Upper Atmospheric Investigations using Radio and Optical Techniques

A THESIS

submitted for the award of Ph.D degree of

MOHANLAL SUKHADIA UNIVERSITY

in the

Faculty of Science

by

Sumanta Sarkhel

Under the Supervision of

Ramanathan Sekar

Professor

Space and Atmospheric Sciences Division

Physical Research Laboratory

Ahmedabad, India

DEPARTMENT OF PHYSICS

MOHANLAL SUKHADIA UNIVERSITY

UDAIPUR

2010

to

the memory of my father

DECLARATION

*I **Mr. Sumanta Sarkhel,** S/o (Late) Mr. Sukumar Sarkhel, resident of A-001, PRL residences, Navrangpura, Ahmedabad 380009, hereby declare that the work incorporated in the present thesis entitled, **"Upper Atmospheric Investigations using Radio and Optical Techniques"** is my own and original. This work (in part or in full) has not been submitted to any University for the award of a Degree or a Diploma.*

Date :

(Sumanta Sarkhel)

CERTIFICATE

I feel great pleasure in certifying that the thesis entitled, **"Upper Atmospheric Investigations using Radio and Optical Techniques"** embodies a record of the results of investigations carried out by Mr. Sumanta Sarkhel under my guidance.

He has completed the following requirements as per Ph.D. regulations of the University

(a) Course work as per the university rules.

(b) Residential requirements of the university.

(c) Presented his work in the departmental committee.

(d) Published minimum of two research papers in a referred research journal.

I am satisfied with the analysis of data, interpretation of results and conclusions drawn.

I recommend the submission of thesis.

Date :

Ramanathan Sekar
Professor
(Thesis Supervisor)

Countersigned by

Head of the Department

Acknowledgements

I express my sincere gratitude to my thesis supervisor Prof. R. Sekar, for his invaluable support and adept guidance that led me towards this thesis. His scientific criticality helped me to overcome the difficulties I encountered in the past few years.

I thank Prof. J. N. Goswami, the Director, Prof. Utpal Sarkar, the Dean, Prof. S. K. Bhattacharya & Prof. A. K. Singhvi, former Deans, Dr. Bhushit Vaishnav, Head, Academic Services and Mr. Y. M. Trivedi, the Registrar, Physical Research Laboratory for providing me the necessary facilities to carry out my thesis work. I am also thankful to the chairman and the members of academic committee for their critical evaluation.

I am thankful to Dipu da for his ineffable selfless moral support and encouragement at every step of my scientific journey at PRL. I also would like to thank Mr. R. Narayanan (Naru Boss) for his invaluable help during my tenure at PRL. I got a lively environment in the lab and as well as during the field campaigns with them. Apart from these, I got a great opportunity to learn about the technicalities of several optical instruments.

I am grateful to Dr. D. Pallamraju for helping me in understanding different aspects of instruments, their applications and scientific discussion.

I thank Prof. R. Sridharan for scientific discussion and his guidance. I enjoyed the company of Dr. Tarun Kumar Pant in field station and discussion in several subjects. I am thankful to Dr. Geetha Ramkumar and (Late) Dr. Sudha Ravindran for their help.

I am grateful to Dr. S. P. Gupta for his support in my scientific career and making the lab lively.

I thank Prof. Shyam Lal for going through my thesis critically.

My sincere regards to Profs. P. B. Rao, B. V. Krishna Murthy, K. N. Iyer, R. Raghavarao, Prashant Panigrahi, J. M. C. Plane, B. R. Clemesha and T. G. Slanger for scientific discussions and their guidance.

I am grateful to the team members of Sensor Development Area, Space Application Centre, Ahmedabad for their support during the calibration of airglow photometer and imager.

I am thankful to Prof. Martin G. Mlynczak, Dr. Tom Marshall, Prof. James M. Russell III, Prof. T. L. Killeen, GATS Inc. team members, and TIMED mission team members for SABER and TIDI data set.

I am thankful to my teachers Prof. Pritam Prasad Ray, Prof. Ranabir Dutt, Prof. Sudipta Narayan Roy, Dr. Sreekantha Sheel and Dr. Arani Chakraborty, Dept. of Physics, Visva Bharati University for their encouragement.

Thanks to Fazlul, R. P. Singh, Amitava, Suneel, Gaurav and Mitesh for creating healthy atmosphere around me which has helped in many ways.

I express my sincere thanks to all the faculty members of Space and Atmospheric Sciences Division: Prof. Harish Chandra, Prof. H. S. S. Sinha, Prof. S.A. Haider, Dr. S. Ramachandran, Dr. Varun Sheel, Dr. Lokesh Sahu, Dr. K. P. Subramanium, Dr. Bhas Bapat, Dr. Som Kumar Sharma, Dr. Y. B. Acharya, Mr. Narain Dutt, Mr. K. S. Modh, Mr. I. A. Prajapati, Mr. S. B. Banerjee, Mr. M. B. Dadhania, Mr. S. Venkataramani and Mr. T. A. Rajesh for their valuable comments and suggestions. I also thank Mr. T. K. Sunil Kumar, Mr. P.K. Pillai and Natu bhai for their help.

I express my gratitude to Dr. P. Sharma and his wife for their caring nature. The care I received from them during my illness cannot be expressed in words.

I am thankful to the Director and all supporting staff members of National Atmospheric Research Laboratory, Gadanki for their support during campaign period. I thank Debashis, Padma, Uma, Sanjay, Venkat, Phani, Radha Krishna, Basha, Mohan, Ashish, Vijay and Vishnu for making atmosphere lively. I am also thankful to Dr. A. K. Patra, Dr. M. Venkat Ratnam, Dr. Y. Bhavani Kumar and Dr. S. Sridharan for their scientific input. I enjoyed the company of Debashis, Mala and other friends during campaign period at Gadanki.

I thank Lakshmi Narayanan and Dhanya Ramani for their help during my stay at Equatorial Geophysical Research Laboratory, Tirunelveli. I am grateful to Prof. S. Gurubaran for scientific discussion.

I express my regards to my batch-mates at PRL: Shuchita, Ayan, Anil, Bhavik, Harindar, Manan, Brajesh, Jitendra, Chandra Mohan (CM), Gyana, Rahaman, Kirpa, Ashwini, Alok, Naveen, Sumita, Ashish, Vishal, Sanjeev, Lokesh, Rohan, Ram Ajor, Timmy. I am thankful to my seniors at PRL: Kushwaha ji, Akhilesh, *Zeen, Rohit bhai, Ritesh bhai, Shreyas bhai, Amit bhai, Sanat da, Uma di, Utpal da, Suranjana di, Subimal da, Kaushik da. Thanks to my juniors: Jayati, Iman, Chinmay, Moumita, Tapas, Arvind Saxena, Arvind Singh, Arvind Rajpurohit, Rohit, Srinivas, Prashant, Vineet, Amzad, Neeraj, Ashok, Vimal, Suratna, Bhaswar, Subrata, Rabiul, Patra, Soumya, Suman, Praveen, Anand, Sandeep, Srikant, Ashish Raj, Naveen Chouhan. The tea-time discussions were one of the entertainments for me.*

I thank Dholokia ji, Subhedar ji, Jigar bhai, Hitendra ji, Alok ji, Tejas bhai and all other staff members of PRL Computer Center for their support.

I am grateful to Nishtha madam for helping me in several ways. I also thanful to Alam, Pragya, Uma ji and all other staff members in PRL Library for their support.

I thank Mr. G. P. Ubale, Vipul bhai and other staff members in PRL Workshop for their help. Thanks to Vaghela ji and Rajesh for their effort in fabricating the optical instruments. I thank Solanki ji, Bikha bhai and Vishnu bhai for their support during the campaign period.

I am thankful to Rajesh ji, Kothari ji, Pitambar ji, Purohit ji and other staff members of Mt. Abu Observatory for their help during Campaign period.

I thank Dr. Samir Dani and Dr. Shital Patel and other staff members of PRL Dispensary for their support during my illness.

I am grateful to Ghanshyam bhai, Sivadashan ji, Parul madam, Ranganathan ji and all other staff members of PRL Administration for their support.

I am grateful for having my loving and caring Grandfathers, Grandmothers, uncles, aunties and cousins.

I express my in-depth love and gratitude towards my Maa and brother, Goutam for their constant support, encouragement and motivation.

Sumanta

List of Publications

1. Identifications of active fossil bubbles based on coordinated VHF radar and airglow measurements, R. Sekar, D. Chakrabarty, **S. Sarkhel**, A. K. Patra, C. V. Devasia and M. C. Kelley, *Ann. Geophys.*, 25, 2099-2102, 2007.

2. Simultaneous sodium airglow and lidar measurements over India: a case study, **S. Sarkhel**, R. Sekar, D. Chakrabarty, R. Narayanan, and S. Sridharan, *J. Geophys. Res.*, 114, A10317, doi:10.1029/2009JA014379, 2009.

3. A Case Study on the Possible Altitude-Dependent Effects of Collisions on Sodium Airglow Emission, **S. Sarkhel**, R. Sekar, D. Chakrabarty, and S. Sridharan, *J. Geophys. Res., 115,* A10306, doi: 10.1029/2010JA015251, 2010.

4. A Review on the Na Airglow Mechanism using Simultaneous Na Airglow and Na Lidar Measurements over India, R. Sekar, **S. Sarkhel**, and D. Chakrabarty, *Asian J. Phys.,* in press, 2010.

5. Mesospheric Gravity Waves over Indian Low Latitude Stations using Sodium Airglow Measurements, **S. Sarkhel**, R. Sekar, D. Chakrabarty, and R. Narayanan, *To be communicated*, 2010.

Papers Presented in National/International Conferences

1. Attended **International School on Atmospheric Radar (ISAR-NCU 2006), Chung-Li, Taiwan** and delivered a talk entitled "Mesosphere-lower ionosphere investigations using Indian MST radar and optical techniques."

2. Presented a paper entitled "Simultaneous sodium airglow and sodium lidar observations from Gadanki" by **S. Sarkhel**, R. Sekar, D. Chakrabarty, R. Narayanan and Y. Bhavani Kumar in **15th National Space Science Symposium (NSSS 2008), Ooty, India.**

3. Presented a paper entitled "On the role of collisions in the sodium airglow process" by **S. Sarkhel**, R. Sekar, D. Chakrabarty, R. Narayanan, and S. Sridharan in **16th National Space Science Symposium (NSSS 2010), Rajkot, India.**

4. Presented a paper entitled "Sodium Airglow Observations from India" by **S. Sarkhel**, R. Sekar, D. Chakrabarty, R. Narayanan, and S. Sridharan in **AOGS 2010, Hyderabad, India.**

5. Presented a paper entitled "Mesospheric Gravity Waves over Indian Regions using Sodium Airglow Measurements" by **S. Sarkhel**, R. Sekar, D. Chakrabarty, and R. Narayanan in **COSPAR 2010, Bremen, Germany.**

Abstract

The present thesis work comprises of the investigations of upper atmosphere using narrow-band airglow photometers, sodium (Na) lidar, radars and satellite-borne instruments. Coordinated observations using Na airglow photometers and Na lidar were obtained from Gadanki (13.5°N, 79.2°E) during March, 2007 which were supplemented by altitude profiles of ozone concentration and temperature obtained from SABER instrument on board TIMED satellite. A case study shows that the measured average airglow intensity on one night (20 March, 2007) is less as compared to the next night despite Na atom concentration being large. Detailed analyses reveal that collisional quenching process was responsible for the reduced airglow intensity on 20 March as, atmospheric pressure at mesospheric height on that night was found to be larger compared to the next night. Further, on a given night, it was observed that Na airglow intensity variation matches fairly well with the Na atom concentration at an altitude situated at around one scale height above the altitude of maximum Na atom concentration. The analyses suggest that the altitude variation of the collisional quenching needs to be considered to account for the observed Na airglow intensity variation.

Systematic measurements using Na airglow photometers were carried out from Mt. Abu (24.6° N, 72.7° E) and Gadanki during cloudless and moonless nights of winter and equinoctial months during 2006-2009 in order to derive the periodicities of gravity waves. The analyses using mesospheric temperature and horizontal wind, obtained from TIMED and TIDI onboard TIMED satellite, nearly over both the places reveal the occurrence of convective and dynamical instabilities within Na airglow layer on a few occasions. The power spectra of Na airglow intensity variations indicate that the dominant periods, on those observational nights are significantly less in comparison with the cases where the instabilities occurred much beyond the Na airglow layer suggesting the possibility of breaking of gravity waves into smaller-scale sizes in the former cases.

Some of these of gravity wave modes penetrate through the mesopause layer and reach thermosphere-ionosphere system. These gravity waves may act as a seed perturbation to generate plasma bubbles during post sunset hours which evolve in space and time. During post mid-night hours, these plasma bubbles become non-evolutionary and drift with the background wind and are known as fossil bubbles. However, on a few occasions, these may be observed to be reactivated by the neutral winds and can be captured by coordinated VHF radar and 630.0 nm airglow photometric measurements. One such case in support of this proposition is reported in the present thesis.

Keywords

Sodium Atom, Sodium Airglow, Mesosphere, Collisional Quenching, Mesopause, Gravity Waves, Convective and Dynamical Instabilities, Equatorial Spread F, Active Fossil Bubble

Contents

Chapter 1

Introduction to Earth's Upper Atmosphere

1.1 Earth's Atmosphere

The Earth's atmosphere is the gaseous envelope surrounding the globe, which protects life on Earth by absorbing high energy radiation from space. Based on the composition and distribution of different gases in the Earth's atmosphere, it can be divided into two regions as homosphere and heterosphere. Homosphere is the part of the atmosphere that is dominated by turbulence and as a consequence, all the species are homogeneously mixed up. The major gaseous components within homosphere is molecular nitrogen (N_2) (78% by volume) and molecular oxygen (O_2) (21% by volume). The overall scale height of the homosphere is mainly governed by N_2 and the mean molecular mass more or less remains constant. Homosphere extends up to turbopause ($\sim$100 km) beyond which turbulence ceases and molecular diffusion takes over. This region of atmosphere is known as heterosphere where the vertical distribution of different species depends on their own masses and hence the scale height of individual species is different.

The density and pressure of the atmosphere decrease exponentially with the altitude. However, the variation of temperature is dissimilar at different altitude regions of atmosphere depending upon the thermal processes.

1.2 Thermal Structure of the Atmosphere

Based on the temperature variation of neutral species with altitude, the Earth's atmosphere is classified into several layers.

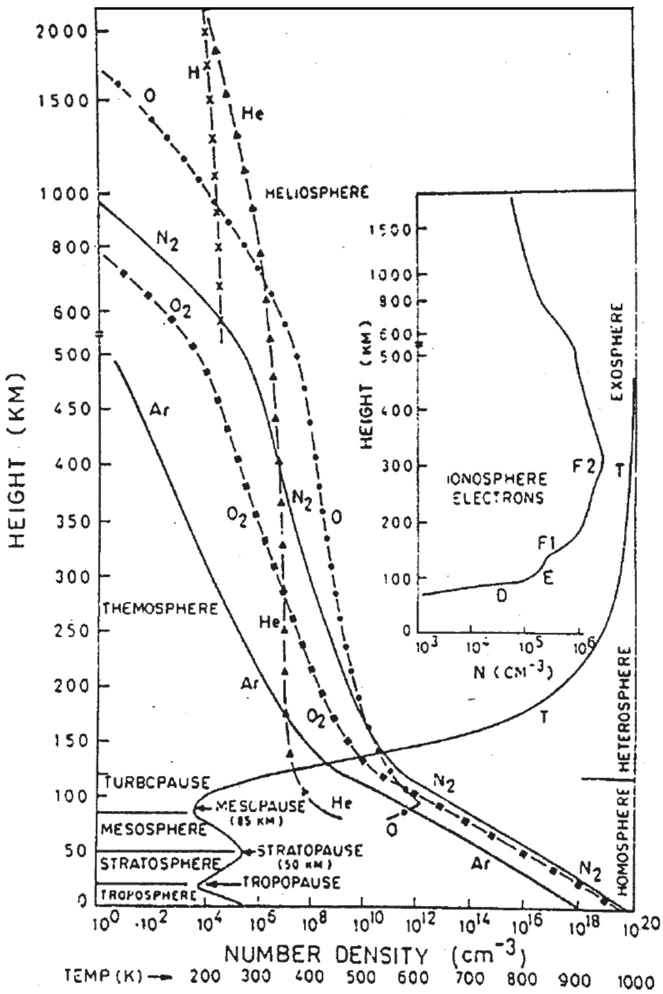

Figure 1.1: The altitude variation of temperature and concentration of neutral species in Earth's atmosphere. The inset figure shows the altitude distribution of ionized species (Compiled from different sources, courtesy: *Pallamraju,* 1996).

The lowest layer is called **Troposphere**, which is denser than any other layer of the atmosphere. This region of the atmosphere mostly controls weather and it ends at tropopause at a height of ~8 km at pole and ~16 km at equator. The troposphere contains more than 75% of the total atmospheric gases. The temperature decreases at the rate of ~6.5 K/km and the temperature at tropopause is ~220 K at pole and ~190 K at equator.

The temperature, beyond tropopause, increases with altitude up to stratopause ($\sim$55 km) where temperature may reach $\sim$270 K. This region of atmosphere is known as **Stratosphere**. The presence of ozone molecules is the primary cause for this increase in temperature as it absorbs solar ultraviolet radiation and plays a vital role in preventing the harmful solar ultraviolet radiation from reaching the surface of the Earth.

In the region beyond stratopause, temperature again decreases and this layer is known as **Mesosphere**. The temperature in mesosphere is less due to lack of heating mechanism and radiative cooling mainly by hydroxyl molecules. Mesopause ($\sim$85-95 km) is the coldest region in the Earth's atmosphere where temperature can be as low as $\sim$160 K. It is the layer where most meteors ablate upon entering the atmosphere.

Beyond mesopause, temperature again increases with altitude and may reach 800-1500 K depending on day, night, season and solar epoch. This part of upper atmosphere is known as **Thermosphere** which extends up to $\sim$600 km. The increase in temperature occurs due to absorption of solar extreme ultraviolet radiation by ambient molecules. Ionization of molecules by energetic solar radiation produces a layer of plasma consisting of free electrons and ions. These plasma layers interact differently with the Earths magnetic fields. This region of the atmosphere is strongly influenced by the variations in solar activity.

Exosphere is the region beyond thermosphere where temperature remains nearly constant with altitude. As the ambient density is significantly low, the mean free path of each molecule drastically increases. The exosphere is mainly composed of Hydrogen (H) and Helium (He).

1.3 Mesosphere and Lower Thermosphere

Mesosphere and Lower Thermosphere (MLT) is one of the least explored regions in the Earth's atmosphere. This region is substantially altered by the dynamical phenomena like atmospheric gravity waves, tides, planetary waves, etc [e.g. *Krishna Murthy et al.,* 1992; *Rajaram and Gurubaran,* 1998; *Gurubaran and Rajaram,* 1999; *Sridharan et al.,* 2002; *Vineeth et al.,* 2005; *Pant et al.,* 2007; *Kumar et al.,* 2008].

The atmospheric gravity waves [*Hines,* 1960] are mostly generated in the lower atmosphere and propagate to the upper atmosphere. The propagation and dissipation of these waves modulate the neutral density and temperature in the MLT region. These atmospheric gravity waves are generated by processes like thermal forcing, lightning, wind flow over a mountain etc. and Earth's gravity acts as a restoring force in the propagation of these waves. In course of its upward propagation, these waves carry energy and momentum. In order to conserve energy, its amplitude grows exponentially with the altitude and reaches a stage where it cannot grow further and breaks into smaller scales. In the process of breaking they deposit energy and momentum to the ambient medium. It is recognized that these waves make significant contributions to the thermal and momentum budgets of the upper mesospheric region [*Lindzen,* 1981]. Considerable amount of total heat budget of mesosphere is contributed by gravity waves [*Killeen and Johnson,* 1995]. Thus, the dynamical condition of MLT region is strongly controlled and modified by these waves. Mesopause, being the interface between mesosphere and thermosphere, acts as a filter for various gravity wave modes. Mesopause can be found at the altitude of around 100 km [e.g. *Venkat Ratnam et al.,* 2010] over low latitudes. This has important consequences in deciding the gravity wave modes reaching thermosphere that play a significant role in the coupling between middle and upper atmosphere [*Guharay,* 2009].

Systematic investigation on gravity waves can be carried out using tracers such as metallic atoms concentration, airglow emission intensities, etc in the MLT region. The passage of gravity waves modulates the metallic atoms and airglow layer and hence the quasi-periodic fluctuation in the physical parameters associated with the medium caused by the waves can be investigated to derive the gravity wave modes. Thus, systematic measurements of metallic atoms and airglow emissions in MLT region is necessary to characterize gravity waves that have significant impacts on the dynamics and energetics of MLT region.

1.3.1 Metal Layers in the MLT Region

The occurrences of thin layers of metals have been observed in the altitude region of 80 to 105 km and meteoric ablation is known to contribute to the generation of these metallic layers. The major metallic constituents [*Mason,* 1971] of meteorites are:Magnesium (Mg) 12.5 %, Iron (Fe) 11.5%, Aluminum (Al) 1.7%, Nickel (Ni) 1.5 %, Calcium (Ca) 1.0% and Sodium (Na) 0.6 %. Several metal atoms such as Sodium (Na), Potassium (K), Iron (Fe) and Calcium (Ca) have been observed by the ground based remote sensing technique like LIDAR (LIght Detection And Ranging). Typical altitude profiles of these metallic atoms are given in Figure 1.2. These metals exist as free atoms within the altitude region of 80 to 100 km. The ozone (O_3) molecules oxidize metal atoms to metal oxides and form a variety of compounds such as hydroxides, carbonates, and bicarbonates. The atomic oxygen (O) and associated with atomic hydrogen (H) reduce these compounds back to metal atoms [*Plane,* 2003a].

Above 100 km, the metals become ionized by charge transfer with the increasing levels of E region ions such as NO^+ and O_2^+. Metallic ions are also formed directly in the lower thermosphere via hyperthermal collisions during meteoroid ablation below 100 km. The presence of metallic ions in the form of layers have been reported in the altitude region of 85 to 130 km using mass spectrometric measurements over different latitudes [e.g. *Narcisi and Bailey,* 1965; *Goldberg et al.,* 1974; *Sridharan,* 1983]. Figure 1.3 shows a typical nighttime profiles of metallic ion layers in MLT region over Thumba, India measured using mass spectrometer onboard a sounding rockets.

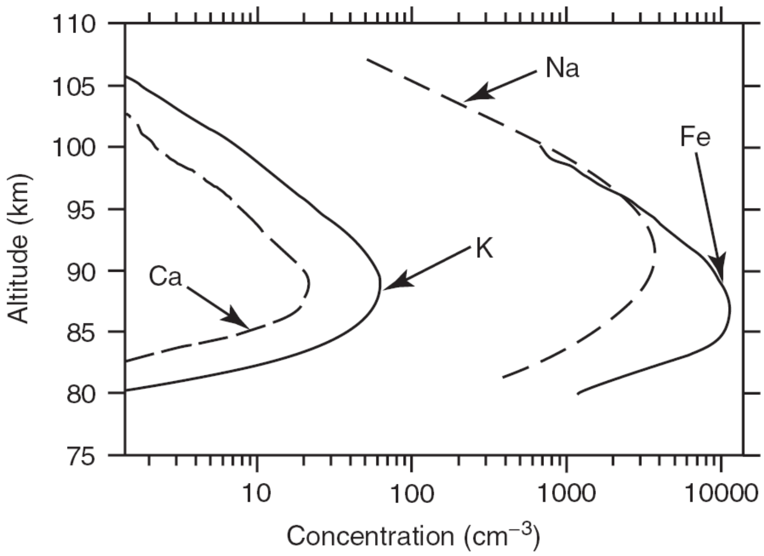

Figure 1.2: Vertical profiles of the annual mean concentrations of Fe, Na, K, and Ca measured by lidar at a number of mid-latitude locations (After *Plane* [2003a]).

Neutralization of these metallic ions can occur through radiative recombination with electrons. In addition, the ions can recombine with molecules like H_2O, CO_2, N_2, O_2, etc to form complex ions and can undergo dissociative recombination with electron to form neutral atoms.

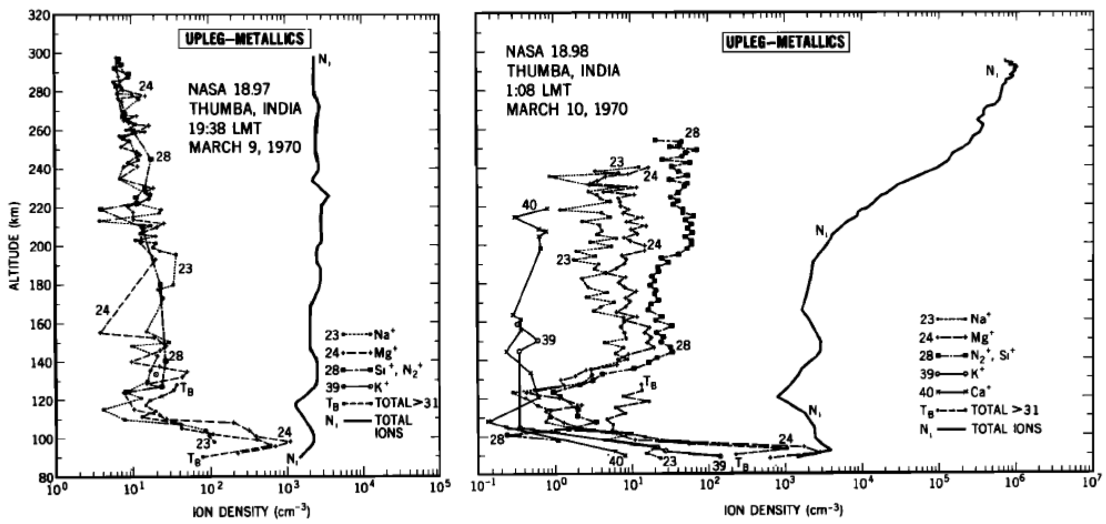

Figure 1.3: Observed distribution of positive metallic ions over Thumba (After *Goldberg et al.,* [1974]).

The relative abundances of the metal atoms in MLT region are quite different from their relative abundances in meteorites. For example, the atomic calcium is depleted more in comparison with atomic sodium [*Williams,* 2002]. These metals also exhibit different seasonal behavior. The integrated column densities of all the metals peak in early winter. Sodium and iron have a mid-summer minimum, whereas calcium and potassium have a secondary mid-summer maximum and hence little seasonal variation [*Plane,* 2003b]. These differences in the relative concentrations in the atmosphere to their parent sources (meteors) are due to the combination of differential ablation (for example, the least volatile metal, calcium, is ablated around 10 km lower in the atmosphere than sodium) and differences in the gas-phase chemistries controlling the layers [*Plane,* 2003b].

1.3.2 Sources of Metals in the MLT region

The sources of mesospheric metals in MLT region were initially believed to be due to the release during the day by thermal evaporation and photo-sputtering of chloride. The postulated origin of metals includes sea-salt aerosols, volcanic debris, and particles formed from the condensation of refractory species produced during meteoric ablation. However, in recent times, strong evidences of direct ablation of incoming meteoroids have been obtained and believed to be the major source of the mesospheric metals. As discussed in *Plane* [2003a], these evidences include sporadic enhancements in the total column abundance of sodium during meteor showers, and the direct observation of metal deposition in short-lived meteor trails using high-resolution lidar [*Kane and Gardner,* 1993; *von Zahn et al.,* 1999; *Pfrommer et al.,* 2009].

The ablation of interplanetary dust particles deposits several tonnes of a variety of metals into the Earth's upper atmosphere. The daily input of meteoric material into the atmosphere had been estimated to be around 44 tonnes using observations by meteor radar. As discussed in *Plane* [2003a], most of the incoming meteoric mass is in the form of interplanetary dust particles in the mass range of 1–1000 μg (median mass 10 μg), with a radius range of 50–500 μm (median radius 100 μm). It should be noted that particles which originate within the solar system must have entry velocities that range from 11.5 km/s to 72 km/s. The lower limit is the escape velocity for a particle leaving Earth and is the lowest velocity that a particle falling towards the Earth can have. The uppermost limit is the sum of two components, a 30 km/s associated with the velocity of Earth itself around the sun and a 42 km/s associated with the maximum velocity of a meteor (the escape velocity of a particle leaving solar system is 42 km/s) [*Sridharan,* 1983]. Due to their very high entry velocities, meteoroids undergo rapid frictional heating by collision with air molecules, and their constituent minerals subsequently vaporize. The frictional heating produces temperature around 2000 K that causes about half of the meteoric material entering the atmosphere to ablate in the altitude region of 80 to 100 km, providing a direct source of metal atoms and ions [*Plane,* 2003a].

1.3.3 Measurements of Meteoric Metals

Systematic measurements of metallic layer are carried out using lidar technique with excellent altitude and temporal resolutions. The first quantitative measurements of metal atoms were made using ground-based photometers. The photometers measure the intensity of the resonance lines from the spectroscopic transitions of metal atoms such as Na, K, Fe and Ca^+ ions excited by solar radiation [e.g. *Blamont et al.,* 1958; *Hunten,* 1967]. A large scattering cross-section is needed in order to detect their existence as their concentrations are extremely less as compared to the ambient atmospheric neutral concentration. Photometers were generally pointed towards zenith during twilight, when the geometrical shadow height of the Earth (the terminator) was close to mesospheric altitudes. Using radiative transfer theory, the vertical concentration profiles were derived from the variation of the emission signal as the terminator passes through the metal layer.

During early 1970s, the photometry technique was superseded as the discovery of tuneable laser sources allowed the development of the resonance lidar (laser radar) technique that enabled the metallic layers to be observed with better accuracy and excellent altitude and temporal resolution [*Sandford and Gibson,* 1970]. In this technique, a pulsed laser beam is tuned to a strongly allowed spectroscopic transition of the metallic atom of interest and transmitted into atmosphere. The laser pulses transmitted to atmosphere undergo Mie and Rayleigh scattering processes respectively due to atmospheric aerosols and molecules particularly in the lower atmosphere. In the mesosphere, the pulse is resonantly scattered by the metal atoms and a small fraction of the scattered signal is detected by a ground-based receiver. The absolute metal concentration at each altitude level in the mesosphere can be derived based on the returned laser signal with the knowledge of resonant scattering cross-section of that metal, Rayleigh-scattering cross-section at an altitude where Rayleigh scattering dominates over any other scattering processes.

The lidar studies substantially contributed in understanding of mesospheric metal chemistry. In order to understand the geophysical significance of these layers, several model based calculations were carried out [e.g. *Plane,* 2004] with the knowledge of the fundamental physio-chemical parameters like rate coefficients and photolysis cross-sections. These mesospheric metal chemistry was simulated in the laboratory under suitable mesospheric condition in order to understand the different phases of the reaction of mesospheric metals with the atmospheric constituents such as O_3, O_2, O, H, H_2, H_2O and CO_2 in mesosphere [e.g. *Plane,* 2002].

1.3.4 Observations of Sodium in the MLT Region

The atmospheric sodium was discovered with the measurements of nighttime spectral emissions at wavelength corresponding to sodium D_2 emission resonance line [*Slipher,* 1929]. During late 1930s, it was determined that this emission was related to the atmospheric neutral sodium atoms and speculation had begun to find out the source and altitude distribution of sodium [*Bernard,* 1938a; *Cabannes et al.,* 1938]. *Bernard,* [1938b] identified the neutral atoms are responsible for 589.0 nm emission. *Dejardin* [1938] discussed the origin of sodium atoms in upper mesosphere. *Cabannes et al.* [1938] supported the origin to be extraterrestrial.

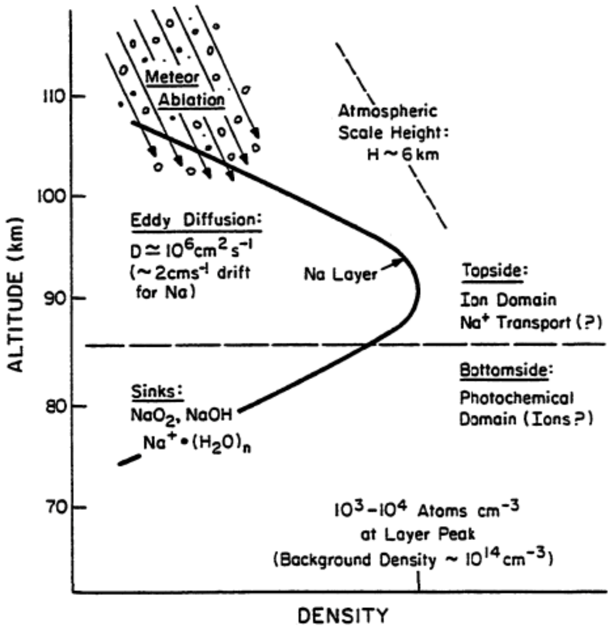

Figure 1.4: The principal processes involved in the formation of the mesospheric sodium layer (After *Voelz,* [1987]).

Sodium atoms can be found within the altitude region of 80 to 105 km as free atoms. Meteors ablate sodium into mesosphere and the ablate products get oxidized by O_3 to form variety of compounds such as hydroxides, carbonates, and bicarbonates (Figure 1.4). These reactions are, in general, favored below 100 km. The investigation on the production of these complex molecules have been carried out and simulated in laboratory under mesospheric conditions [*Plane et al.,* 1999b; *Plane,* 2004]. These oxides compounds are further reduced by O and H to produce back the metal atoms. This gas phase chemistry of sodium atom has been extensively investigated [*Plane* [2003a] and references therein].

Above 100 km altitude, the sodium atoms are ionized by charge transfer with NO^+ and O_2^+ ions to form Na^+. These Na^+ ions can recombine with electrons below 100 km to form neutral sodium atoms as, the lifetime of Na^+ is less [*Daire,* 2002]. The Na^+ ions are also believed to be responsible for the sudden or sporadic sodium layers [e.g. *Clemesha et al.,* 1996; *Vishnu Prasanth et al.,* 2007].

The first lidar measurements of the sodium layer were presented by *Bowman et al.* [1969]. The sodium density and column abundance have been measured by several researchers using broadband resonance fluorescence lidars where the spectral width of the laser pulse was much larger compared to the absorption resonance line width. Figure 1.5 represents a typical altitude profile of neutral sodium atom measured using sodium resonance lidar over Gadanki, India.

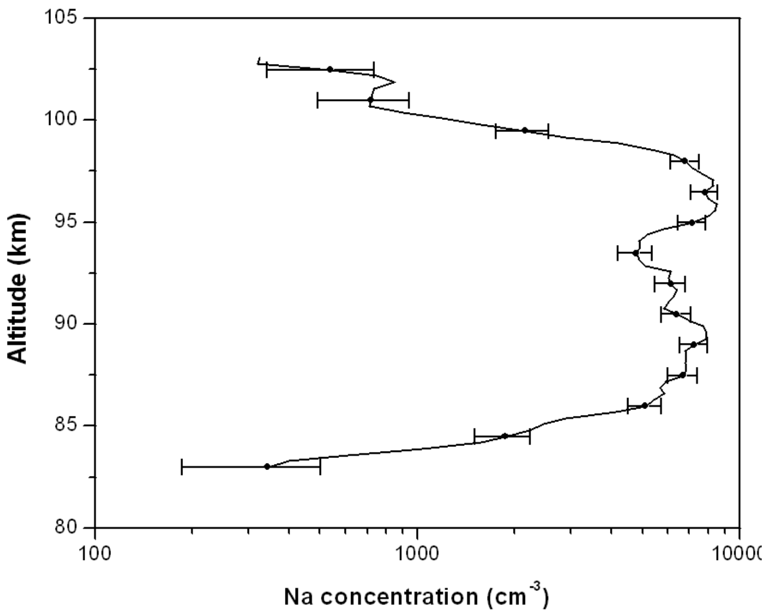

Figure 1.5: A typical nighttime profile of neutral sodium atom measured over Gadanki, India (After *Bhavani Kumar et al.* 2007a).

Long-term observations of the sodium layer provided more details of seasonal, latitudinal and diurnal variations [*Sandford and Gibson,* 1970; *Gibson and Sandford,* 1971,1972; *Blamont et al.,* 1972; *Kirchhoff and Clemesha,* 1973; *Rowlett et al.,* 1978; *Clemesha et al.,* 1979; *Kirchhoff and Clemesha,* 1983a; *Gardner et al.,* 1988; *Plane et al.,* 1999a; *She et al.,* 2000; *Clemesha et al.,* 2004]. In addition, several measurements of mesospheric sodium were carried out over Indian low latitude stations, Gadanki [*Bhavani Kumar et al.* 2007b, *Vishnu Prasanth,* 2007; *Sarkhel et al.,* 2009, 2010]. The lidar measurements can provide the altitude distribution of neutral sodium atoms in mesosphere with good temporal and altitude resolution. These meteoric origin of sodium atoms produce sodium airglow and are widely used as tracer to understand the dynamics in the MLT region.

1.3.5 Sodium Airglow

As discussed earlier, *Slipher* [1929] discovered the spectral resonance line of sodium atom. Measurements of sodium twilight glow (resonantly scattered sunlight at twilight) began in the 1950s [*Chamberlain et al.,* 1958; *Bullock and Hunten,* 1961; *Sullivan,* 1971]. The first atmospheric sodium chemistry theory was proposed by *Chapman* [1939] in an effort to explain the nighttime airglow emissions. The Chapman mechanism describes the conversion of neutral sodium to excited sodium atoms. The proposed mechanism suggested that mesospheric ozone plays an important role for this emission.

$$Na + O_3 \xrightarrow{k_1} NaO + O_2 \tag{1.1}$$

$$NaO + O \xrightarrow{\alpha k_2} Na^*(^2P) + O_2 \tag{1.2}$$

$$\xrightarrow{(1-\alpha)k_2} Na(^2S) + O_2$$

$$Na^*(^2P) \longrightarrow Na(^2S) + h\nu(589.0, 589.6\ \ nm) \tag{1.3}$$

In the above scheme, k_1, k_2 are the temperature dependent reaction rate constants for reactions given in equations 1.1 and 1.2 respectively and α is the branching ratio for the reaction in equation 1.2.

Chapman mechanism explains the origin of sodium airglow emission from sodium atoms. The neutral sodium atoms are first oxidized by O_3 to produce NaO. It further reacts with mesospheric atomic oxygen (O) to produce the mixer of excited and ground state of Na atoms. The abundance of these excited atoms can be determined by the branching ratio of this reaction. Chapman mechanism provided first systematic explanation for generation of sodium airglow emission. This mechanism suggests one-to-one relation between sodium atoms and sodium airglow intensity provided O_3 concentration remains same.

Substantial measurements of sodium airglow have been carried out from low latitude station using ground-based photometers [e.g. *Clemesha et al.,* 1979; *Kirchhoff et al.,* 1981]. These ground based photometers measures the altitude-integrated airglow (expressed in terms of Rayleigh; 1 Rayleigh = 10^6 photons. $cm^{-2}.s^{-1}.sr^{-1}$) with excellent temporal resolution.

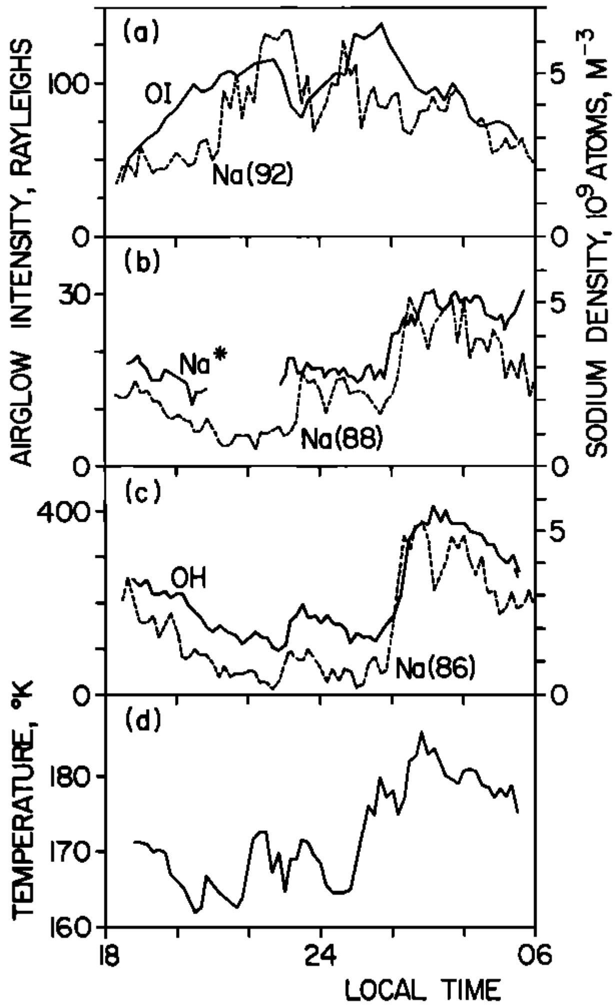

Figure 1.6: Typical nocturnal variations of airglow and sodium density. (a) OI 557.7 nm and sodium density at 92 km, (b) NaD and sodium density at 88 km, (c) OH (8,3) and sodium density at 86 km, and (d) variation of the OH (8,3) band rotational temperature (After *Clemesha et al.* 1979).

The solid curve in Figure 1.6b represents a typical nocturnal sodium airglow intensity variation over low latitude. Gravity wave induced perturbation can be observed in the intensity variation. These photometric observations of sodium airglow are useful in deriving the period of atmospheric gravity waves.

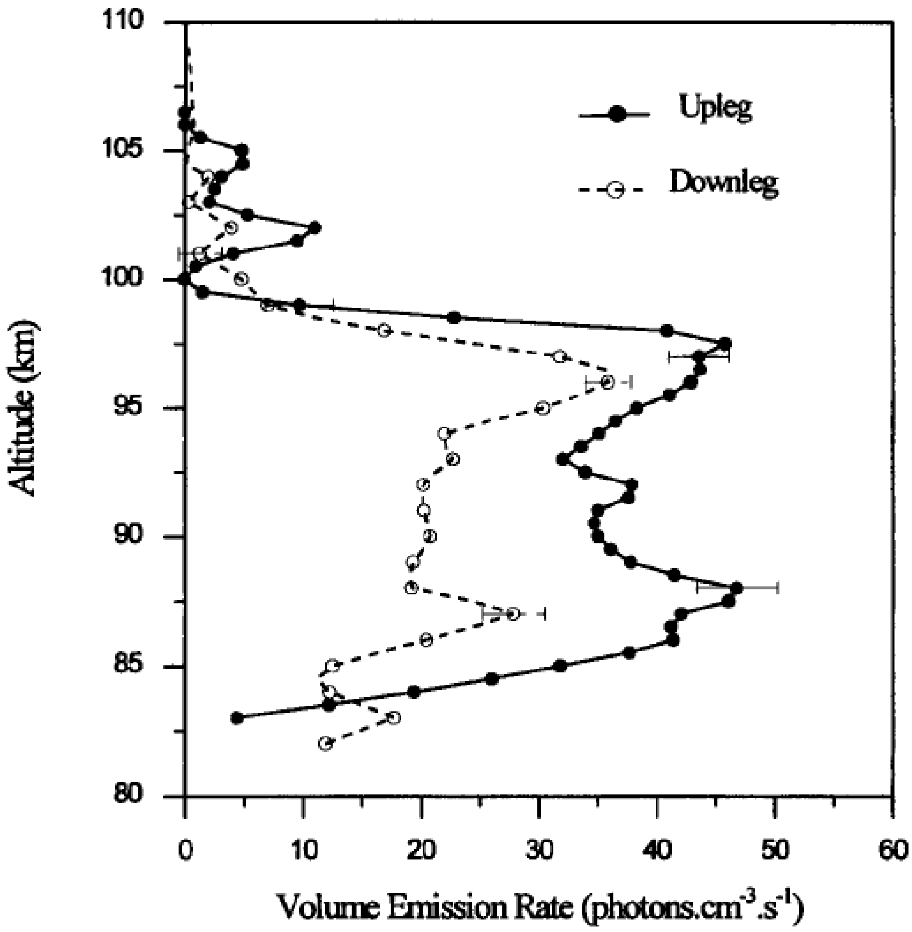

Figure 1.7: Typical nighttime profiles of sodium airglow (After *Takahashi et al.* 1996a).

Using rocket borne photometers, several in-situ measurements of sodium airglow have also been carried out [e.g. *Clemesha et al.,* 1993; *Takahashi et al.* 1996a; *Hecht et al.,* 2000]. Figure 1.7 shows a typical nighttime altitude profile of sodium airglow over low latitude measured using sodium airglow photometer onboard a sounding rocket. It is to be noted that the sodium airglow layer is situated within 85-97 km. The altitude profiles of sodium airglow have importance in deriving the vertical parameters of gravity waves.

Several simultaneous measurements of sodium atoms and sodium airglow intensity have been carried out to evaluate the relationship between them [e.g. *Clemesha et al.,* 1978, 1979; *Clemesha et al.,* 1993; *Takahashi et al.,* 1996a, 1996b].

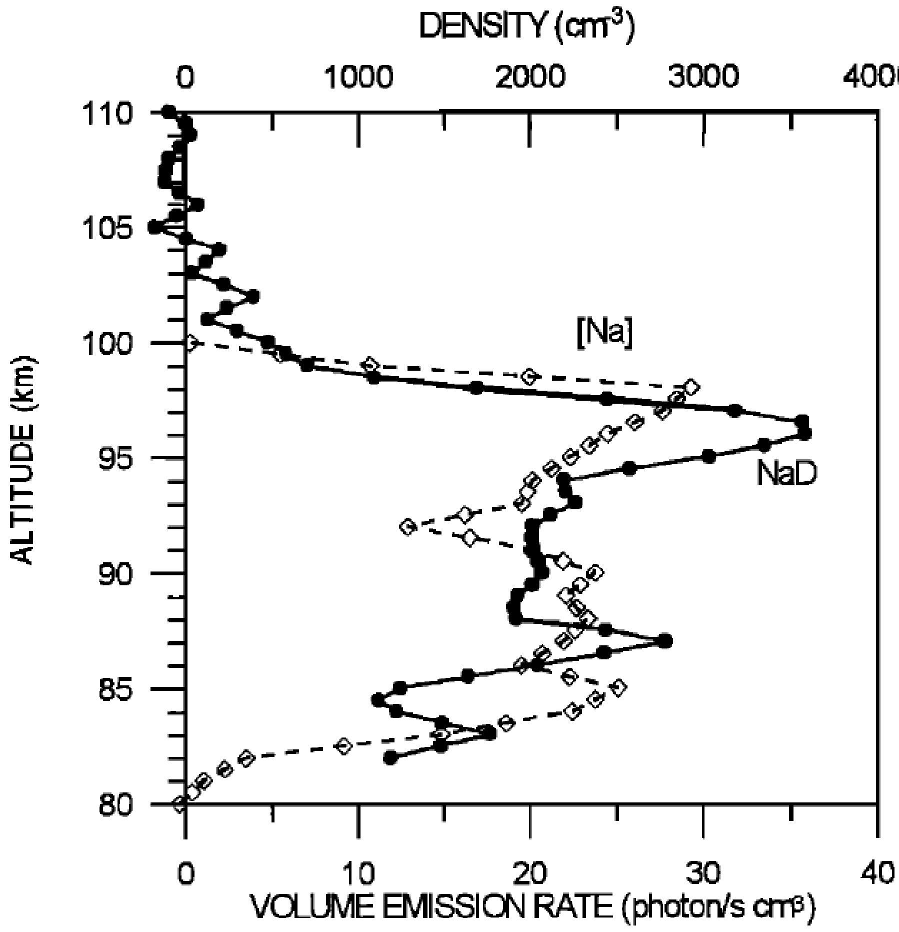

Figure 1.8: A typical nighttime profile of sodium airglow (NaD) and sodium atom concentration [Na] (After *Takahashi et al.* 1996b).

Figure 1.8 represents a typical sodium airglow profile measured using a onboard photometer overlaid on an altitude variation of neutral sodium atom concentration measured using a collocated sodium lidar. The branching ratio (α) pertaining to the reaction given in equation 1.2 is crucial in this aspect as it effectively determines the fraction of the sodium atoms that ends up emitting sodium airglow. More the value of α, greater is the amount of excited sodium atoms and hence sodium airglow intensity. Therefore, several attempts were made to estimate the value of α based on theoretical and experimental techniques.

By considering the symmetry properties of the correlated electronic states, *Bates and Ojha* [1980] estimated a value of 1/3 for α. Subsequent investigations were carried out based on laboratory measurements under mesospheric conditions that reported α to be as low as 0.01 [*Plane and Husain,* 1986]. On the contrary,

α was estimated to be 0.67 based on theoretical calculations [*Herschbach et al.,* 1992]. Based on rocket-borne photometry and lidar measurements, *Clemesha et al.* [1995] calculated the range of α to lie between 0.05 to 0.2 with the best fit value to be $\sim$0.1. Using the measurements by on-board photometers and ground-based Na lidar as well as airglow imager, *Hecht et al.* [2000] found that the value of α lies between 0.02 and 0.04 whereas recent laboratory based experiments [*Griffin et al.,* 2001] provided an estimation of α to be 0.14 ± 0.04.

The investigations reported above reveal that α has enormous variability and this aspect cannot be explained by the Chapman mechanism. In addition, a few recent observations indicate that the Chapman mechanism cannot explain sodium airglow variations comprehensively. Recently, *Slanger et al.* [2005] and *Plane et al.* [2007] carried out spectroscopic measurements of Na D_2 (589.0 nm) and Na D_1 (589.6 nm) lines and the intensity ratio (R_D) of Na D_2 and Na D_1 line was observed to be variable.

Figure 1.9 shows the temporal variation of R_D with an average value of around 1.8 with the minimum and maximum value of 1.3 and 2.4 respectively. It can clearly noted that R_D is variant with time. In addition, a seasonal variation of R_D was determined based on observations (shown in Figure 1.10). The value of R_D maximizes during March-April and September-October. The minimum value of R_D can be observed during July-August.

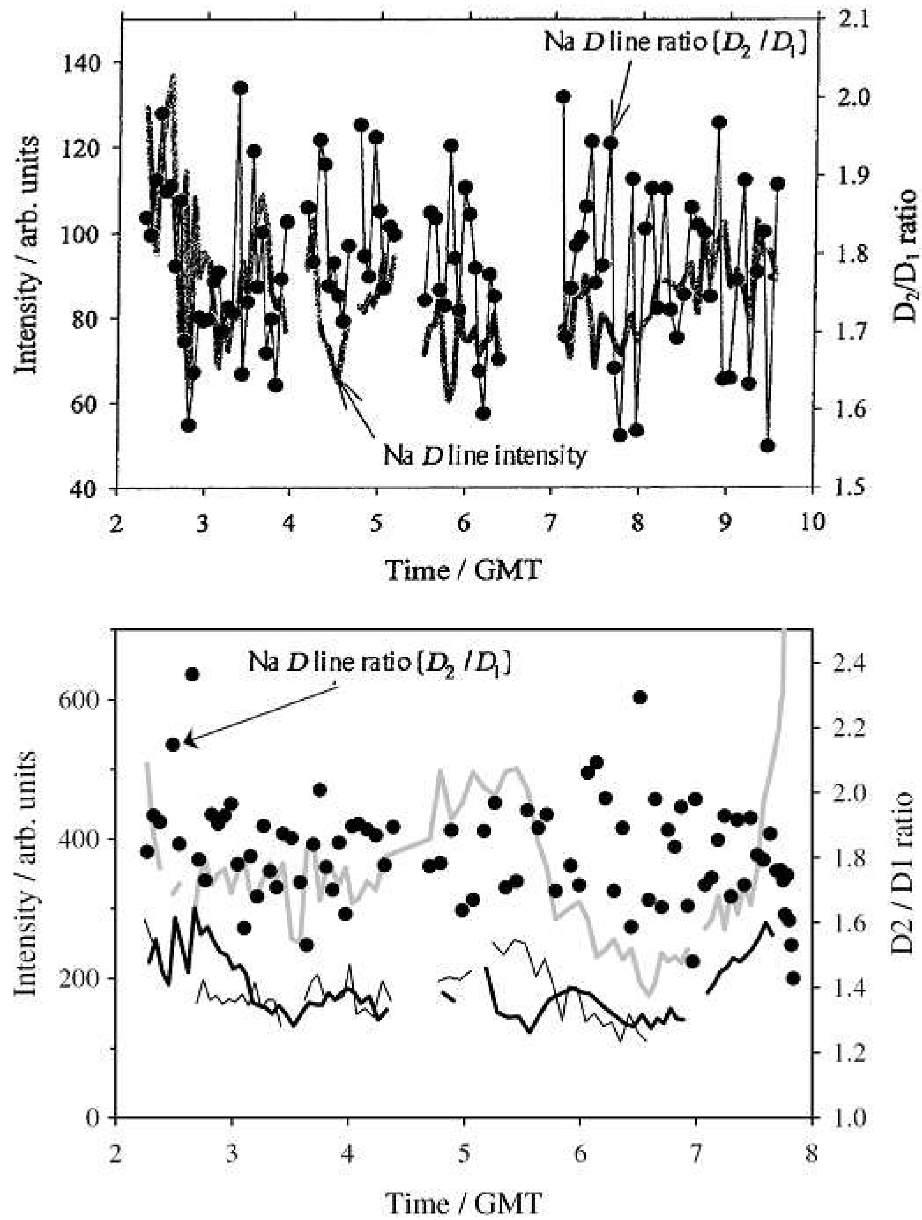

Figure 1.9: (a) Temporal variations of sodium airglow (NaD) and sodium D_2/D_1 intensity ratio (R_D) (After *Slanger et al.* 2005). (b) Temporal variations of NaD (gray thick line), OI (black thick line) and OH* (black thin line) emission intensities, and the R_D measured from the NASA DC-8 between 40°N and 50°N during 17th November 2002 (After *Plane et al.,* 2007).

The Na D_2 and Na D_1 emissions respectively arise due to the electronic transitions between the Na($^2P_{3/2}$) and Na($^2P_{1/2}$) states to ground state Na(^{2}S). The intensity ratio R_D must be 2.0 if Na($^2P_{3/2}$) and Na($^2P_{1/2}$) are produced according to their spin orbit statistical weights. It is to be noted that the frequency of collisions with the ambient molecules, at the pressure below 10^{-5} bar in the upper atmosphere, is too low to equilibrate the Na(^{2}P) spin orbit states before emission occurs as, the lifetime of Na(^{2}P) state is only 16 ns [*Slanger et al.,* 2005]. Based on several investigations during 1935–1960, *Chamberlain* [1995] estimated R_D to be 2. The latter measurements also showed the value of R_D to be ~2 [*Sipler and Biondi,* 1978].

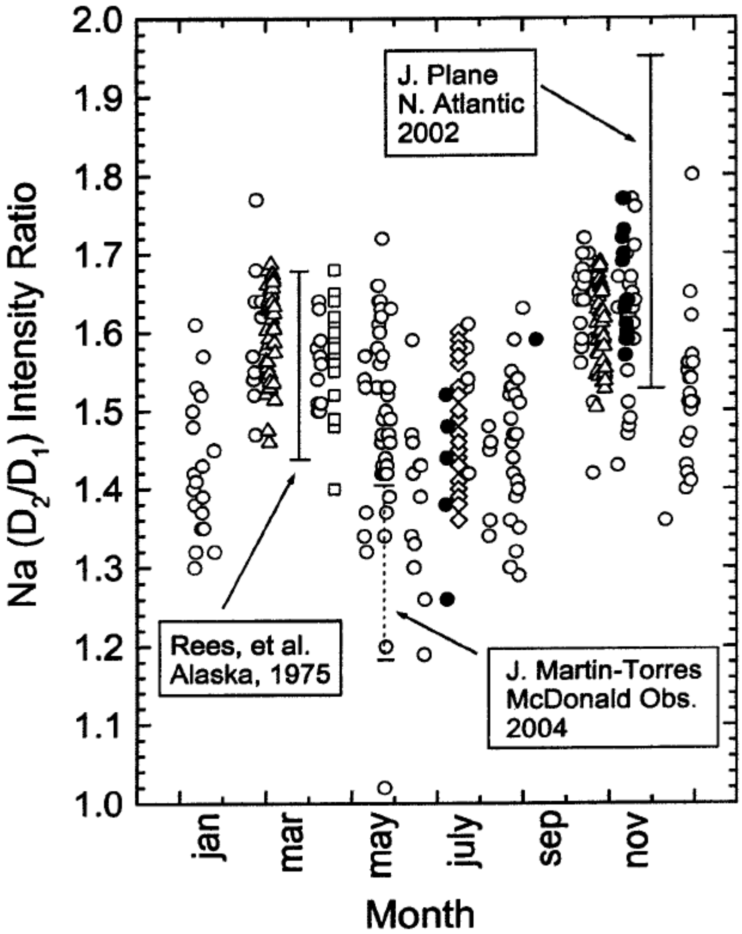

Figure 1.10: Seasonal dependence of sodium D_2/D_1 intensity ratios. Open circles, HIRES, 19931997; solid circles, HIRES, 1999; open triangles, ESI, 2000; open squares, ESI, 2001; open diamonds, ESI, 2001/2002 (After *Slanger et al.* 2005).

As R_D is a spectroscopic parameter, it is not expected to change under any atmospheric condition. However, the measurements by *Slanger et al.* [2005] and *Plane et al.* [2007] indicate that R_D is quite variable. In order to accommodate these aspects, the original Chapman mechanism is modified by *Slanger et al.* [2005] recently.

$$Na + O_3 \longrightarrow NaO^*(A^2\Sigma^+) + O_2 \tag{1.4}$$

$$NaO^*(A^2\Sigma^+) + O(^3P) \longrightarrow Na^*(^2P_J) + O_2 \tag{1.5}$$

$$NaO^*(A^2\Sigma^+) + M \longrightarrow NaO(X^2\Pi) + M \tag{1.6}$$

$$NaO(X^2\Pi) + O(^3P) \longrightarrow Na^*(^2P_J) + O_2 \tag{1.7}$$

In this chemical scheme, an intermediate channel is introduced to explain various observations. It was shown that the oxidation of Na with O_3 mostly produces NaO in excited state (NaO*). The values of both branching ratio (α) and R_D are higher when NaO* directly reacts with O. However, the values will be less, if NaO* is quenched by ambient molecules at mesospheric altitudes, to produce NaO before it reacts with O. Therefore, the ambient atmospheric molecules at mesospheric altitude have an important role to play in deciding sodium airglow intensity.

The measurements of both neutral sodium atoms and sodium airglow intensity are crucial as they can be used as tracers to investigate dynamical processes in mesosphere such as gravity waves and tides. Narrow line-width lidar observations of the hyperfine structure of the Na D lines have also been used to measure the temperature and wind with excellent precision [e.g. *Gibson et al.,* 1979]. The temperature and wind in mesosphere are modulated by atmospheric gravity waves and, therefore, these parameters can be measured to investigate gravity waves.

1.4 Atmospheric Gravity Waves

The recent investigations have yielded a more detailed understanding of gravity waves in mesospheric region on many fronts. Ground-based observational studies using VHF, MF and meteor radars in the low latitudes over Indian longitudinal sector have contributed substantially to the knowledge of wavelength range, amplitudes, momentum fluxes and spectra of gravity waves [e.g. *Gurubaran and Rajaram,* 2001; *Ramkumar et.al.,* 2006; *Antonita et al.,* 2008]. These investigations have thrown light on the instabilities, dynamics, vertical propagation, variations with altitude, as well as seasonal and geographic variabilities. Recent theoretical and numerical studies have addressed source characteristics, scales, spectral character, evolution, energy transfers, instability dynamics, wave–wave and wave–mean flow interactions, and the implications these effects for atmospheric circulation and structure [*Fritts and Alexander,* 2003]. The wave–wave and wave–mean flow interactions in MLT region can create several interesting phenomena like mesospheric bore events [*Narayanan et al.,* 2009, 2010].

The basic equations that govern the motion of gravity waves are as follows

$$\rho_0 \frac{\delta U_x}{\delta t} = -\frac{\delta p}{\delta x} \tag{1.8}$$

$$\rho_0 \frac{\delta U_z}{\delta t} = -\rho g - \frac{\delta p}{\delta z} \tag{1.9}$$

$$\frac{\delta p}{\delta t} + U_z \frac{dp_0}{dz} = c^2 \left[\frac{\delta \rho}{\delta t} + U_z \frac{d\rho_0}{dz} \right] \tag{1.10}$$

$$\frac{\delta \rho}{\delta t} + U_z \frac{d\rho_0}{dz} + \rho_0 \left[\frac{\delta U_x}{\delta x} + \frac{\delta U_z}{\delta z} \right] = 0 \tag{1.11}$$

Where, U_x and U_z are wave velocity components in the x (horizontal) and z (vertical) directions respectively.
p and ρ => Atmospheric pressure and density respectively.
p_0 and ρ_0 => Unperturbed atmospheric pressure and density respectively.
c (speed of sound) $= \frac{\gamma p_0}{\rho_0}$, γ is ratio of specific heat.

After solving the these equations, the dispersion relation for gravity waves turns out to be as follows

$$\omega^4 - \omega^2 c^2 (k_x^2 + k_z^2) + (\gamma - 1) g^2 k_x^2 + \omega^2 \gamma^2 g^2 / 4c^2 = 0 \tag{1.12}$$

where, ω is the angular frequency, k_x and k_z are the wave numbers of gravity waves in the horizontal and vertical direction respectively and g is the acceleration due to gravity.

Rearranging the equation 1.12, we get

$$k_z^2 = \left(1 - \frac{\omega_a^2}{\omega^2}\right) \frac{\omega^2}{c^2} - k_x^2 \left(1 - \frac{\omega_b^2}{\omega^2}\right) \tag{1.13}$$

where,

$$\omega_a = \gamma g/2c$$

$$\omega_a = (\gamma - 1)^{\frac{1}{2}} g/c$$

The waves can propagate if k_x and k_z are real and positive. This requires either $\omega > \omega_a$ or $\omega < \omega_b$ and these are called acoustic and gravity wave regimes respectively. Figure 1.11 represents a typical propagation of a gravity waves in atmosphere. The air particles move perpendicular to the direction of phase propagation. Thus, the phase velocity of the upward propagating gravity wave will be always directed downward. If viscous effects are neglected, the energy travels at the right angles to the phase velocity. The wave amplitude increases with altitude which varies as the square root of the air density in order to maintain the energy flux at a constant value.

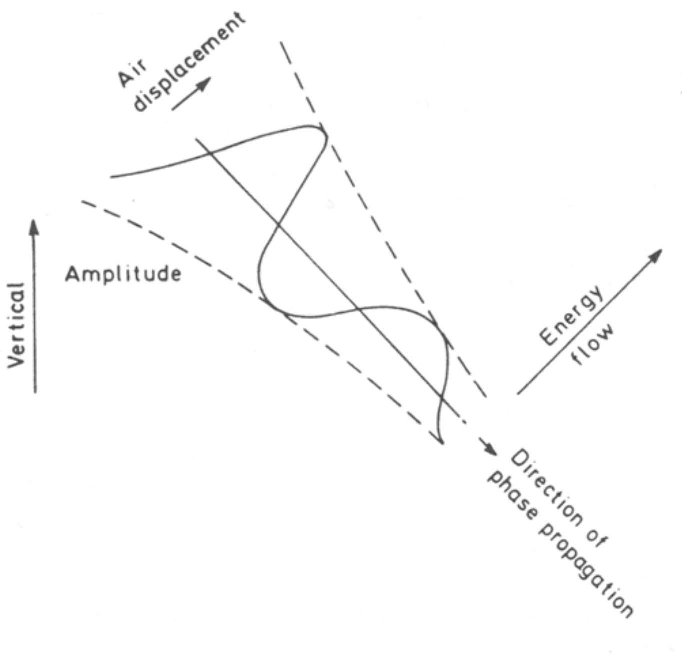

Figure 1.11: Propagation of gravity wave (Based on the work of *Hines,* 1963. Reproduced from *Hargreaves,* 2002).

The parameters ω_a and ω_b are known as the *acoustic resonance frequency* and *Brunt-Vaisala resonance frequency* respectively. The first is the resonant frequency of the atmosphere in the acoustic mode, when the restoring frequency is due to compression. The Brunt-Vaisala resonance is the natural resonance of a displaced parcel of air within the atmosphere when buoyancy is the restoring force. Figure 1.12 represents a synoptic view of the gravity waves in different modes. As discussed above, the waves can propagate if either $\omega > \omega_a$ or $\omega < \omega_b$ and known as 'acoustic waves' and 'internal gravity waves' respectively. The waves are called 'evanescent' if $\omega_a > \omega > \omega_b$ and under this condition, the waves cannot propagate through atmosphere.

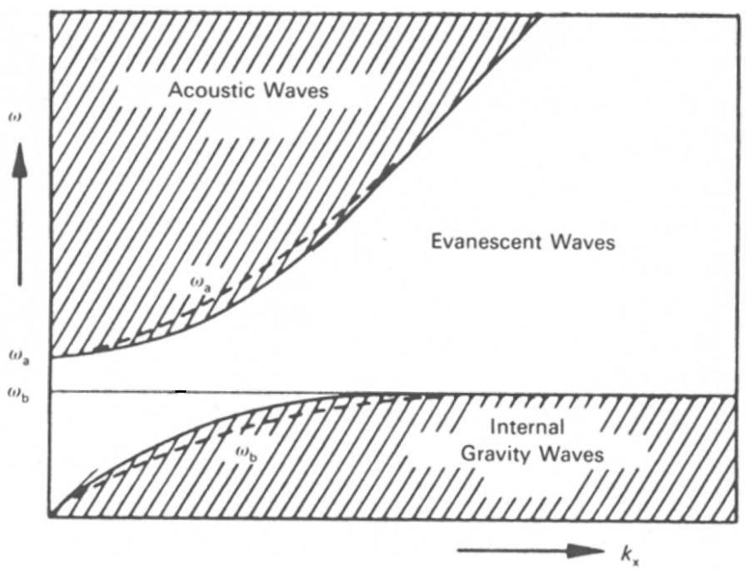

Figure 1.12: The acoustic, evanescent and gravity regimes of acoustic-gravity waves (Based on the work of *Hines,* 1963. Reproduced from *Hargreaves,* 2002).

As discussed earlier, variations in the neutral sodium atom concentration and sodium airglow layer can be used as tracer to investigate the propagation and characteristics of gravity waves in the MLT region. *Rowlett et al.* [1978] carried out lidar observation which showed wave–like structures in the sodium layer which moved downward with time. The waves have typical wavelengths of 4-11 km and phase velocities of less than 1 m/s. *Hickey and Plane* [1995] investigated gravity wave driven fluctuations in sodium layer using a linear chemical-dynamical model. Their calculations indicate that the sodium layer can be treated as a tracer of gravity wave motions above 85 km. Since gravity wave perturbations have a timescale extending to around 3 hours, this implies that the lifetime of sodium in mesosphere is more than the typical timescale of gravity waves. Recently, *Xu and Smith* [2003] calculated the chemical lifetime of mesospheric sodium layer. The lifetime is more than a day in the vicinity of the mesospheric sodium layer and is much longer than the traditionally defined chemical lifetime for sodium of a few minutes. Therefore, the passage of gravity waves can redistribute the neutral sodium layer. The gravity waves have substantial influences on the structure of neutral sodium layer and are mostly responsible for the night-to-night variability [*Plane et al.,* 1999a]. Using the perturbation in sodium layer, several parameters can be derived. As discussed earlier, the phase velocity of a upward propagating gravity waves will be always directed downward (shown in Figure 1.11). Figure 1.13 reveal the stacked time series profiles of neutral sodium atoms measured over Gadanki that show the presence of downward phase progression (showed by inclined lines in Figure 1.13) clearly indicating the signature of gravity waves perturbation in neutral sodium layer.

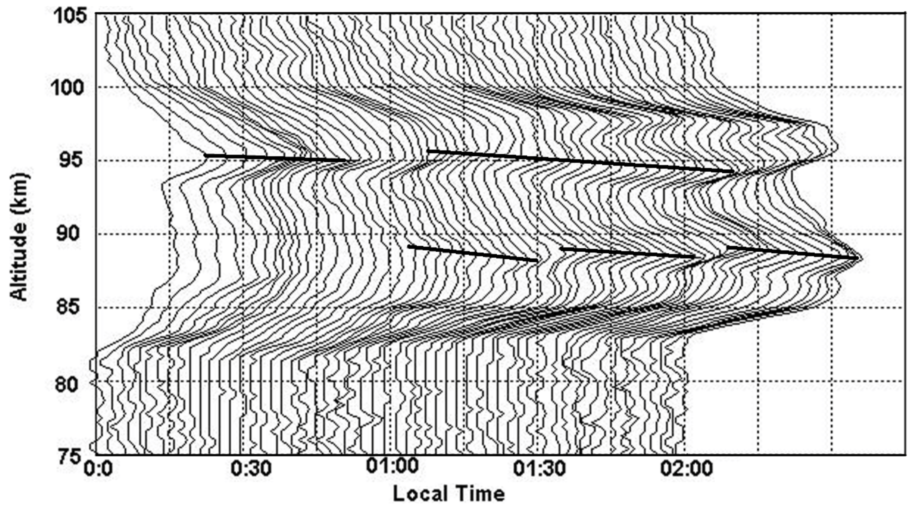

Figure 1.13: Time series of sodium density profiles measured over Gadanki during 10-11 January, 2005. The bold slant lines indicate the downward phase propagation (After *Bhavani Kumar et al.,* 2007b).

Similar to neutral sodium atom layer, sodium airglow emission is also used as a tracer to investigate gravity waves in mesosphere. The reaction time constant of sodium airglow in the Chapman mechanism being around a few seconds [*Plane et al.,* 1993], the perturbation caused by the gravity waves having periods greater than the reaction time constant can, in principle, be captured. Using ground-based observations of the mesospheric sodium nightglow emissions, several investigators have reported wave-like structures in the spatial and temporal variations of the sodium airglow emission [e.g. *Molina,* 1983; *Fagundes et al.,* 1995]. The wave-like structures observed in the mesospheric nightglow intensity variations were attributed to the passage of gravity waves, which are generated in the lower atmospheric regions. Several investigators have presented theoretical considerations related to the interaction between gravity waves and mesospheric nightglow emissions [e.g. *Hines and Tarasick,* 1993]. Gravity waves propagating through the upper atmosphere in the low-latitude regions with periods of around 60 min were reported by *Fagundes et al.,* [1995].

The gravity waves interact with the atmosphere in several ways. As the wave propagate upward, the negative density gradient causes their amplitudes to grow. At some point of amplitude of the wave will force local temperature gradient to exceed the adiabatic lapse rate. This is the condition where the wave become unstable and is expected to break [*Lindzen,* 1981] and causes turbulence to prevent further growth. This process is also referred to as saturation. The dissipation of these waves cause turbulent mixing and deposition of heat to the medium. Vertical mixing transfers momentum between layers of atmosphere. If the wave has a phase speed that differs from the mean flow, the breaking of wave can provide energy and momentum source that accelerate or retard the background motion [*Fritts,* 1984; *Fuller-Rowell,* 1995]. If the wave phase speed matches with the background wind field, strong absorption occurs that leads to the energy and momentum deposition to the ambient and consequently play a significant role in the wind and temperature variability in upper mesosphere [*Krishna Murthy,* 1998].

Instability processes cause the gravity waves to break into smaller scale sizes. It is considered that there are two ways for instabilities to occur in the MLT region. One is dynamical instability mechanism, and the other is convective instability mechanism. The dynamical instability occur due to wind shear in the background horizontal wind field whereas, the convective instability appears when the temperature gradient exceeds the adiabatic lapse rate. Figure 1.14 shows an event of breaking of gravity waves in OH airglow images. The time sequence of the OH images reveals that a large scale gravity wave break into ripples in the MLT region due to those instabilities.

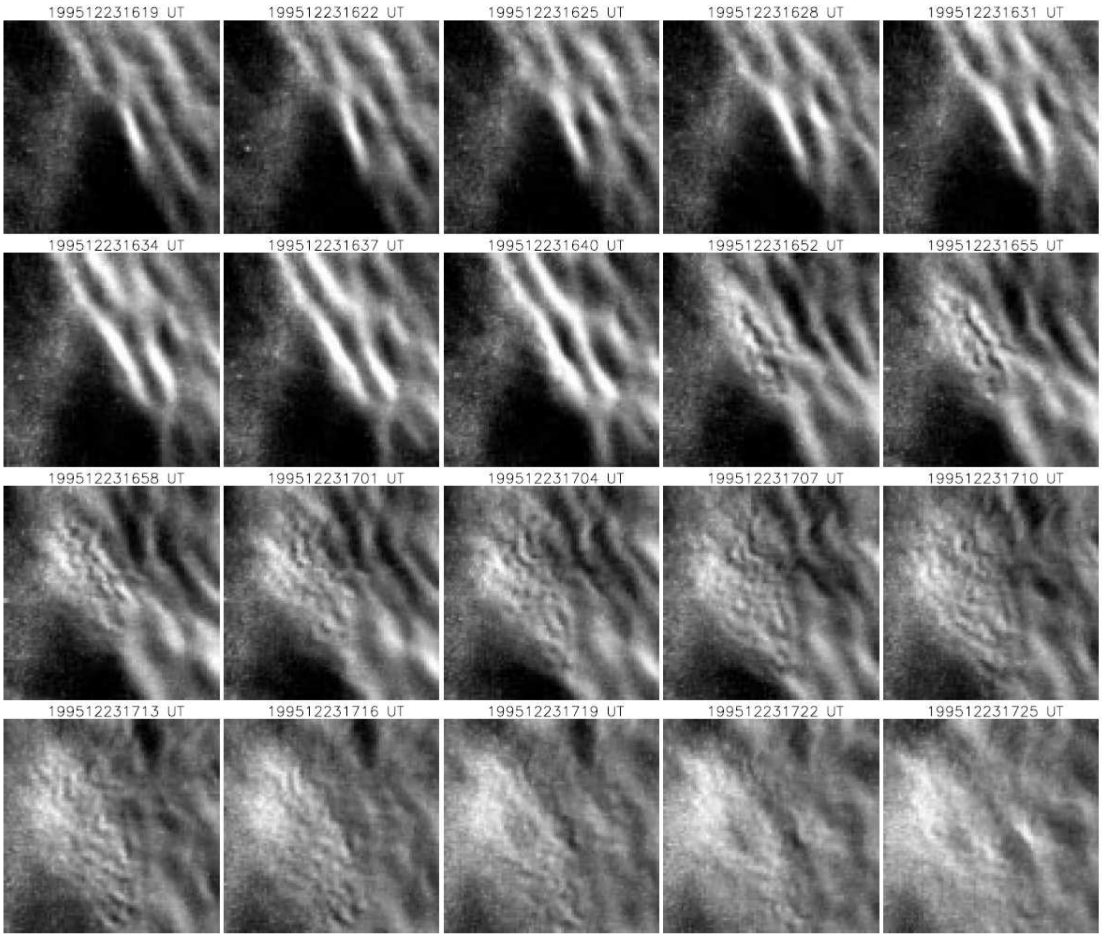

Figure 1.14: Breaking of gravity waves observed in OH airglow images during the period of 1619–1725 UT on December 23, 1995. The last four digits at top of each image give universal time of image acquisition. (After *Yamada et al.,* 2001).

The breaking of these waves near mesopause region can produce secondary waves [*Vadas et al.,* 2003] and propagate upward that reach Thermosphere Ionosphere System (TIS). In recent times, significant evidences have been obtained that indicate strong influence of Atmospheric Gravity Waves [e.g. *Meriwether,* 1996] in the dynamics of TIS. Mesopause being the interface between the middle and upper atmosphere, it plays crucial role in deciding the gravity wave modes propagating to TIS and generating plasma irregularities that have enormous implications in satellite communication and navigation purposes.

1.5 Thermosphere Ionosphere System

Thermosphere-Ionosphere is a mutually coupled system. Neutral processes affect the ionospheric phenomena and vice versa. Ionosphere has several layers depending on its physical properties. It is classified into three distinct layers D, E and F. In D layer the ion-neutral (ν_{in}) and electron-neutral (ν_{en}) collision frequencies are greater than their respective gyro frequencies (ω_i, ω_e). So both ions and electrons are governed by neutral wind. In the E region $\nu_{in} > \omega_i$ but, $\nu_{en} < \omega_e$. This means that the movement of electrons is controlled by the Earth's magnetic field, while ions are still controlled by collision. In F region both ions and electrons movements are governed by Earth's magnetic field. Molecular and atomic ions are the dominant ionic species in the E and F region respectively.

1.5.1 Thermospheric Airglow Emission

As discussed above, molecular ions below 160 km and atomic ions above 200 km are dominant. These ions recombine with the ambient electrons and on many occasions, metastable atomic excited states are produced during recombination process. The role of these metastable species has been comprehensively discussed in *Torr and Torr* [1982]. The metastable states have lifetimes much longer than typical lifetime for the spectroscopically allowed transitions observed in the laboratory. These are referred to the forbidden transitions as they violet the selection rules for the electric dipole transition. However, these are allowed transitions if higher order electric moments and magnetic dipole moments are considered. The atoms in metastable states can only exist under low ambient density where the probability of collisional de-excitation is significantly less. Thus, the atoms in metastable states are preferred to occur in thermosphere where neutral collisional frequency is less due to low ambient density (referred to Figure 1.1).

OI 630.0 nm and 777.4 nm are the two thermospheric airglow emissions that occur in the altitude region of 250 and F region peak respectively during nighttime. The emission 777.4 nm occurs mainly due to radiative recombination of O^+ ions with electrons in the peak F region altitude (~300 km). On the other hand, the dominant process for the OI 630.0 nm airglow emission during nighttime is dissociative recombination of O_2^+ ions with electrons. These thermospheric airglow emissions are extensively used as tracers to investigate the dynamics of F region plasma irregularities. In the present thesis work, the results based on the observations of OI 630.0 nm airglow emission are also discussed.

1.5.2 Equatorial Spread F

In the F region over low and equatorial latitudes, several complex geophysical phenomena occur. One of them is Equatorial Spread F (ESF), which is a nighttime phenomenon. The name 'ESF' was derived based on observation during the initial years, wherein the plasma irregularities generated in the post sunset F region ionosphere manifested as spread in the return echo obtained on ionograms. The spatial scale sizes of these plasma irregularities structures span from a few hundred of kilometers to a few centimeters. The investigations of ESF events over low latitudes have been carried out extensively based on theoretical [e.g. *Ossakow,* 1981; *Sekar and Kelley,* 1998; *Sekar,* 2003] and experimental works [e.g. *Raghavarao et al.,* 1984, 1987; *Sridharan et al.,* 1997; *Prakash et al.,* 1991; *Iyer et al.,* 2003; *Sekar and Chakrabarty,* 2007; *Kelley,* 2009]. These plasma irregularities associated with ESF occur due to plasma instability processes assisted by the steep vertical gradient in electron density during post sunset hours. Due to recombination of ions in the E region during post sunset hours, the density of electron decreases. On the other hand, electron density is maintained in F region by the dynamical processes thus causing a steep gradient.

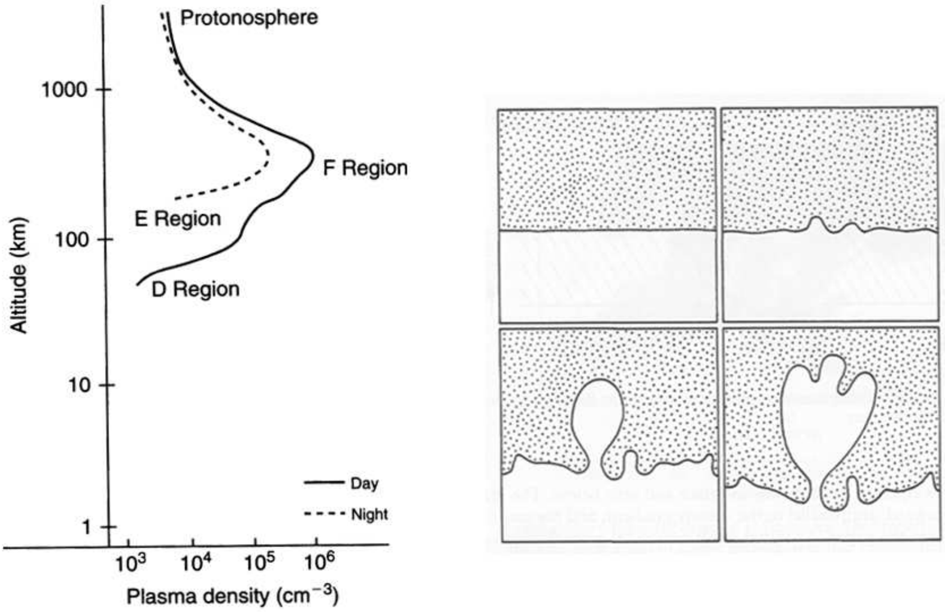

Figure 1.15: (Left) Plasma density profiles during day and night. (Right) Rayleigh Taylor instability (After *Kelley,* 2009).

Figure 1.15 represents typical profiles of plasma density during day and nighttime. It can be observed that the E region electron density during nighttime is significantly less than that in the F region. This steep gradient in the electron density is favorable for Rayleigh-Taylor (RT) [*Kelley,* 2009] instability to take place, which gives rise to F region irregularities during nighttime. it is well known that RT instability is the prime causative mechanism of ESF. This instability occurs when heavier fluid is supported by lighter fluid. As shown in Figure 1.15, a small perturbation in the fluid can generate instability in the medium that grows in space and time. Similar to the fluid, the nighttime ionosphere is unstable as the F region electron density is much larger in comparison with the E region. Thus, any perturbation can grow to generate irregularities in F region ionosphere.

The gravity waves which penetrate mesosphere may act as a seed perturbation to cause F region ionospheric irregularities. *Nicolls and Kelley* [2005] presented the evidence for gravity wave seeding of ionospheric plasma instabilities. Medium and shorter scale sizes gravity waves with downward phase velocity were identified to be causative agent to trigger ESF. Recently, a few simultaneous measurements of thermospheric OI 630.0 nm airglow and mesospheric OI 557.7 nm, NaD, O_2 and OH band emissions [e.g. *Takahashi et al.,* 2009; *Sreeja et al.,* 2009] over low latitude stations reveal the possible relation between the ESF activities in the ionosphere and gravity wave activity in the mesosphere.

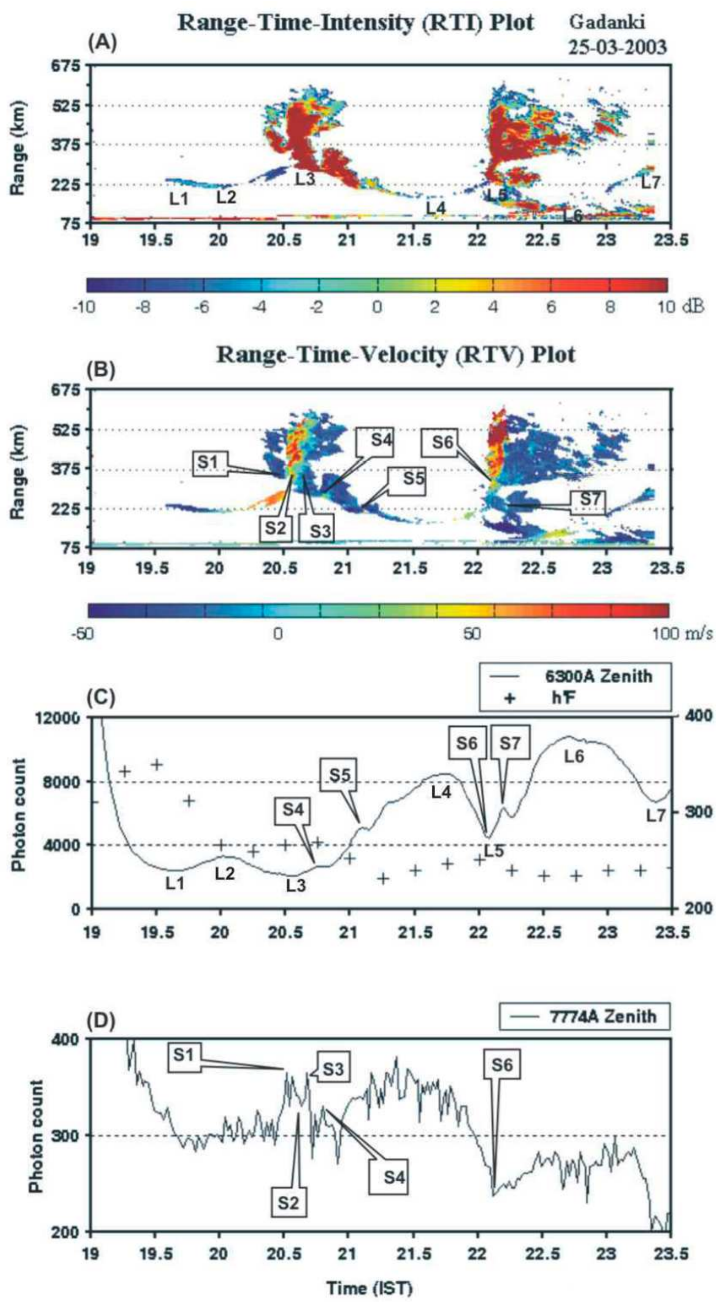

Figure 1.16: Composite plots of temporal variations of (A) Range and Intensity (RTI), (B) Range and Velocity (RTV), (C) 630.0-nm airglow intensity (solid line) along with hF (+) and (D) 777.4 nm airglow intensity on an equatorial Spread F night, 25 March 2003 (After *Sekar et al.,* 2004).

These atmospheric gravity waves play a crucial role in the generation of ESF. *Chakrabarty et al.* [2004] made an attempt to identify the preferred gravity wave modes over low and equatorial latitudes during geomagnetically quiet and disturbed periods. Several possibilities regarding the source region of these modes were qualitatively explored and identified to be the lower atmospheric origin. In addition, *Pallamraju et al.* [2010] identified the existence of short, medium and large periodicities in thermosphere based on OI 630.0 dayglow emission over low latitude. These gravity waves may act as seed perturbation during the post sunset hours and trigger the plasma instabilities that generate ESF.

Figure 1.16 represents optical observations obtained on an ESF night that exhibit macro and micro intensity variations in OI 630.0 nm airglow emission. As expected from the Barbier relation [*Barbier,* 1959], the macro variations in the airglow intensities are found to be anti-correlated with the variation of the base height of F region. However, the smaller scale structures are controlled by the F-region electron density to the OI 630.0 nm emission intensities. The bottom envelope of the F region show wave–like structures on the RTI map. As discussed in *Sekar et al.* [2004], seed perturbation with more than one wavelength is required to give rise to a plasma enhancements structure known as blob.

1.5.3 Fossil Bubbles

Plasma plume structures, generated during post sunset hours, evolve in space and time. During post mid-night hours, these plasma bubbles become non-evolutionary and drift with the back ground wind. These bubbles in this phase are known as 'fossil bubbles'. The fossil bubbles lack 3 meter scale size irregularities and are transparent to VHF radar beam. As discussed in *Basu et al.* [1978], the meter scale structures detectable by VHF radars disappear during this non-evolving phase leaving larger scale structures in place. However, on occasions, these plasma bubbles with meter scale irregularities can be detected during post midnight hours. The origin of these meter scale size irregularities in the fossil bubble is due to neutral wind driven instability [*Kelley et al.,* 1981; *Sekar,* 1993]. The eastward wind can drive the instability when background electron density gradient is directed westward and vice versa. This instability make the fossil bubble active reappearance of 3 meter scale size irregularities that can be detected using VHF radar.

1.6 Scope of the Present Thesis

The radio and optical techniques used for this thesis work are described in Chapter 2. The author is involved in the development of some of the optical instruments such as photometers and imager. The radio techniques include the VHF radar and HF (ionosonde) observations. On the other hand, optical techniques describe the observations using airglow photometers, sodium resonance lidar and satellite borne measurements.

Simultaneous measurements of sodium atom concentration and sodium airglow over Gadanki, a low latitude station in Indian longitudinal sector are described in Chapter 3. The measurements reveal the importance of collisional quenching with the ambient atmospheric molecules on sodium airglow mechanism. In addition, the measurements suggest that the effect of collisional quenching on sodium airglow intensity is altitude dependent.

Results obtained due to passage of atmospheric gravity waves through neutral sodium atom and sodium airglow layer are described in Chapter 4. The temporal variations sodium airglow intensity enable to derive periodicities of gravity waves over Mt. Abu and Gadanki, India. Moreover, the temperature and wind profiles, obtained from SABER and TIDI instruments onboard TIMED satellite, over both the places showed the occurrence of convective and dynamical instabilities in sodium airglow layer on a few nights. An indication for the breaking of gravity waves is obtained.

The identification of fossil bubbles in F region ionosphere using VHF radar and OI 630.0 photometric measurements during post midnight hours is presented in Chapter 5. The neutral winds were suggested to destabilize the bubbles and made them active.

The important results from the present thesis work are summarized in Chapter 6. Future directions are also indicated.

Chapter 2

Experimental Techniques: Radio and Optical

2.1 Introduction

Systematic investigation of terrestrial upper atmosphere can be carried out using remote sensing techniques. Remote sensing is the technique where the properties of medium are deduced without placing any instrument in the medium. Active and passive remote sensing techniques are the two types which are widely used to explore upper atmosphere. In active remote sensing technique, a probing wave (electromagnetic or acoustic) is transmitted into the medium and scattered/reflected signals are detected. RADAR (RAdio Detection And Ranging) and LIDAR (LIght Detection And Ranging) are a few examples of the active remote sensing techniques. In passive remote sensing technique, emissions occurring naturally within the medium are recorded. Monitoring the natural emissions from the atmospheric species such as airglow is an example of passive remote sensing. The faint emissions by the atmospheric constituents in different wavelengths originated due to photochemical and/or chemical reactions, which is of global nature, non thermal and with the exceptions of the radiations associated with events like lightning and meteor trails, etc is known as airglow. Airglow photometry, spectrometry and imaging are passive remote sensing techniques.

In order to fulfil the scientific objectives of the present work, airglow photometers and imager were developed and fabricated in-house at Physical Research Laboratory, Ahmedabad. These optical instruments were operated from Mt. Abu (24.6° N, 72.7° E) and also at Gadanki (13.5° N, 79.2° E) in conjunction with the facilities like Very High Frequency (VHF) radar and sodium lidar at National Atmospheric Research Laboratory (NARL). Simultaneous observations using the above mentioned radio and optical techniques were carried out from 2006 to 2009 during moonless period in cloudless season. These coordinated observations were occasionally supplemented by the High Frequency (HF) radar (ionosonde) observations at Thumba (8.5° N; 77.0° E) a dip equatorial station.

2.2 Radio Techniques

The scattering of radio waves depends on the changes in the radio refractive index of the medium. A radar is able to resolve the changes in the scattering medium when the Inter Pulse Period (IPP) (inverse of the Pulse Repetition Frequency (PRF)) of the radar beam is less than the characteristic time scales of the medium. The propagation of radio wave in the upper atmosphere is affected by the plasma density and the fluctuations in it.

2.2.1 VHF Radar

The Indian MST (Mesosphere Stratosphere Troposphere) radar at Gadanki is basically a VHF radar that operates at 53 MHz frequency whose peak power aperture product can go up to 3×10^{10} W.m^2. The MST radar system includes 1024 (32×32), three element, cross-polarized Yagi antennas with 32 high power trans-receiver duplexers and phase coherent receivers. The detailed specifications of this radar are available in literature [*Rao et al.,* 1995]. The MST radar can also be operated at coherent pulsed mode to receive echoes from ionospheric irregularities.

In the coherent backscatter radar mode, it is assumed that the transmitted beam is not significantly affected by the individual plasma fluctuations. Therefore, Born approximation is valid. Moreover, the characteristic length of scattering volume is considered to be much larger than the probing wavelength but not small for the medium so that the medium can be treated as the homogeneous. Under these conditions, if the radio wave travels through a medium with changing refractive index, it will be scattered due to the changes in the plasma refractive index obeying Bragg's condition.

$$\overrightarrow{k} = \overrightarrow{k_i} - \overrightarrow{k_s} \tag{2.1}$$

where $\overrightarrow{k_i}$, $\overrightarrow{k_s}$ are respectively the wave vectors for the incident, scattered waves and $\overrightarrow{k}$ is the corresponding wave vector in the medium. This is known as Bragg's condition.

Now, in the case of backscattering,

$$\overrightarrow{k_s} = -\overrightarrow{k_i} \tag{2.2}$$

Therefore,

$$|\overrightarrow{k}| = 2|\overrightarrow{k_i}| \tag{2.3}$$

In wavelength domain,

$$\lambda = \frac{\lambda_i}{2} \tag{2.4}$$

This suggests that the radar beam will be able to probe plasma density fluctuations with spatial scale sizes half of the radar wavelength. Therefore, the MST radar operated in ionospheric mode can probe nearly 3 meter scale size plasma irregularities. These plasma irregularities are aligned to the geomagnetic field lines. As a consequence, the return echo is highly aspect sensitive. Aspect sensitivity refers to the dependence of the backscattered echo power with the angle of incidence of the radio wave. The echo power decreases when the incident angle increases. Therefore, the beam of radar is oriented orthogonal to geomagnetic field lines in order to receive the maximum backscatter echo power. In the present case, the beam of MST radar in ionospheric mode is oriented 14.8° N from the zenith to make the beam orthogonal to the field aligned F region plasma irregularities also nearly orthogonal to the E region plasma irregularities. It is apparent that this perpendicularity condition holds for an extremely narrow radar beam at both E and F regions. Since, the radar beam divergence is only 2.8° it satisfies the orthogonality condition over a broad altitude range from E to F region. The other radar parameters for investigating Equatorial Spread F (ESF) irregularities and the operations of MST radar in ionospheric mode are available in literature [*Chakabarty,* 2007].

Based on the average power spectrum, the following low order spectral moments are derived [*Chakabarty,* 2007; *Venkateswara Rao*, 2008].

The Zeroth moment represents the total power of the backscatter echo and can be expressed as,

$$M_0 = \sum_{i=l}^{u} P_i \tag{2.5}$$

Therefore, the Signal-to-Noise-Ratio (SNR) in dB is

$$SNR = 10 \log \left(\frac{M_0}{N.L} \right) \tag{2.6}$$

where N represents the total number of Doppler bins and L is the mean noise level. Hence, the product of N and L gives the total noise level over the whole bandwidth.

The First moment is the weighted mean Doppler shifts (line-of-sight phase velocity).

$$M_1 = \frac{1}{M_0} \sum_{i=l}^{u} P_i f_i \tag{2.7}$$

The Second moment represents the variance which is a measure of dispersion from the mean frequency

$$M_2 = \frac{1}{M_0} \sum_{i=l}^{u} P_i (f_i - M_1)^2 \tag{2.8}$$

In the above expressions of the moments, P_i and f_i are the powers and frequencies corresponding to the Doppler bins within the spectral window. l and u are the lower and upper limits of the Doppler bin of the spectral window. In the present work, all the three moments M_0, M_1 and M_2 are used respectively to construct Range-Time-Intensity (RTI), Range-Time-Velocity (RTV) and Range-Time-Width (RTW) maps of F region plasma irregularities.

2.2.2 HF Radar (Ionosonde)

In addition to the VHF radar, HF radar (ionosonde) is also used to investigate F region ionosphere. However, the working principle of ionosonde is different from the VHF radar mentioned earlier. The principle of ionosonde relies on the total reflection of HF radio waves (~2-30 MHz) from different parts of the ionosphere. The propagation of HF radio waves is affected when the plasma refractive index changes due to variation in plasma density (N_e). The simplified expression for the plasma refractive index can be obtained from the Appleton-Hartree equation if the effects due to collisions and Earth's magnetic field are neglected.

$$n^2 = 1 - \frac{\omega_N^2}{\omega^2} \tag{2.9}$$

where ω is the angular frequency of the incident HF radio wave and ω_N is the angular frequency of plasma which is given by

$$\omega_N = \left(\frac{N_e e^2}{\epsilon_0 m} \right)^{\frac{1}{2}} \tag{2.10}$$

It is clear from equation 2.9 that the HF radio waves are totally reflected from the ionosphere, when the incident radio wave frequency is equal to the plasma frequency at each altitude region. The transmitted HF wave is swept in frequency and the echo time is recorded as a function of frequency. Using these information, the altitude profile of electron density can be constructed. As the electron density increases till the F region peak height, the plasma refractive index gets smaller and becomes zero at F region peak height at a particular HF radio wave frequency (equation 2.9). Hence, ionosonde can provide information up to F region peak altitude. The electron density (N_e) in the ionosphere can be derived using the following expression

$$f_N = (80.5 N_e)^{\frac{1}{2}} \tag{2.11}$$

where N_e is in cm^{-3}

f_N is in kHz

Based on the frequency (f_N) versus height curve, several other ionospheric parameters like base height and peak height of F region can be derived.

2.3 Optical Techniques

As indicated earlier, airglow emissions can be used as a tracer to investigate upper atmosphere. In view of this, instruments like airglow photometer and imager have been developed and used extensively as passive remote sensing techniques. Airglow photometry is the technique where the temporal variation of the integrated intensity is recorded at particular wavelength of airglow emission. On the other hand, airglow imager can provide the spatial information in the horizontal plane of the emission region for a particular duration at a particular wavelength of interest. Sequences of image can provide temporal information.

Sodium lidar is an active remote sensing technique and vastly used to study upper atmosphere especially mesosphere and lower-thermosphere region. Sodium lidar can provide the concentration profile of neutral Na atoms at mesospheric heights and is extremely important to deduce the perturbation caused by atmospheric wave activities.

2.3.1 Multi-Wavelength Airglow Photometer

In order to measure the intensities of thermosphere and mesosphere airglow emissions, a multi-wavelength airglow photometer (shown in Figure 2.1) was designed and developed at Physical Research Laboratory, Ahmedabad. This photmeter has $\frac{f}{2}$ optics maintained throughout the optical path. It comprises of front-end optics, filter section and a detector. In order to observe from various spatial directions, a mirror arrangement was fitted on the top of the photometer. The elevation-azimuth movements of mirror and the movement of the filter wheel are controlled through a computer.

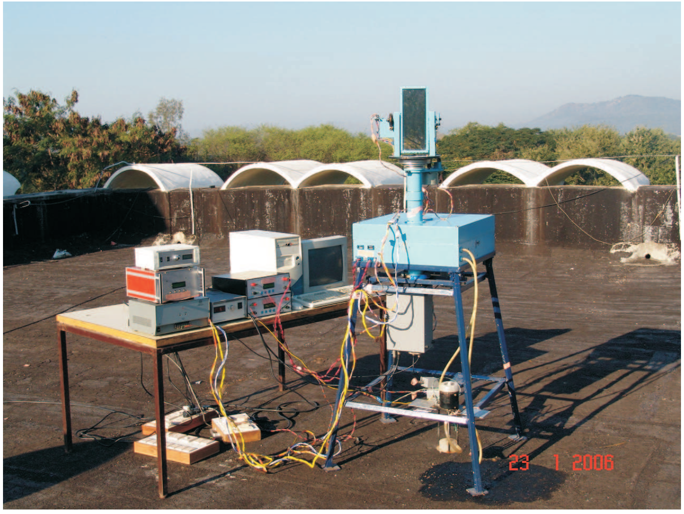

Figure 2.1: The set up of the multi-wavelength photometer at the Indian MST radar site, Gadanki (After *Chakrabarty,* 2007).

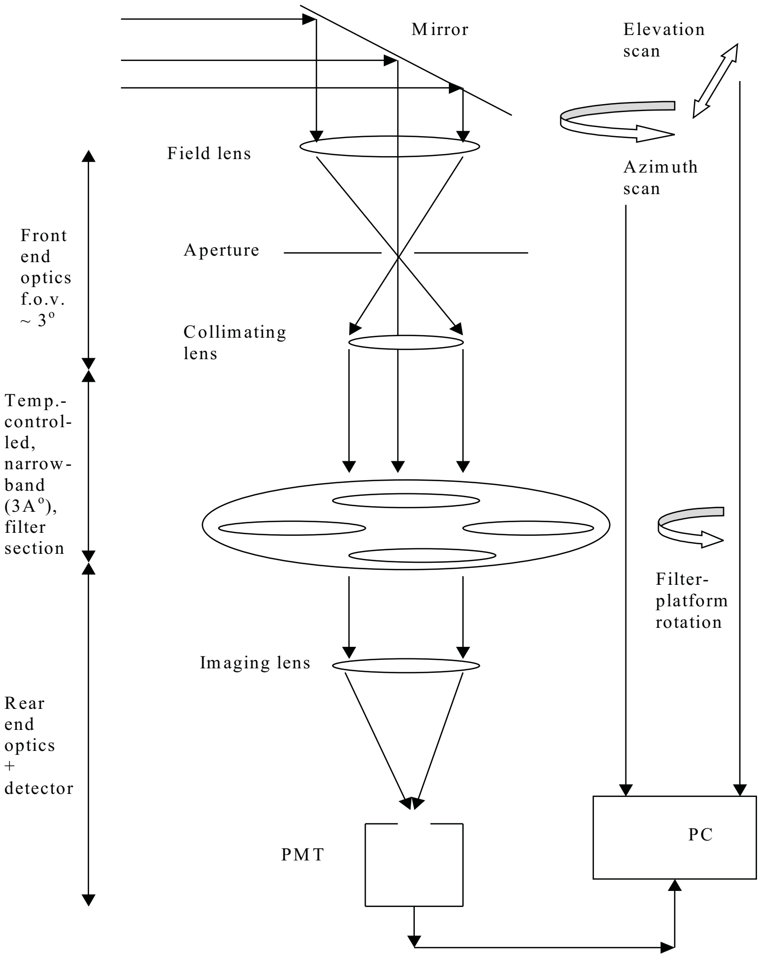

Figure 2.2: Optical schematic diagram of the multi-wavelength photometer (After *Chakrabarty,* 2007).

The front-end optics of this photometer consists of several optical elements like field lens, collimating lens and imaging lens (shown in Figure 2.2). In addition, a field stop is introduced at the focal plane of the field lens to restrict the field-of-view (FOV) to 3° in order to match with the VHF radar beam width. The field lens with an aperture is used to make the desired FOV and the rays are further collimated using collimating lens. The collimating lens is kept before the filter wheel arrangement portion to make the beam parallel that gets incident on the interference filter. Narrow band-width (0.3 nm) filters tuned to 23 °C are chosen in the present investigation in order to minimize the unwanted sky background noise. The four-position filter wheel, attached to the system, is programmed to align the desired filter in the optical path. All the filter slots are temperature tuned with an accuracy of ±0.2 °C. The filtered beam is now focussed on the photomultiplier tube (Type S-20; EMI 9863A) which has an in-house temperature controller unit (FACT 50; EMI). The detailed description of each components of multi-wavelength photometer and the coordinated VHF radar observations of ESF irregularities are available in literature [*Sekar et al.,* 2004, 2008; *Chakrabarty,* 2007].

2.3.2 Single-Wavelength Portable Airglow Photometer

The multi-wavelength photometer is not easily transportable. As part of the thesis work, the necessity to make observations from several vantage points simultaneously with other measurement techniques was realized. Therefore, two suitable miniaturized, single wavelength photometers were developed. These portable photometers capable of measuring mesospheric Na airglow emission intensity, were designed and fabricated at Physical Research Laboratory (PRL), India with field of view of 3°. A temperature-controlled narrow band (0.3 nm) interference filter with the central wavelength around 589.1 nm was used in one of the photometer. Another mini-photometer with similar configuration was also made that contained interference filter of band-width 0.6 nm with central wavelength 589.0 nm. These photometers were operated in campaign modes from Mt. Abu (24.6° N, 72.7° E) and Gadanki (13.5°N, 79.2°E) during 2006-2009. The observations made by these portable photometers were inter-compared with the observations by multi-wavelength photometer for the same airglow emission line.

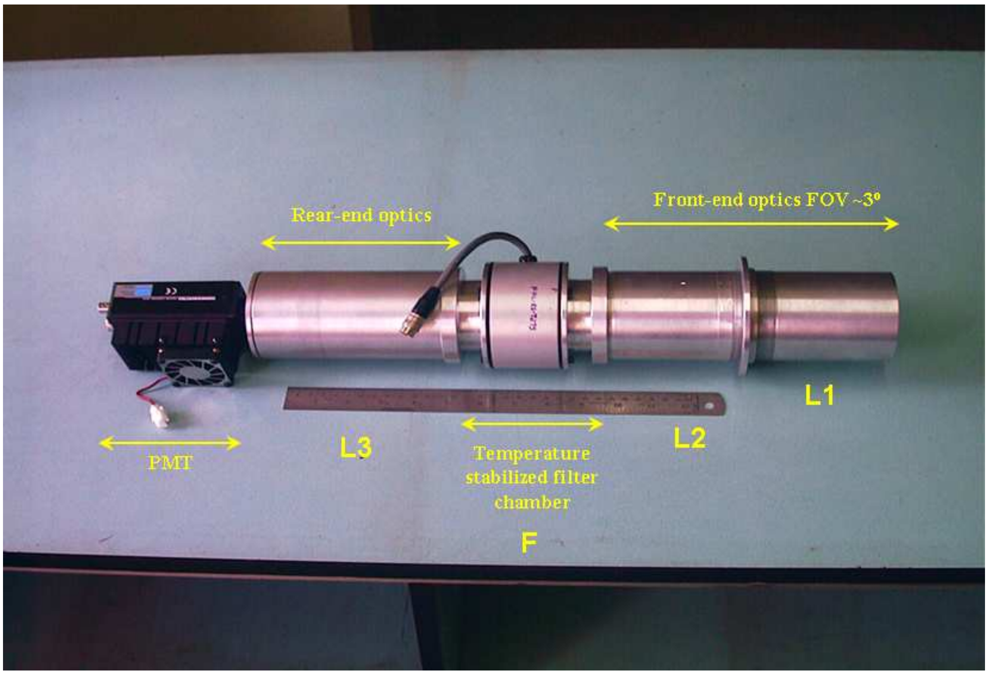

Figure 2.3: The set up of the portable mini-photometer during laboratory testing phase.

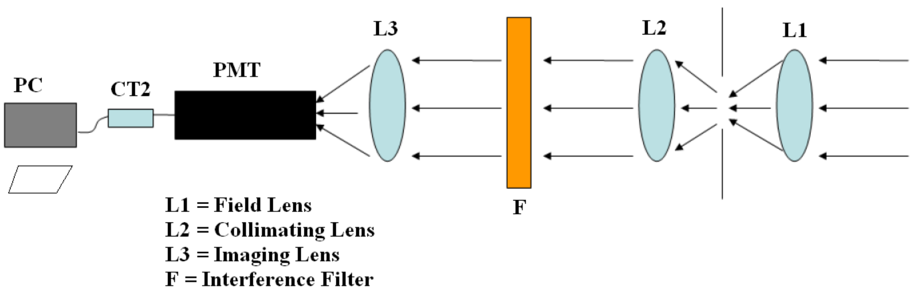

Figure 2.4: Optical schematic of the mini-photometer.

Figure 2.5: The set up of the mini-photometer at the Na lidar site, Gadanki.

The mini-photometer comprises of front-end optics, temperature stabilized filter chamber, rear-end optics and photomultiplier tube (Figures 2.3 and 2.4). The field lens and the aperture in the front-end optics decide the FOV (3°) of the photometer. The collimating lens converts incoming rays into parallel beam before they are incident on the interference filter.

Interference filters are multi-layer thin film devices. An interference filter is basically a lower order Fabry-Perot interferometer. A Fabry-Perot interferometer [*Thorne et al.,* 1999] normally consists of two glass or fused silica plates with the front surfaces flat and parallel. The front surfaces of the plates are coated with materials of high reflectivity. The incident rays undergo multiple reflections and interference. The spectral rejection of undesired wavelengths is carried out using destructive interference principle. On the other hand, the desired wavelength undergoes constructive interference. A narrow-band interference filter consists of several cavities separated by absentee layers. Each cavity consists of multiple layers of alternate high (e.g. Zinc Sulphide) and low refractive index (e.g. Cryolite) each with $\frac{\lambda}{4}$ thickness, that drastically reduces the transmission of un-desired wavelengths by destructive interference.

The central wavelength of the pass-band shifts towards the lower wavelength if the angle of incidence deviates from zero. The wavelength of the peak transmittance at small angles (ϕ) is given by

$$\lambda(\phi) = \lambda_0 \sqrt{1 - \left(\frac{n_0}{n_e}\right)^2 \sin^2 \phi} \tag{2.12}$$

where n_0 and n_e are the refractive indices of external medium (n_0=1.0003 for air) and for the spacer material.

The temperature has important role to play in altering the central wavelength of the filtered signal as, the deviation in temperature affects the thickness and refractive index of the material. Therefore, it is necessary to maintain the temperature of filter chamber. The interference filters, used in the present case, are tuned to 35 °C. As the ambient temperatures during nighttime at the observational sites (Mt. Abu and Gadanki) are always less than 35 °C, heating-type filter chamber is used to maintain the temperature.

The filtered rays are focussed on the cathode of a **photomultiplier tube** (PMT) by the imaging lens housed in the rear end optics section. A PMT consists of photocathode, series of dynodes and anode. Photoelectrons are generated when photons strike photocathode due to photoelectric effect. These primary electrons are attracted to the additional electrodes known as dynodes and are maintained at a potential in such a way so that the potential difference between the $(n+1)^{th}$ and n^{th} dynode is always positive. Each dynode generates 10^5 to 10^7 secondary electrons for each incident electron. Thus the series of dynodes create the cascade of secondary photoelectrons that are finally accumulated on the anode to form a pulse. The pre-amplifier attached to the last dynode enhances the signal strength. The discriminator discards the noise in order to increase the signal-to-noise ratio. The photocathode of the PMT (Hamamatsu H7421-50) used in the mini-photometer is Gallium Arsenide (GaAs). The quantum efficiency of this PMT at 589.1 nm is around 10%.

The PMT has a built-in thermoelectric cooling unit (cools up to -20 °C) in order to minimize the thermal noise level. The PMT in the mini-photometer is operated in counting mode as the airglow signal strength is weak. As the statistic of the photon counts for a given input (I) follows Poisson distribution, the noise associated with it is $\sqrt{I}$. The data acquisition system attached to the counting unit records the temporal variation of airglow intensity in terms of the photon counts/s.

It may be noted here that due to a technical problem only one mini-photometer was calibrated against a standard source [Labsphere INC., USS-1200 V] which is generally used for calibration of satellite borne imaging payloads at the Space Application Centre (SAC), Indian Space Research Organisation (ISRO), Ahmedabad. The results obtained, using this calibrated photometer at Na D_2 airglow emission line (589.0 nm) in conjunction with Na lidar for a few nights during March, 2007 from Gadanki, are discussed in Chapter 3. As the airglow intensity variations are modulated by the passage of gravity waves, the relative intensity fluctuations from both the photometers are used in order to derive the periodicities of gravity waves. This aspect is discussed in detail in Chapter 4.

2.3.3 Sodium Resonance Lidar

The sodium lidar system at NARL, Gadanki is a tunable dye laser pumped by a pulsed Nd:YAG laser (shown Figure 4.6). It is useful to characterize atmospheric gravity waves by measuring mesospheric neutral Na atom concentration at different times. The sodium lidar consists of a transmitter and a receiver.

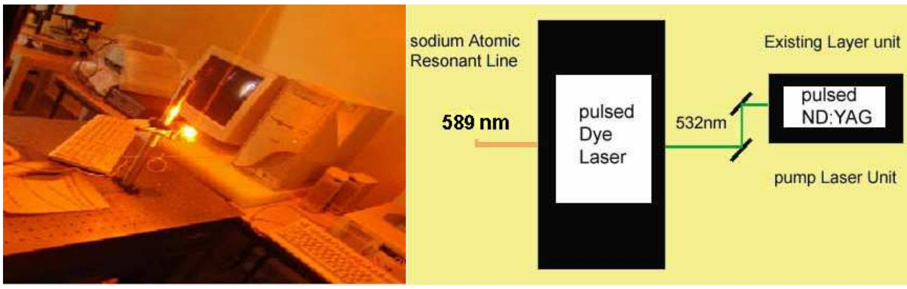

Figure 2.6: Sodium lidar system at Gadanki (Courtesy: NARL, Gadanki).

The laser **transmitter** consists of a tunable dye laser pumped by a Nd:YAG laser at second harmonic of Nd:YAG (532 nm). The output pulse energy is typically ~800 mJ at 50 Hz repetition rate with a beam size approximately 8 mm. The Nd:YAG laser is used to pump the dye laser which is a Continuum, Jaguar model D90DMA with dual grating system. The dye laser, with a narrow line-width (<0.05 cm^{-1} or about 2 pm), is equipped with two 90 mm holographic gratings. The dual grating system (2400 lines/mm) used in the first order diffraction regime and has a theoretical resolving power of 432000 that implies a wavelength resolution of about 2 pm at 589.16 nm wavelength. The final beam with energy per pulse (E_p) of around 12 mJ and beam divergence of 100 μrad is sent vertically into the sky using a mirror with high reflectivity.

The **receiver** system comprises of a telescope, interference filter, PMT and data acquisition system. The laser backscattered light is collected by a vertically fixed 750 mm diameter Newtonian telescope (F/3). An interference filter with center-wavelength of 589 nm and bandwidth 1.0 nm is positioned in front of the photon detector. A high gain PMT (Hamamatsu R3234) is used as the photon detector. The PMT is operated in counting mode in order to detect weak backscattered signals. The pulse signals from PMT are passed through a discriminator (Phillips model 6908) and then fed to a PC based multichannel analyzer (EG&G Ortec model MCS-PCI). The instrumental bin width is normally set at 2 μs, corresponding to a height resolution of 300 m. The photon count profiles are generated for each 6000 laser shots, corresponding to a time resolution of 120 sec. A data acquisition system is used to store the generated photon count profiles.

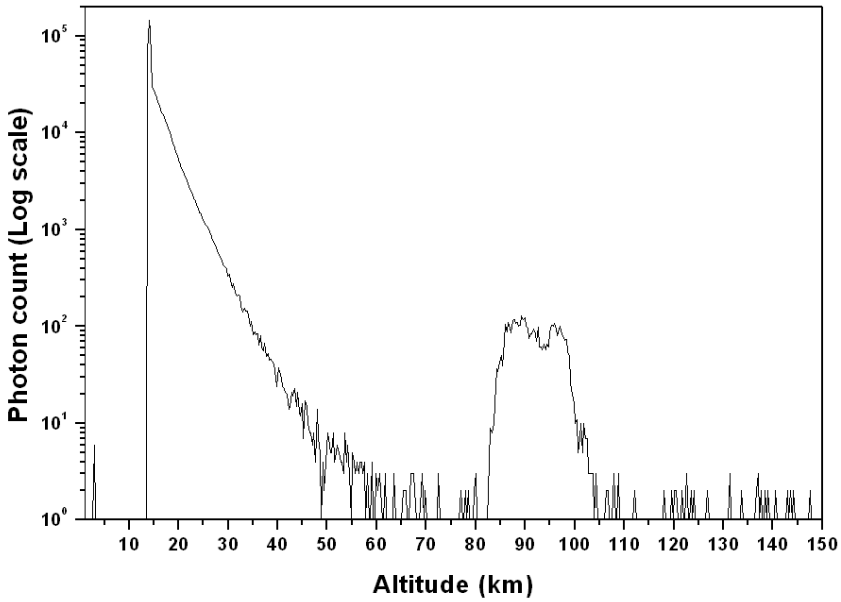

Figure 2.7: A typical photon count profile from the sodium lidar system at Gadanki [After *Bhavani Kumar et al.,* 2007a; *Vishnu Prashanth,* 2007].

Figure 2.7 shows a typical photon count profile from the sodium lidar. The resonant scattering from the Na layer can be clearly observed at altitudes above 80 to 105 km. The signal returns from above 35 and below 60 km and are due to Rayleigh scattering from atmospheric ambient molecules. The abrupt change in the returned signal below 12 km is due to electronic gating of the PMT. The details of the Na lidar system, operations and first observation of Na atom concentration over India are available in literature [*Bhavani Kumar et al.,* 2007a, 2007b; *Vishnu Prashanth,* 2007].

A sodium lidar transmits the 589.16 nm laser beam into the atmosphere and receives the laser backscattered signal from atmospheric molecules and neutral Na atoms due to Rayleigh and resonance scattering processes respectively. Following *Gardner* [1989], the total number of photons received by the telescope scattered from the neutral Na atoms at an altitude z and within the altitude range of Δz is expressed as

$$N_{Na}(z) = \left[\frac{P_L \Delta t}{hc/\lambda}\right][\sigma_{eff} n_s(z)\Delta z]\left[\frac{A_R}{z^2}\right][T_a^2(z)][\eta] + N_B \Delta t \tag{2.13}$$

Where,

$N_{Na}(z)$ = Number of photons detected in the range interval (z-Δz/2, z+Δz/2)

P_L = Laser power

Δt = Integration time

h = Planck's constant

c = Speed of light

λ = Lidar operating wavelength

$n_s(z)$ = Concentration of Na atoms in the range interval (z-Δz/2, z+Δz/2) due to Na atoms

N_B = Photon counts due to background noise and dark counts of detector

σ_{eff} = Effective back scattering cross-section of Na atoms

A_R = Area of Receiving telescope

$T_a(z)$ = One way transmittance of atmosphere

η = Efficiency of lidar system

Similarly, the total number of photons received due to Rayleigh scattering of atmospheric ambient molecules is given by

$$N_R(z) = \left[\frac{P_L \Delta t}{hc/\lambda}\right][\sigma_R n_A(z)\Delta z]\left[\frac{A_R}{z^2}\right][T_a^2(z)][\eta] + N_B \Delta t \tag{2.14}$$

Where,

z_R = Reference height

$N_R(z_R)$ = Number of photons due to Rayleigh scattering at height z_R

σ_R = Rayleigh scattering cross-section

$n_A(z)$ = Atmospheric neutral density

Thus, Na atom concentration is derived from photon counts using equations 2.13 and 2.14 (all parameters are in CGS units).

$$n_s(z) = \frac{z^2 \sigma_R n(z_R)[N_{Na}(z) - N_B]}{z_R^2 \sigma_{eff}[N_R(z_R) - N_B]} \tag{2.15}$$

In order to derive the Na concentration, z_R is taken to be 40 km where Rayleigh scattering significantly dominates over other scattering processes. The product of $\sigma_R n(z_R)$ can be calculated using the formula $\sigma_R n(z_R) = 3.539 \times 10^{-6} P(z_R)/T(z_R) m^{-1}$ [*Gardner,* 1989], where, $P(z_R)$ and $T(z_R)$ are the atmospheric pressure and temperature at height z_R and can be obtained from SABER instrument onboard TIMED satellite. The effective back scattering cross-section of Na atoms (σ_{eff}) is taken to be $5.17 \times 10^{-12} cm^2$ [*Bhavani Kumar et al.,* 2007a].

The maximum error involved in deriving Na atom concentration is around 10%. The measurements of Na atom concentration using lidar were carried out over Gadanki with time and height resolutions of 120 s and 300 m respectively for a few nights during March, 2007 along with the Na airglow photometer. Due to technical problem in the Na lidar, simultaneous observations could not be obtained during the remaining campaign periods.

2.3.4 Multi-Wavelength Airglow Imager

In order to derive the horizontal parameters of atmospheric gravity waves, a multi-wavelength airglow imager was designed and fabricated at Physical Research Laboratory, Ahmedabad. The imager consists of several optical elements, programmable motorized five-position filter wheel and cooled Charge Coupled Device (CCD) (shown in Figures 2.8 and 2.9).

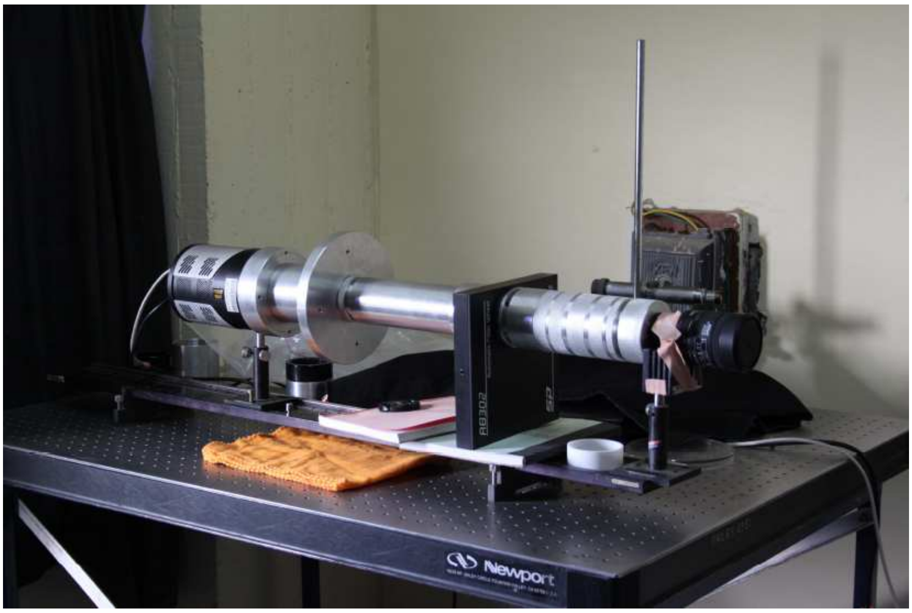

Figure 2.8: The set up of the multi-wavelength imager during laboratory testing phase.

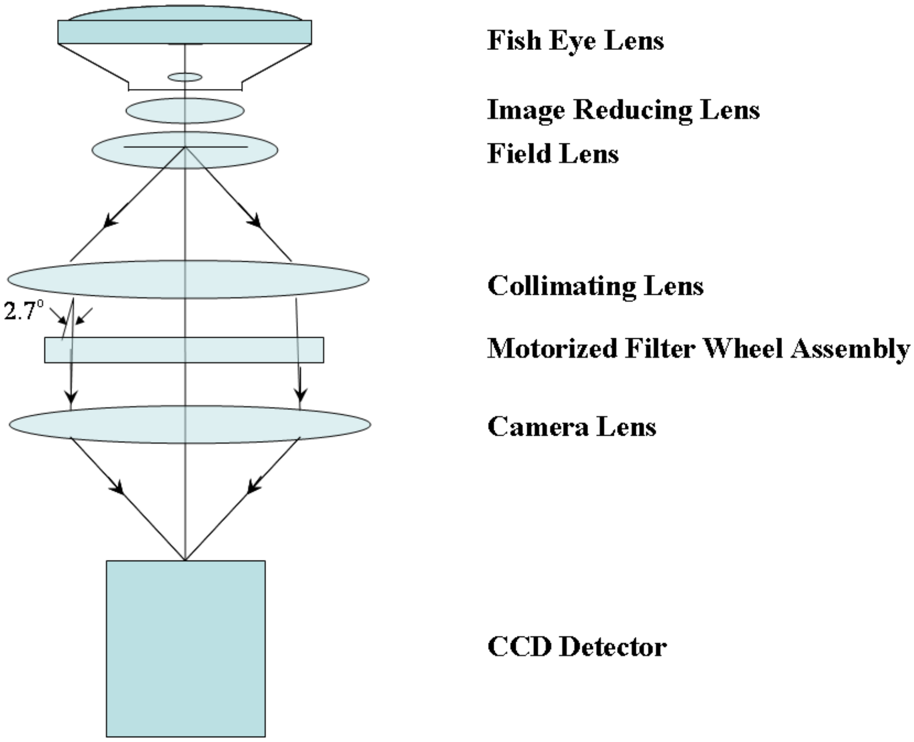

Figure 2.9: The schematic diagram of the multi-wavelength imager.

The optical elements consist of image quality fisheye lens, field lens and camera lens. The fish-eye lens (F/2.8) being an essential part of the lens system decides the field-of-view (FOV) of the system. In general, a fisheye lens has FOV of 180° and reduces the divergence of the optical rays. However, in the present optical system the FOV is brought down to 100° using an external field stop in order to avoid stray light contamination from low elevation. An additional lens (f/1) is attached to the fisheye lens to reduce the image size from 30 mm to 17 mm. This reduced image is now channelled through an achromatic field lens (f/1) and incident on a collimating lens. A field lens positioned at the focal plane channels the beam to get incident on a collimating lens without any loss of flux. A collimating lens further reduces the divergence of the rays before the rays pass through the interference filter. As discussed in *Sekar et al.* [1993], the maximum shift of the pass band ($\Delta\lambda_{max}$) of an interference filter is related to the angle between normal and the farthest ray (θ_{max}) as,

$$\Delta\lambda_{max} = \lambda\theta^2_{max}/2\mu^2 \tag{2.16}$$

Where, μ is the refractive index of the coating material on the interference filter. Therefore, it is necessary to reduce the divergence so that $\Delta\lambda_{max}$ is minimal. The angle of divergence (θ) is decreased if the focal length of the collimating lens is increased. However, the increase in the focal length of a lens reduces the flux of the rays. Thus, there is a competition between the choice of angle of divergence and focal length of collimating lens. In order to make a faster optics, the F number is kept as 4 and hence focal length of collimating lens is limited to 180 mm. As a result, θ_{max} turns to be around 2.7°. Therefore, the bandwidth of the interference filters is chosen to be 1 nm in order to minimize the intensity modulation due to different transmittance at different angles.

The interference filter selects the desired wavelength of emission and the filtered signals are further focussed on the high sensitive CCD pixels using camera lens. The CCD (PIXIS 1024BR-DD) containing 1024×1024 pixels is kept at -80 °C using a in-house multi-stage thermoelectric cooling unit in order to minimize thermal noise. This back-illuminated deep-depleted CCD chip has quantum efficiency that peaks at around 800 nm (>90%). This CCD chip is used to minimize the etaloning effect at near infrared region and suitable to record OH Meinel band [*Meinel,* 1950] emission. This can help in deriving the horizontal parameters of gravity waves with reasonable accuracy.

The whole imaging system is completely automatic and the interfacing between the motorized filter wheel and the CCD camera was carried out in the laboratory. A Graphical User Interface (GUI) is used to synchronize CCD operations with the movement of the filter wheel. The customized program developed in-house is equipped with the capability of handling the movement of the five filter wheel slots at desired time interval. Therefore, suitable exposure times can be set for different airglow emissions depending upon the intensity level.

The imaging system was calibrated against a uniform standard source at SAC, Ahmedabad (Figure 2.10). The response of the each pixel will be useful for flat field correction of the CCD output image.

Figure 2.10: The calibration of imager at SAC, Ahmedabad (Courtesy: SAC, Ahmedabad).

This imager was built during the last phase of the thesis work and the field trials of this imager were carried out recently. Field trials suggest further improvement is needed in optics. Thus the present work does not include any investigation using the observations from this imager.

2.3.5 Satellite Measurements

In order to assess the contribution of mesospheric ozone to the observed Na airglow, the retrieved altitude profiles of ozone obtained from SABER (Sounding of Atmosphere using Broadband Emission Radiometry) instrument on board TIMED (Thermosphere Ionosphere Mesosphere Energetics and Dynamics) satellite are also used in the present investigation. SABER uses the emission at 9.6 μm from ozone to derive its concentration with an uncertainty around 20% [*Martin G. Mlynczak,* private communication, 2008]. In order to use the retrieved ozone concentration by SABER (Data source: http://saber.gats-inc.com; v1.07) in the present investigation, the ozone profiles available for the nearest location are chosen for the post mid-night hours when simultaneous measurements of Na airglow and lidar are available over Gadanki.

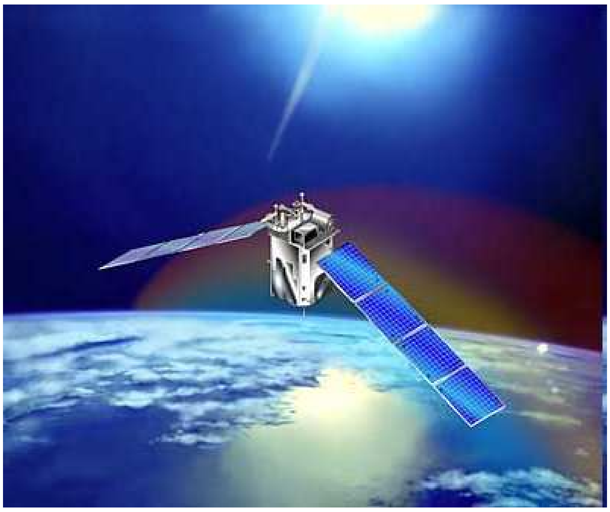

Figure 2.11: TIMED satellite (Courtesy: TIMED website).

SABER also provides pressure and kinetic temperature in the altitude range of 80-105 km. Pressure is retrieved from 15 μm CO_2 terrestrial emissions and temperature is derived using those pressure values. The maximum uncertainty in temperature in the above altitude range is around 10 K [*Mertens et al.,* 2001]. The SABER retrieved temperature is used to derive temperature dependent rate constant for Chapman reaction [*Chapman,* 1939] k_1 (to be discussed in Chapter

3). The uncertainty in pressure is only 3% in the altitude range of 84 to 96 km [*Tom Marshall,* private communication, 2009].

In order to investigate the neutral instability processes in the mesosphere, zonal and meridional wind profiles nearly over Mt Abu and Gadanki were obtained from the TIMED Doppler Interferometer (TIDI) measurements of the wind field (version: R01). Using limb scans of airglow emissions through four orthogonally oriented telescopes, TIDI simultaneously measures the neutral winds with a vertical resolution of 2.5 km and with an accuracy of ~3 m/s [TIDI Home page: http://tidi.engin.umich.edu/html/go?Overview/tidi_overview.html&menu_home – new.html].

The profiles of mesospheric ozone, temperature, zonal and meridional wind obtained from TIMED satellite are used in the present thesis work and discussed in Chapters 3 and 4.

Chapter 3

Investigation on Na Airglow Mechanism

3.1 Background

The source of metallic sodium (Na) in mesosphere is believed to be meteoric origin (discussed in Chapter 1). There are two principal sources of meteoroids in the Earth's atmosphere. The dust trails produced by sublimating comets as they orbit the sun are the origin of periodic meteor showers such as the Perseids and Leonids. Fragments from the asteroid belt and dust particles from long-decayed cometary trails give rise to the continuous input of sporadic meteoroids. The meteoric ablation is the main source of metallic atoms in atmosphere.

It is well established that the neutral Na atoms in mesosphere produce Na airglow emission. Several simultaneous measurements were carried out [e.g. *Clemesha et al.,* 1978; 1979; 1993; *Takahashi et al.,* 1996] in order to understand the Na airglow mechanism. However, there has been considerable debate on the degree of coupling between Na atoms and Na airglow intensity. As introduced in Chapter 1, it is generally believed that the chemical scheme, formulated by *Chapman,* [1939] is responsible for Na airglow.

$$Na + O_3 \xrightarrow{k_1} NaO + O_2 \tag{3.1}$$

$$\begin{aligned} NaO + O &\xrightarrow{\alpha k_2} Na^*(^2P_J) + O_2 \\ &\xrightarrow{(1-\alpha)k_2} Na(^2S) + O_2 \end{aligned} \tag{3.2}$$

$$Na^*(^2P) \longrightarrow Na(^2S) + h\nu(589.0, 589.6\ \ nm) \tag{3.3}$$

where k_1, k_2 are the temperature dependent reaction rate coefficients and α is the branching ratio for the reaction given in equation (3.2).

Chapman mechanism suggested that neutral Na atoms are oxidized by mesospheric ozone and produce NaO. NaO further reacts with mesospheric atomic oxygen (O) to produce the mixer of excited and ground state of Na atoms. The abundance of these excited atoms (Na*) can be determined by the branching ratio (α) of this reaction. Chapman mechanism provided the first systematic explanation for generation of Na airglow emission. This mechanism suggests one-to-one relationship between Na atoms and Na airglow intensity provided ozone concentration remains same.

The Na airglow intensity exhibits considerable variability from one night to another [e.g. *Kirchhoff et al.*, 1979]. The chemical scheme mentioned above suggests that simultaneous measurements of the parameters like number density of neutral Na atoms, mesospheric ozone and temperature are needed to understand the observed night-to-night variation of Na airglow intensity. Several simultaneous measurements of Na airglow intensity and Na concentration were carried out over low latitude stations [e.g. *Clemesha et al.,* 1978; 1979]. However, the simultaneous measurements of most of the parameters involved in the Chapman mechanism were sparse until recently making it difficult to address the variation in Na airglow intensity comprehensively.

Although the importance of the chemical channel proposed in the above scheme in producing Na airglow over mesospheric region is realized over the years, there has been considerable debate regarding the value of the branching ratio α which effectively determines the fraction of the Na atoms that ends up emitting Na airglow. Based on rocket-borne photometry, airglow imager and lidar measurements, the range of α is found to lie between 0.02 to 0.2 [e.g. *Clemesha et al.,* 1995;

Hecht et al., 2000a]. In addition, the recent spectroscopic measurements [*Slanger et al.,* 2005; 2006] showed that intensity ratio of the Na doublet $\left[\frac{I(D_{589.0})}{I(D_{189.6})} = \mathrm{R}_D\right]$ is not invariant and has significant temporal variability. As the reaction (3.1) is rate determining [*Plane,* 2003b], the measurement of mesospheric ozone in the Na airglow study is crucial. With the availability of altitude profiles of mesospheric ozone by satellite borne measurements, it is now possible to examine the impact of ozone variation on the Na airglow intensity. Two case studies are performed to explain the anomalous relationship between Na atom concentration and Na airglow intensity using a set of coordinated measurements of Na atom concentration, Na airglow intensity and satellite borne measurements of mesospheric ozone, pressure and temperature. In this Chapter, the results obtained from these case studies are discussed and the importance of the quenching processes in determining Na airglow emission is brought out.

3.2 Data Set

A single-channel, portable, narrow band (0.3 nm) Na airglow photometer was operated in conjunction with the collocated Na resonance lidar during March, 2007 at Gadanki (13.5° N, 79.2° E). The detailed descriptions of this photometer and Na lidar are discussed in Chapter 2. Na airglow intensities with temporal resolution of 2 minutes were obtained using this photometer. In addition, the profiles of Na atom concentrations are obtained with an altitude resolution of 0.3 km and temporal resolution of 2 minutes based on reliable signal-to-noise ratio in the altitude range of 80-105 km. Due to technical problem, the Na lidar could only be operated for a few nights during March, 2007.

Mesospheric ozone profile, obtained from SABER instrument on board TIMED satellite, are used in the present investigation to assess the contribution of mesospheric ozone to the observed Na airglow. These profiles over a location nearest to Gadanki are chosen during post mid-night hours [at around 20:30 UT or 2:00 IST; Indian Standard Time, IST = Universal Time, UT + 5.5 hrs] when simultaneous measurements of Na airglow and lidar are available.

The profiles of mesospheric pressure and kinetic temperature in the altitude range of 80-105 km are also used in the present work. The details of SABER instrument are available in Chapter 2.

3.3 Data Analyses

In order to evaluate relationship between Na atoms and Na airglow, the volume emission rate (V_{Na}) of the Na airglow is calculated for the two nights under consideration. This is carried out using the following equation.

$$V_{Na} = \alpha k_1 [Na][O_3] \tag{3.4}$$

It is to be noted here that V_{Na}, consists of contributions from both D_2 and D_1 emission lines. The ratio of D_2 and D_1 emission line intensities, R_D $\left(R_D = \frac{I_{D_2}}{I_{D_1}}\right)$ is shown [*Slanger et al.,* 2005] to be variable. As the high resolution photometer is tuned to measure the D_2 line only, the volume emission rate corresponding to D_2 line obtained from V_{Na} needs to be scaled down by a factor $\left(\frac{R_D}{1+R_D}\right)$.

Therefore,

$$V_{NaD_2} = \frac{\alpha R_D}{1 + R_D} k_1 [Na][O_3] \tag{3.5}$$

The maximum uncertainty involved in computing volume emission rate is around 25%. The upper and lower levels of V_{NaD_2} are calculated using the maximum and minimum values of α and R_D for both the case studies. Mesospheric ozone profiles and rate coefficient (k_1) based on SABER measurements as well as average Na concentration profiles obtained from the lidar are also used in these calculations.

One of the case studies involves the comparison of average Na concentrations with the average Na airglow intensities between the two consecutive nights. In order to investigate the variation in the relative intensity levels corresponding to the two nights, the following procedure is adopted. The area under the altitude profiles of the volume emission rate for particular α and R_D are evaluated for both the nights (denoted by 1 and 2). Thus, the ratio of volume emission rates for two nights is equal to the ratio of the observed time-averaged airglow intensities $\Big(\langle I_1 \rangle_t$, $\langle I_2 \rangle_t$ respectively$\Big)$. Mathematically,

$$\frac{\left[\int_{h_1}^{h_2} V_{NaD_2} dh\right]_1}{\left[\int_{h_1}^{h_2} V_{NaD_2} dh\right]_2} = \frac{\langle I_1 \rangle_t}{\langle I_2 \rangle_t} \tag{3.6}$$

As the altitude profiles of Na atoms and ozone are available, the factor $\left(\frac{\alpha R_D}{1+R_D}\right)$ was changed by trial and error method to match the observed variation in the average levels of Na airglow intensity. It is to be noted here that the values of α and R_D are varied within the respective extrema values available in the literature. The implications of this exercise is discussed later.

As the intensity variation on one of the nights (18-19 March, 2007) was entirely different, the relation between the temporal variabilities of Na concentrations at different altitudes and the temporal variation in Na airglow intensity was examined as another case study. Cross-correlation analyses were performed between the temporal variation of Na airglow intensity obtained during 23:12-01:42 IST (this time window was closer to the SABER measurement time of ozone) on 18-19 March, 2007 with the temporal variations of Na concentration at multiple altitudes. Altitude profile of correlation coefficients was constructed subsequently. Correlation coefficients are calculated between 85-100 km as the variances of Na atom concentration are not significant except this altitude region. Correlation coefficients below 95% confidence level are not considered. Further, to compare the spectral modes in Na atom concentration variations at two altitude levels with the spectral modes of Na airglow intensity variation, power spectral analyses were carried out. Spectral peaks below 95% confidence level are not considered.

The altitude integrated volume emission rate of Na airglow corresponding to D_2 line (V_{NaD_2}) is calculated using equation 5 on 19 March, 2007 at 01:30 IST when the TIMED satellite pass was over a location closer to Gadanki. This is, in principle, equivalent to the observed airglow intensity. Therefore, V_{NaD_2} is calculated by suitably varying both α and R_D within their extrema and is compared with the measured airglow intensity.

3.4 Results

Figure 3.1 depicts a compilation of simultaneous observations of Na airglow intensity and Na atom concentration from Gadanki. The left panel depicts the Height-Time-Concentration (HTC) maps of neutral Na atoms constructed from the lidar observations on each night with the color code denoting the concentration level. The right panel shows the temporal variations of Na airglow intensity in Rayleigh (R) for the same intervals.

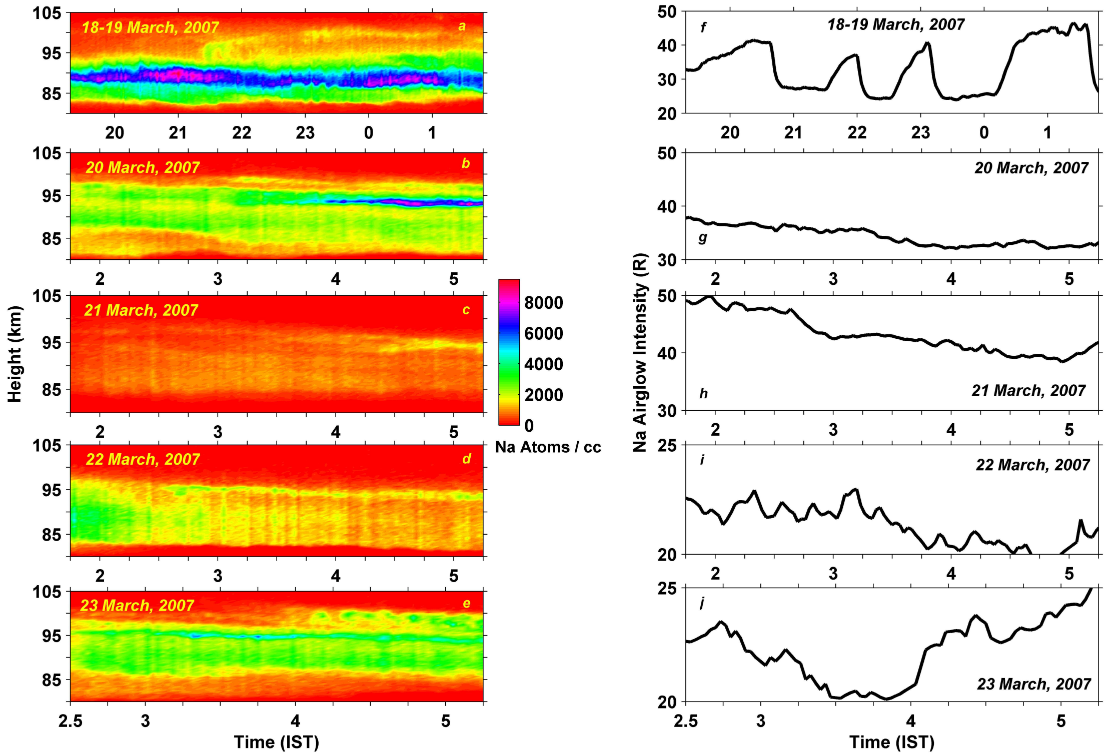

Figure 3.1: The left panel depicts the Height-Time-Concentration maps of Na atoms at various times obtained from Na lidar over Gadanki for five nights during March, 2007. The right panel shows the temporal variation of Na airglow intensity (in Rayleigh) on those respective nights.

The above simultaneous observations suggest that the Na atom concentration and Na airglow intensity have large night-to-night variability. Further, these simultaneous observations suggest that the one-to-one relation between Na atoms and Na airglow intensity is not always maintained. The average Na airglow intensity level on 20 March 2007 is found to be less compared to that on the next night despite average Na concentration being significantly large. In addition, the Na airglow intensity on 22 March, 2007 beyond 03:30 IST decreases. However, the Na atom concentration during that interval is nearly invariant. Similarly, the airglow intensity during 03:30–4:15 IST on 23 March shows a valley region despite Na atom concentration being nearly constant. Therefore, in the subsequent figures, attempts will be made to highlight certain aspects of these variabilities and to investigate the relationship between Na atoms and Na airglow intensity on a night-to-night basis (20 & 21 March 2007) as well as on a given night (18-19 March, 2007).

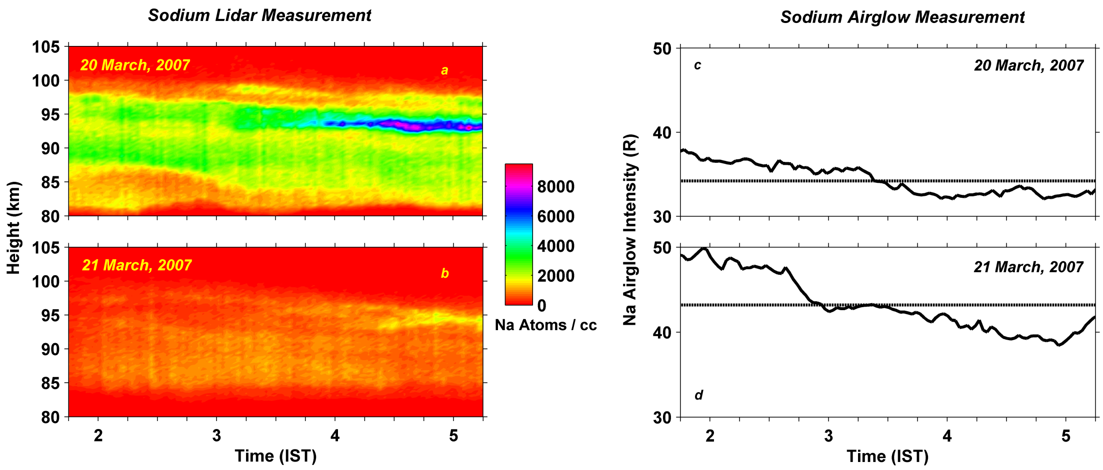

Figure 3.2: (a & b) Height-Time-Concentration (HTC) maps of Na atoms at various times obtained from Na lidar over Gadanki during 20 and 21 March, 2007. The vertical color bar shows the concentration level of Na atoms. (c & d) The temporal variation of Na airglow intensity (in Rayleigh) on those nights. The black horizontal lines in figures correspond to the average intensity level during the observational window.

Figure 3.2 represents the Na lidar and Na airglow measurements during 20 and 21 March, 2007. The black horizontal dashed line in each subplot in the right panel corresponds to the average intensity level during the observational period. The abscissas on both the left and right panels correspond to time in IST. The HTC maps in the left panel reveal that the concentration of neutral Na atoms (shown in Figures 3.2a and 3.2b) on 20 March, 2007 is, in general, large compared to the concentration of Na atom on 21 March, 2007. For example, the peak concentration on 20 March, 2007 is around 9500 atoms/cc at around 04:30 IST, whereas, it is only around 2200 atoms/cc at the same time on the very next night. However, the Na airglow intensity at 04:30 IST is less on 20 March, 2007 (∼33 R) compared to the next night (∼40 R). The Na concentration decreases quite sharply on both the nights below 82 km and beyond 98 km altitudes. It is of interest to note that the enhancement in Na concentration is observed during early morning hours on both the nights around 94 km. This aspect will not be discussed further.

Average values of Na concentration were evaluated for both the nights by time averaging the corresponding lidar profiles during the observational period. Figure 3.3 depicts the altitude profiles of the average Na concentration (black line) for the given duration along with the altitude profiles of the mesospheric ozone concentration (gray line). It is noted that the variations (and not the amplitudes) in the altitude distributions of average ozone and Na concentrations in the altitude range of 85-98 km nearly match within the uncertainty of the measurements. Figure 3.3 reveals that the peak value in the average Na concentration profile on 21 March, 2007 is around a factor of five smaller while, the concentration of mesospheric ozone is only 1.5 times larger compared to the previous night.

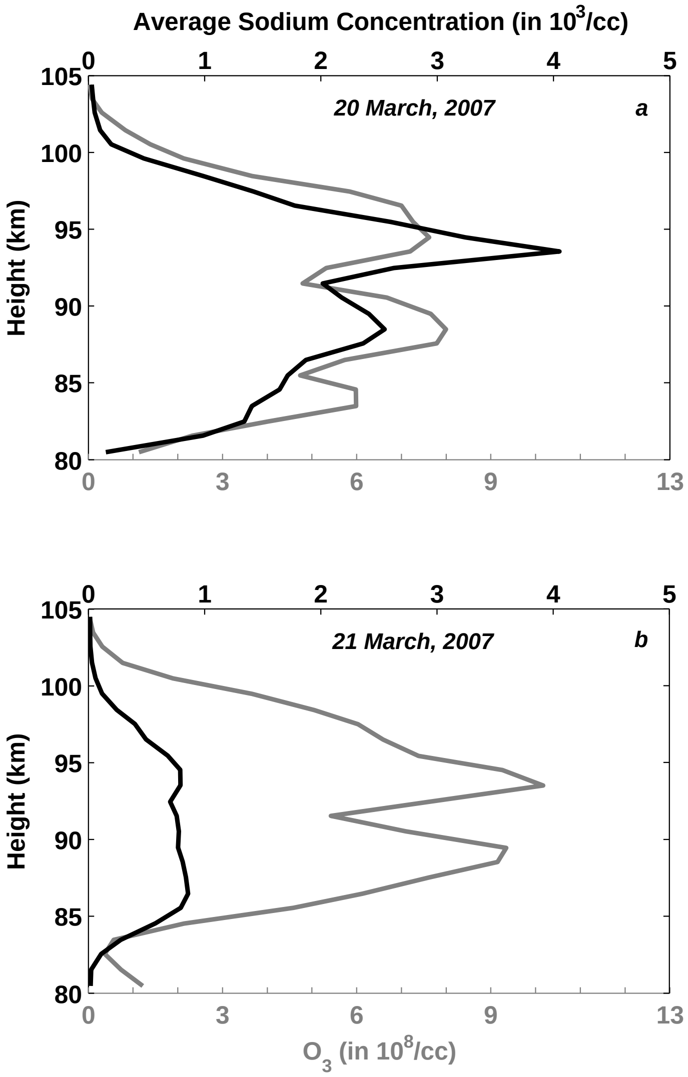

Figure 3.3: (a & b) The altitude profiles of mesospheric ozone concentration (gray curves) retrieved by the SABER instrument onboard TIMED satellite on the two consecutive nights (20 and 21 March, 2007). The altitude variations of the average Na concentration (black curves) on each night are overlaid. The location and time of SABER measurements on 20 and 21 March, 2007 are 12.04°N, 79.09°E; 01:45 IST and 14.08°N, 72.80°E; 02:02 IST respectively.

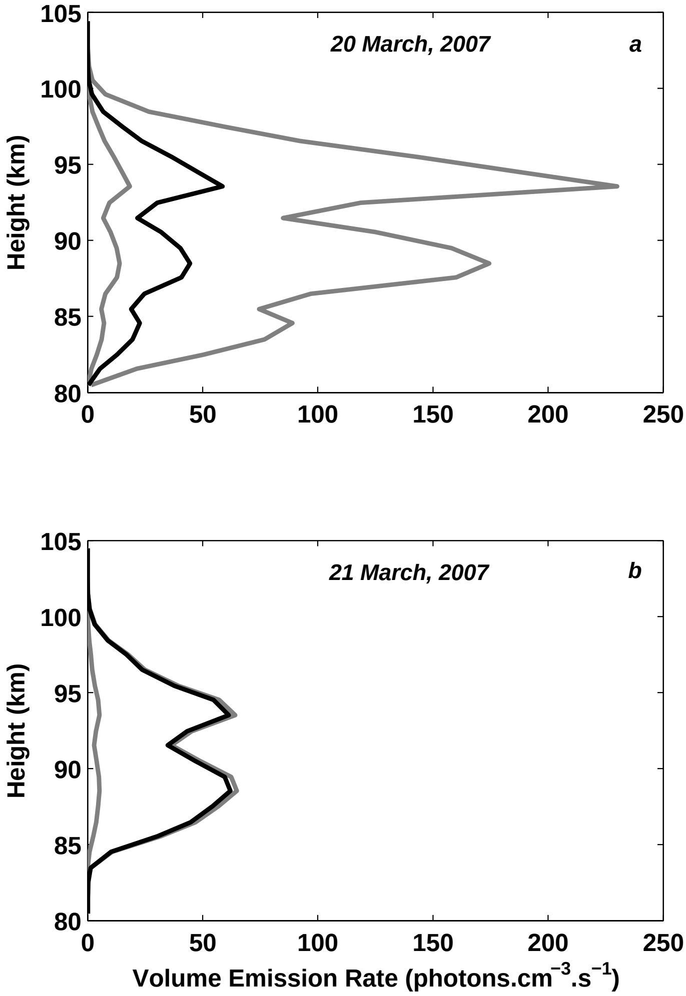

Figure 3.4: (a & b) The altitude profiles of the volume emission rate of the Na airglow on 20 and 21 March, 2007. The upper and lower levels of volume emission rate (gray curves) at D_2 line (V_{NaD_2}) are calculated using extrema values of α and R_D (refer to text). The black curve in each subplot represents the volume emission rates that satisfy the relative variation of average Na airglow intensity level.

The upper and lower limits of altitude profiles of volume emission rate corresponding to the D_2 line (V_{NaD_2}) on each night are shown in Figure 3.4 by gray curves respectively. As discussed earlier, both α and R_D are variable. Therefore, the extrema values of α and R_D are used in the calculation of V_{NaD_2}. The minimum volume emission rate profile is constructed using minimum value of α as 0.02 [*Hecht et al.,* 2000a] and R_D as 1.3 [*Slanger et al.,* 2005, 2006; *Plane et al.,* 2007] using equation 3.5. Similarly, the maximum V_{NaD_2} profile is derived using the uppermost value of α as 0.2 [*Clemesha et al.,* 1995] and R_D as 2.4 [*Slanger et al.,* 2005, 2006; *Plane et al.,* 2007]. It is to be noted that the variation in the average intensity level observed on the two nights cannot be reproduced using the pairs of extrema values. However, the black curves, the volume emission rate profiles on the two nights, calculated by suitably varying both α and R_D, are consistent with the observed relative variation in average Na airglow intensity levels. The values of $\left(\frac{\alpha R_D}{1+R_D}\right)$ satisfying equation 3.6 are 0.036 and 0.135 on 20 and 21 March, 2007 corresponding to the respective black curves in Figure 3.4.

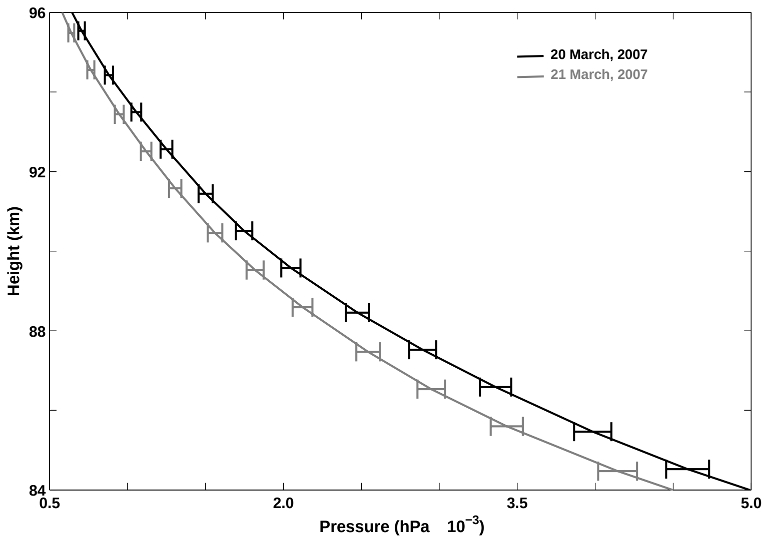

Figure 3.5: The altitude profiles of pressure retrieved by SABER on 20 and 21 March, 2007 in the altitude range of 84-96 km. The uncertainty in retrieving pressure from 15 μm CO_2 emission is represented by the horizontal error bars.

Figure 3.5 depicts altitude profiles of pressure on 20 and 21 March, 2007 in the range of 84-96 km altitude. Interestingly, the pressure on 20 March, 2007 is more compared to its counterpart on 21 March, 2007 throughout the altitude range.

As mentioned earlier, another case study was performed in order to investigate the relationship between the Na atoms and Na airglow intensity on a given night (18-19 March, 2007). The results pertaining to this study are described in the following figures. The measurements obtained from Na lidar, Na airglow photometer and satellite borne instrument (SABER) on this night are plotted in Figure 3.6. Figure 3.6a depicts the HTC map of neutral Na atoms. The vertical color bar denotes the concentration levels. It is noted that Na atom distribution is relatively higher in a narrow, localized altitude region between 85-95 km throughout the period of observation. Figure 3.6b shows the Na airglow intensity variation (black curve) in Rayleigh (R) overlaid on the average airglow intensity variation constructed from 10 nights of observations (excluding 18-19 March) during the month of March (gray curve). This figure highlights the significant difference in the Na airglow intensity variation on 18-19 March from the average Na airglow intensity variation during the interval for that month. Figure 3.6c represents altitude profiles of mesospheric ozone concentration (gray curve) along with Na concentration (black curve) obtained at 01:30 IST on 19 March, 2007. It is of interest to note that the altitude profile of mesospheric ozone has a valley region at the peak altitude of Na concentration located at $\sim$88.5 km. Further, there is a third peak of both ozone and Na concentration at around 94 km closer to the altitude (93.6 km) where the correlation coefficient is maximum (to be discussed later in Figure 3.8a).

Figures 3.6d and 3.6e depict the results of the power spectral analyses of the observed Na concentration at two specific altitudes (93.6 km and 88.5 km) and altitude-integrated Na airglow intensity variation on 18-19 March respectively. The rationale behind the choice of 93.6 km and 88.5 km altitudes will be clear subsequently from Figures 3.7a and 3.7b. Figure 3.6d reveals the dominance of 128 min, 85 min, 64 min periodicities at 93.6 km altitude with decreasing power and dominance of 103 min, 57 min periodic components at 88.5 km altitude with decreasing power. Figure 3.6e, on the other hand, reveals the dominance of periodicities of 123 min, 77 min, 56 min with decreasing power. Comparison of the spectral peaks in Figures 3.6d and 3.6e also suggests that the correlation between Na concentration and Na airglow intensity is better at 93.6 km altitude. It must be noted here that it is not possible to find out the correlation between Na concentration and Na airglow unless other parameters like ozone concentration remains invariant with time. Based on several years (2003-2007) of SABER data, the average temporal variation of ozone over Gadanki for the altitude region of 80-105 km for the month of March is analyzed. Barring the daytime passes of TIMED satellite, the data set is available only between 23:00 to 2:00 IST during nighttime nearly over Gadanki.

The analysis revealed that the temporal variation of ozone concentration during 23:0 to 2:00 IST is well within uncertainty of measurement at both 88.5 km and 93.6 km (Figure 3.6f). Therefore, this time zone is chosen for the correlation analysis depicted subsequently in Figures 3.6 and 3.7a.

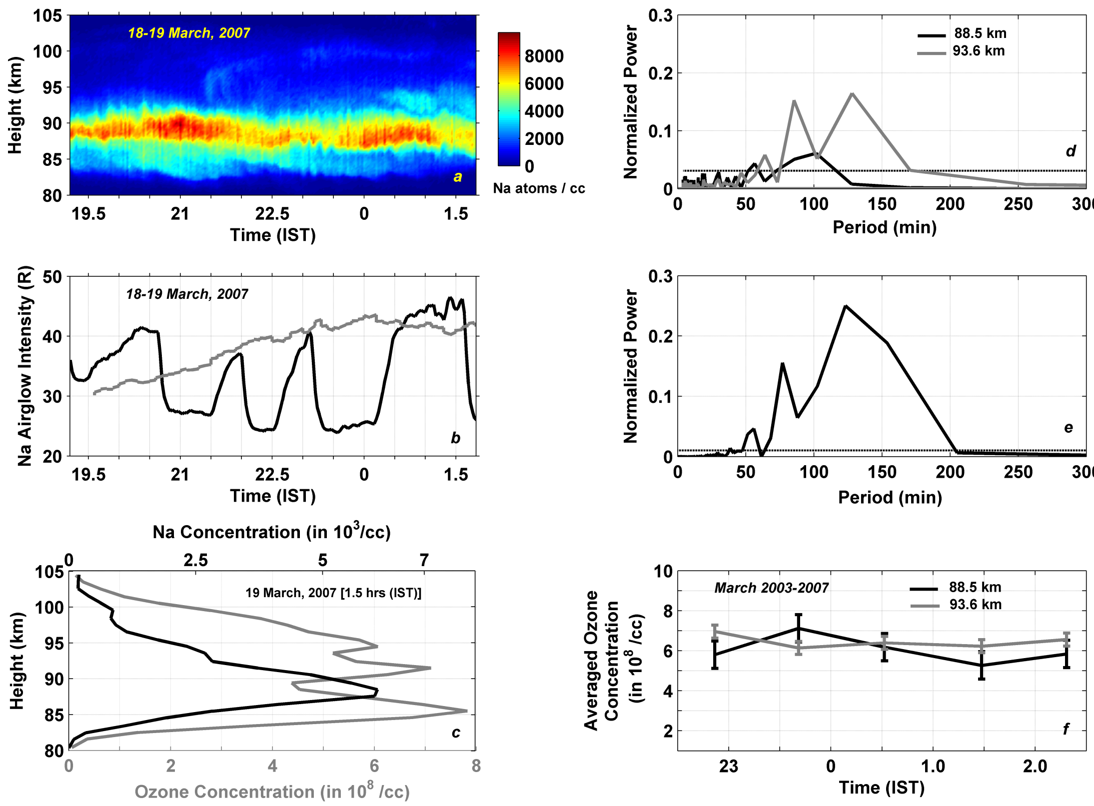

Figure 3.6: (a) Height-Time-Concentration (*HTC*) maps of Na atoms obtained from Na lidar over Gadanki during nighttime on 18-19 March, 2007. (b) The temporal variation of Na airglow intensity (in Rayleigh) corresponding to D_2 line on 18-19 March, 2007 (black curve) along with the average variation of Na airglow during March (gray curve). (c) The gray curve corresponds to SABER retrieved mesospheric ozone profile measured over the nearest location of Gadanki at 01:30 IST on 19 March, 2007 overlaid on the Na atom concentration profile at that time (black curve). (d & e) The power spectral components of the observed Na concentration at two specific altitudes (93.6 km and 88.5 km) and altitude-integrated Na airglow intensity variation on 18-19 March respectively. The dotted horizontal lines in the both figures represent the 95% confidence level above which the spectral components are considered. (f) Monthly (for the month of March) averaged temporal variation of ozone during 23:00–02:00 IST over Gadanki at 88.5 km and 93.6 km for several years (2003-2007). These variations are well within uncertainty of measurement.

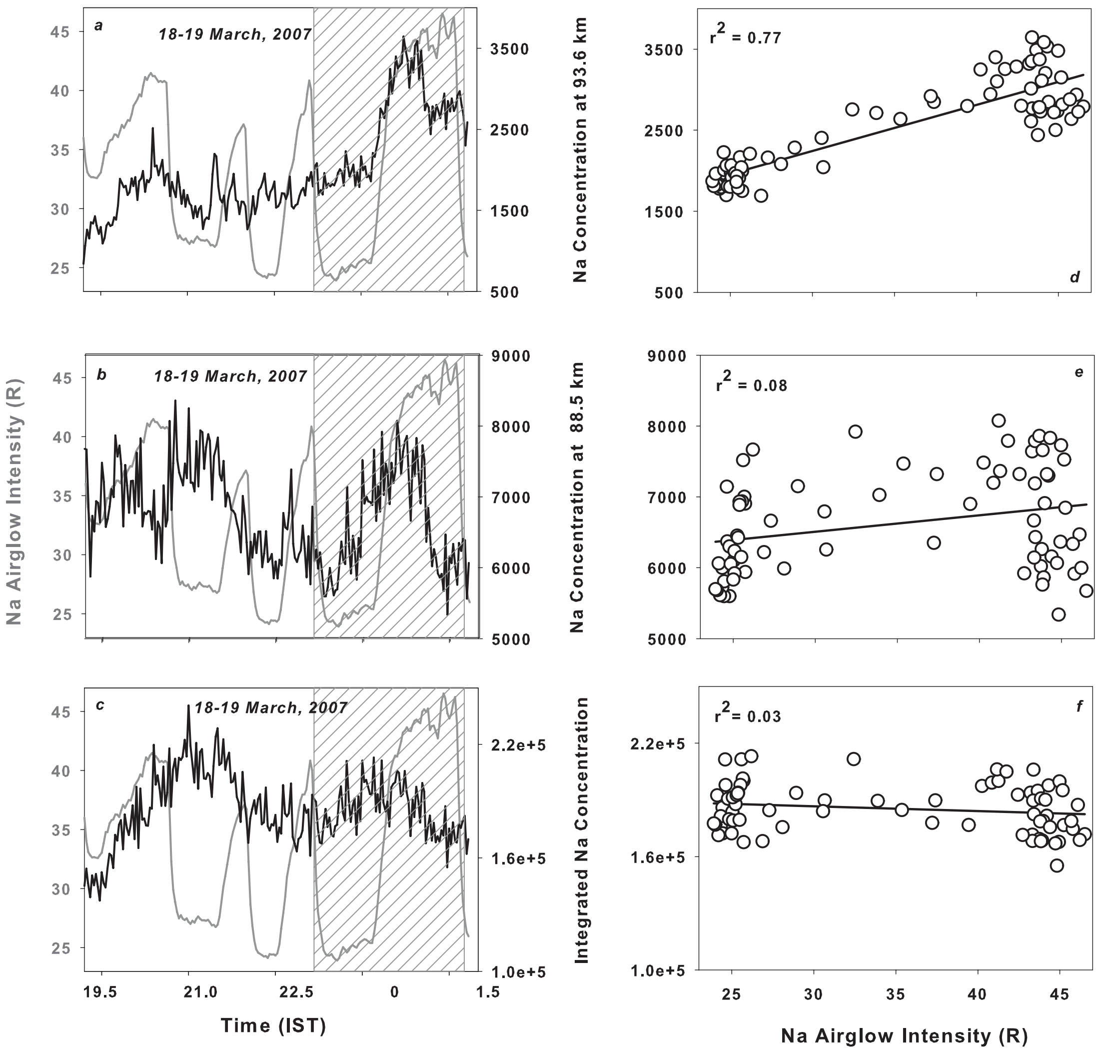

Figure 3.7: (a-c) The gray curves represent the Na airglow intensity variation whereas, the black curves correspond to the Na atom concentration (in atoms/cm^3) variation at 93.6 km, 88.5 km and altitude integrated concentration (in atoms/cm^2) respectively. (d-f) Coefficient of determination (r^2) obtained from the variations in Na airglow intensity and Na atom concentration at respective altitude region during the time window shown in the shaded region of left panel of figure.

Figures 3.7a and 3.7b depict the comparisons of temporal variations in Na airglow intensity (gray curve) and the Na atom concentration (black curve) at two representative altitudes (93.6 and 88.5 km respectively) respectively whereas, Figure 3.7c brings out a comparison between the temporal variation of altitude-integrated Na atoms with the Na airglow intensity. Figures 3.7a, 3.7b and 3.7c (left panel of Figure 3.7) reveal that Na airglow intensity variations during 23:12-01:42 IST (shaded region) match fairly well with the temporal variation in Na atoms only at 93.6 km (Figure 3.7a) and do not corroborate with the temporal variations in Na atoms at the peak altitude of Na concentrations. The left panel of Figure 3.7 is also supplemented by the corresponding cross-correlation analyses in the right panel. It is found that the value of coefficient of determination (r^2) is significant at 93.6 km (Figure 3.7d) and negligible corresponding to the other two cases (Figures 3.7e and 3.7f respectively). It can be additionally noted here that if a finite time lag ($\sim$10 minutes in Figure 3.7b) is given to the temporal variation of Na concentration at 88.5 km altitude, the correlation coefficient may improve. However, the time constant for the reaction of Na airglow is only a few seconds [*Plane et al.*, 1993]. Therefore, correlation analysis with such a large time lag is not considered.

It is also to be noted here that even if one chooses the full observational period (19:30–01:42 IST), the correlation coefficient (shown in Figure 3.8a) reduces from 0.86 to 0.55 at 93.6 km altitude and 0.3 to 0.1 at 88.5 km altitude possibly due to the random variation in the time lags required at different time intervals. Thus the choice of specific time window (23:12-01:42 IST) does not alter the conclusion of the present work.

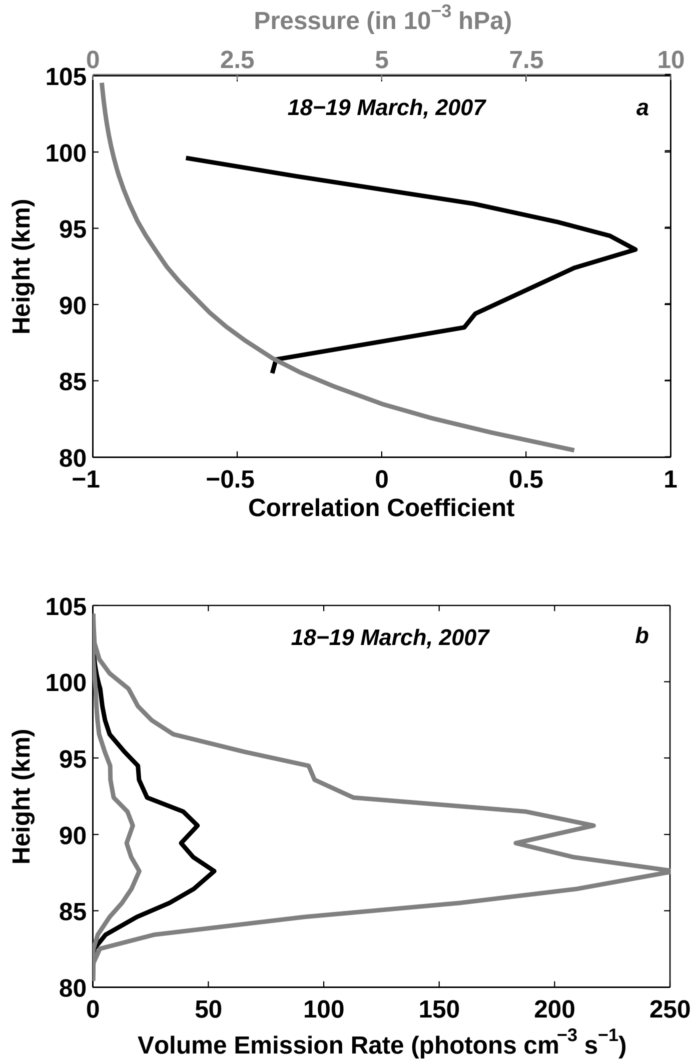

Figure 3.8: (a) The altitude profiles of correlation coefficient (black curve) along with the ambient pressure obtained from SABER (gray curve). (b) The gray curves correspond to the uppermost and lowermost level of volume emission rate profile of Na airglow corresponding to D_2 (V_{NaD_2}) line whereas, the black curve represents the V_{NaD_2} by suitably varying $\left(\frac{\alpha R_D}{1+R_D}\right)$ within their respective maxima in order to match the observed Na airglow intensity level at SABER measurement time.

Figure 3.8a depicts the altitude profiles of the correlation coefficients and pressure between 80 to 105 km. The correlation profile reveals that the correlation peak lies at ~93.6 km. The ambient pressure, plotted in Figure 3.8a, reduces by a factor of ~2.5 as altitude changes from 88.5 to 93.6 km. It is interesting to note that correlation peak altitude differs from the peak altitude (88.5 km) of Na atom concentration profile (Figure 3.6c) by around one scale height. The two gray curves in Figure 3.8b depict the altitude profiles of volume emission rate (V_{NaD_2}) for the maximum and minimum values of the factor $\left(\frac{\alpha R_D}{1+R_D}\right)$. However, in both the cases, the area under the V_{NaD_2} curve does not match with the observed airglow intensity. Therefore, using trial and error method, the factor $\left(\frac{\alpha R_D}{1+R_D}\right)$ is varied suitably in between the extrema so as to match the altitude-integrated value of V_{NaD_2} with the observed airglow intensity level measured using ground based Na airglow photometer. It may be noted that the values for $\left(\frac{\alpha R_D}{1+R_D}\right)$ are chosen to be altitude independent for all the three curves in Figure 3.8b. Nevertheless, the peak altitude in the volume emission rate differs significantly from the peak altitude in the correlation curve (Figure 3.8a).

3.5 Discussion

3.5.1 The Effects of Collisions on Na Airglow

Na airglow intensity observations reported in the present investigation exhibit significant variation on the two nights. Interestingly, the average intensities are larger on 21 March 2007 despite the fact that the average Na atom concentration is less by at least a factor of three (Figures 3.3a and 3.3b) on this night in comparison with 20 March 2007. The fact that Na atom concentrations and the Na airglow intensity are not proportional on those two nights during the observational period clearly indicates that there exist other parameters in addition to Na atoms that decide Na airglow intensity variations. The Chapman mechanism suggests that Na airlgow emission intensity depends not only on the concentration of Na atoms but also on the ambient mesospheric ozone concentration. As reaction (3.1) determines the rate of the Chapman reaction, it is expected that the variability in ozone concentrations will significantly contribute to the overall variation of Na airglow emission intensity. It is to be noted here that the SABER retrieved ozone profiles can represent the ozone concentration at the Na airglow emission altitude fairly well despite minor differences in the observation periods. This is owing to the fact that chemical lifetime of ozone at mesospheric altitude beyond 80 km during nighttime is more than 12 hours [*Brasseur and Solomon,* 1986]. Post-midnight enhancement [*Zommerfelds et al.,* 1989] of mesospheric ozone is possible due to vertical downward transport of atomic oxygen. However, as suggested by *Connor et al.* [1994] and *Huang et al.* [2008], this mechanism is operative at around 70 km in the equatorial region. Therefore, the assumption of temporal invariance of profiles at an altitude region of 80-105 km after midnight is believed to be realistic for the present investigation. Thus, the snapshot measurement of mesospheric ozone during post-midnight hours can represent average ozone concentration. Apparently, a relatively enhanced peak ozone concentration may seem to cause the enhanced Na airglow intensity despite lesser Na atom concentration on 21 March 2007. However, even after incorporating measured ozone concentrations in the volume emission rate calculation and keeping α and R_D constant (not shown), the variations in the Na airglow intensity on the two nights could not be reproduced.

The observed Na airglow intensity variations during observational period may also get altered if mesospheric temperatures vary substantially in time and altitude. This is because rate coefficient (k_1) pertaining to reaction (3.1) is dependent on ambient temperature [*Plane,* 2004]. Based on a morphological investigation, *Kishore Kumar et al.* [2008] brought out that the maximum variation in the nocturnal temperature in the altitude range of 80-105 km over Gadanki during the month of March is $\sim$20K. Following *Plane,* [2004], the temperature dependent rate constant k_1, for a temperature change of 20 K, was found to be insignificant to alter the volume emission rate significantly. The nocturnal mesospheric temperature during 20 and 21 March, 2007 was also found to vary from a minimum of 160 K to a maximum of 210 K. Even after using k_1, the variability of Na airglow brightness levels on those two nights could not be reproduced. In other words, variability of Na airglow brightness levels could not also be obtained by varying k_1 from 5.33×10^{-10} to 6.33×10^{-10} cm^3s^{-1} (considering the above mentioned temperature extrema) keeping both α and R_D constant. Therefore, it is implied that the only way to reproduce the observed relative variation in the Na airglow intensity levels on the two nights is through the possible variation of both α and R_D. The range of the values of volume emission rate in Figure 3.4 indicate that the variability of Na airglow intensity cannot be explained by keeping the same α and R_D on both nights. Therefore, both α and R_D are taken to be significantly different on the two nights.

Slanger et al. [2005] suggested that night-to-night variations of α and R_D are possible. The original Chapman mechanism is modified by *Slanger et al.*, [2005] to accommodate this aspect. As discussed in Chapter 1, the proposed chemical scheme is as follows.

$$Na + O_3 \longrightarrow NaO^*(A^2\Sigma^+) + O_2 \tag{3.7}$$

$$NaO^*(A^2\Sigma^+) + O(^3P) \longrightarrow Na^*(^2P_J) + O_2 \tag{3.8}$$

$$NaO^*(A^2\Sigma^+) + M \longrightarrow NaO(X^2\Pi) + M \tag{3.9}$$

$$NaO(X^2\Pi) + O(^3P) \longrightarrow Na^*(^2P_J) + O_2 \tag{3.10}$$

In this scheme, the variations in α and R_D are suggested to depend on whether $NaO^*(A^2\Sigma^+)$ or $NaO(X^2\Pi)$ is predominantly available in the emission altitude region. It is shown that NaO is mostly produced in excited state $NaO^*(A^2\Sigma^+)$ rather than in ground state $NaO(X^2\Pi)$ [*Shi et al.,* 1993; *Wright et al.,* 1993]. Based on theoretical analysis, *Herschbach et al.* [1992] showed that α would be on the higher side (0.67), if $NaO^*(A^2\Sigma^+)$ entirely reacts with O. This was also supported by *Grifin et al.* [2001] wherein it was shown that the value of α will be higher if the abundance of $NaO^*(A^2\Sigma^+)$ is large. On the other hand, the value of α was suggested [*Herschbach et al.*, 1992; *Joo et al.*, 1999] to be less if $NaO^*(A^2\Sigma^+)$ gets quenched and converted to $NaO(X^2\Pi)$ before its reaction with O. The quenching of $NaO^*(A^2\Sigma^+)$ to $NaO(X^2\Pi)$ also affects R_D [*Slanger et al.*, 2005, 2006]. The reactions (3.8) and (3.10) are likely to produce $Na(^2P_{1/2})$ and $Na(^2P_{3/2})$ with different D-line ratios. Hence, R_D will have different values depending on the quenching of $NaO^*(A^2\Sigma^+)$ with ambient gas. *Slanger et al.*, [2005] postulated that R_D will be on the higher side ($\sim$2.4) if $NaO^*(A^2\Sigma^+)$ reacts with O. However, it may be as low as 1.3 if $NaO(X^2\Pi)$ comes into the picture. Therefore, both α and R_D are dependent on ambient background condition.

The present investigation indicates the need of variable α and R_D on the two nights under consideration to explain the observed variability in Na airglow intensity level. As discussed above, this is due to the variability of the quenching of $NaO^*(A^2\Sigma^+)$. Figure 3.5 reveals that the pressure level on 20 March, 2007 is higher compared to that on the next night throughout the emitting altitude range. High pressure implies enhanced quenching of $NaO^*(A^2\Sigma^+)$ with ambient atmospheric neutral species on 20 March, 2007 that might lead to less sodium airglow intensity on this night. It is difficult to quantify the required enhanced pressure level on 20 March, 2007 to match observed airglow intensity as there is no established relationship available in the literature. It is interesting to note that the factor $\left(\frac{\alpha R_D}{1+R_D}\right)$ is also dependent on the quenching process. It is well established [*Herschbach et al.*, 1992; *Joo et al.*, 1999] that the dependence of branching ratio α is less when quenching of $NaO^*(A^2\Sigma^+)$ is more. However, the dependence of R_D on the quenching process is not known. *Slanger et al.*, [2005] postulated that R_D will be on the higher side ($\sim$2.4) if $NaO^*(A^2\Sigma^+)$ reacts with O. However, it may be as low as 1.3 if $NaO(X^2\Pi)$ comes into the picture. The factor $\left(\frac{\alpha R_D}{1+R_D}\right)$ being less on 20 March, 2007 (described in the results section) is possible only when both α and R_D are on the lower side. Thus, the present measurements along with with volume emission rate calculations augment the previous postulation of *Slanger et al.*, [2005] and indicate that both α and R_D have possible roles to play in deciding the observed Na airglow intensity level on the two nights which provide an evidence [*Sarkhel et al.,* 2009; *Sekar et al.,* 2010] to collisional quenching process that was suggested by *Slanger et al.* [2005]. Although collisional quenching is expected to vary with altitude, earlier investigations did not explicitly consider this aspect to explain the observed variations in Na airglow. The simultaneous observation of Na airglow and Na lidar on 18-19 March, 2007 over Gadanki substantiates this aspect of collisional quenching effects on Na airglow.

3.5.2 Possible Altitude Variation of Collisional Quenching on Na Airglow

Na airglow intensity variation on 18-19 March, 2007 during 19:30–01:42 IST is significantly different (Figure 3.8b) from the average nocturnal variation of March, 2007. It is further noticed that variations in Na airglow intensity nearly follow the variations in the Na atom concentration at $\sim$93.6 km at around midnight. At this time, Na concentration increases approximately from 1800 atoms/cc to 3500 atoms/cc that corresponds to ∼94% increase whereas Na airglow intensity changes approximately from 25 R to 45 R that amounts to ∼80% increase. Since the volume emission rate of the Na airglow is proportional to the Na concentration, the above-mentioned observation indicates that the observed Na airglow intensity variation is primarily due to variation in Na concentration at 93.6 km at around midnight when variation in ozone concentration at that altitude is nominal. Interestingly, as revealed by Figure 3.8a, this correspondence between Na atoms and airglow is observed at an altitude (∼93.6 km) where Na atom concentration is relatively less in comparison with the maximum Na atom concentration observed at 88.5 km. Therefore, the peak altitude of correlation lies at ∼93.6 km which is almost one scale height above than the peak altitude of Na atom concentration at that time. In addition, the integrated Na concentration does not corroborate with the Na airglow intensity variation during 23:12-01:42 IST. These considerations indicate that more Na concentration does not necessarily warrant more Na airglow and more importantly, there is possibly a critical dependence of Na airglow on the altitude–specific mesospheric conditions that include distribution of mesospheric ozone, temperature-dependent rate constant (k_1), branching ratio (α) and D_2/D_1 intensity ratio (R_D).

The dependence of Na airglow emission on mesospheric ozone is evident from the Chapman mechanism. As mentioned earlier, it is expected that the variability in ozone concentration will significantly contribute to the variability of Na airglow emission intensity. As already stated in the results section, temporal variation of ozone concentration during 23:00 to 02:00 IST is not significant. This is also supported by the recent model calculation by *Schmidt et al.* [2006]. Therefore, it is unlikely that the Na airglow variation during 23:12-01:42 IST is caused by the temporal variations in the mesospheric ozone concentration.

The observed Na airglow intensity variations during 23:12-01:42 IST may also get altered if mesospheric temperatures vary substantially in time and altitude. As already shown earlier that the maximum variation in nocturnal mesospheric temperature during March over Gadanki is not sufficient to change k_1 and consequently, the volume emission rate significantly. Therefore, it can be safely taken that variation in mesospheric temperature is not responsible for the variation in

Na airglow intensity during 23:12-01:42 IST.

Figures 3.6b and 3.6e suggest that the airglow layer is modulated by the passage of gravity waves. In this context it is important to note here that the passage of atmospheric gravity waves can introduce dynamical and subsequently, chemical changes as it passes through atmospheric medium especially mesosphere [e.g. *Walterscheid et al.,* 1987]. Dynamical changes cause redistribution of atmospheric constituents and as a consequence, the abundance of atmospheric species participating in chemical reactions involving airglow emission can change with time. Therefore, changes in the chemistry of Na airglow emission process capture the dynamical changes introduced by the passage of gravity waves. As the volume emission rate profiles are calculated based on measured variations of Na atom, mesospheric ozone and reaction rate constant k_1 using the SABER-measured temperature profile, the effect of gravity waves is believed to be already included implicitly in the present investigation.

The temporal or altitudinal variations in R_D and/or α may also be responsible for the observed Na airglow intensity variation during 23:12-01:42 IST. The Na airglow intensity changes approximately from 25 R to 45 R at around local midnight. This amounts to ~80% increase. The observed Na airglow intensity variation from ~25 R to ~45 R at ~24:06 IST could not be reproduced by considering the extreme variations in R_D and the variation in R_D with pressure is postulated to be a step like function [*Slanger et al.,* 2005]. On the other hand, α can be variable depending upon ambient pressure [Slanger et al., 2005] and the value of α can range from 0.02 to 0.2 [*Clemesha et al.,* 1995; *Hecht et al.,* 2000a]. As drastic changes in pressure in short time scale is generally not expected at that altitude, it is assumed that α is temporally nearly invariant in this case. Further, it can also be noted from Figure 3.8b that the peak altitudes of V_{NaD_2} do not change for three different altitude-independent values of $\left(\frac{\alpha R_D}{1+R_D}\right)$. In other words, the peak altitude of V_{NaD_2} profiles cannot get closer to the peak altitude revealed by the correlation analysis (Figure 3.8a) without the altitude variation of $\left(\frac{\alpha R_D}{1+R_D}\right)$. Therefore, any variation other than the altitude variation in $\left(\frac{\alpha R_D}{1+R_D}\right)$ does not satisfactorily explain the observations reported here. It is to be noted that the individual value of

α and R_D cannot be obtained particularly in the absence of Na D_1 line intensity.

The above salient points suggest that the factor $\left(\frac{\alpha R_D}{1+R_D}\right)$ may be altitude-dependent. Following *Slanger et al.* [2005], it is discussed in *Sarkhel et al.* [2009] that the factor $\left(\frac{\alpha R_D}{1+R_D}\right)$ is more when quenching of $NaO^*(A^2\Sigma^+)$ is less with the ambient gas. Based on simultaneous Na concentration and Na airglow observations on two nights in conjunction with SABER data, *Sarkhel et al.* [2009] showed that altitude-independent values of $\left(\frac{\alpha R_D}{1+R_D}\right)$ needed to be variable (0.036 and 0.135 on the two nights respectively) to explain anomalous Na airglow intensity variations. As the values of both α and R_D depend on the ambient pressure, possible variation in the values of altitude-dependent $\left(\frac{\alpha R_D}{1+R_D}\right)$ was attributed to ambient collisions. In the present case, however, the altitude-independent value of $\left(\frac{\alpha R_D}{1+R_D}\right)$ turns out to be ~0.0295 when the altitude independent value of volume emission rate match with the observed airglow intensity level. However, this does not match with the correlation curve as the peak in the correlation curve (93.6 km) lies about a scale height above than the peak altitude of Na atom concentration (88.5 km) (Figures 3.6c and 3.8a). Atmospheric pressure at 93.6 km, as shown in Figure 3.8a, is ~2.5 times less in comparison with that at 88.5 km. This will result in more collisional quenching of $NaO^*(A^2\Sigma^+)$ at 88.5 km than at 93.6 km. Therefore, enhanced Na airglow emission is expected at ~93-94 km, where the factor $\left(\frac{\alpha R_D}{1+R_D}\right)$ has larger value. Earlier in-situ measurements [*Clemesha et al.,* 1993, 1995; *Hecht et al.,* 2000a] of volume emission rate profiles were found to maximize at ~95 km. Thus, the relatively larger value of the factor $\left(\frac{\alpha R_D}{1+R_D}\right)$ at correlation peak altitude rather than the altitude of maximum Na atom concentration may be responsible for the enhancement in volume emission rate at the altitude other than peak altitude of Na atom concentration in the present case. The investigation implicitly suggests that the factor $\left(\frac{\alpha R_D}{1+R_D}\right)$ varies with altitude. Therefore, the altitude variation of the collisional quenching needs to be considered, on this occasion, to account for the observed Na airglow intensity variation [*Sarkhel et al.,* 2010; *Sekar et al.,* 2010].

Thus, the collision with the ambient molecules plays a significant role in deciding Na airglow intensity. Based on a few nights of simultaneous measurements of neutral Na atom concentration and Na airglow intensity over Gadanki, it was observed that one-to-one relationship between Na atom and Na airglow intensity do not need to be maintained at all the time. The present investigations indicate that the effect of the collisional parameters like α and R_D are significant in Na airglow reaction. Further systematic observations are needed in order to establish the effects of collision.

Chapter 4

Mesospheric Gravity Waves over Indian Low Latitude Stations

4.1 Background

The terrestrial mesopause region (~85-95 km) acts as an interface zone between the lower atmosphere and thermosphere. In recent times, significant evidences have been obtained that indicate strong influence of lower atmospheric processes like Atmospheric Gravity Waves (AGWs) [e.g. *Meriwether,* 1996; *Walterscheid and Hickey,* 2005], tides [e.g. *Immel et al.,* 2006] etc in the dynamics of Thermosphere-Ionosphere System (TIS). Therefore, Mesosphere-Lower Thermosphere (MLT) coupling is one of the important issues that needs to be addressed to understand the coupling of lower and upper atmosphere comprehensively.

4.1.1 Atmospheric Gravity Waves

As stated, AGWs [*Hines,* 1960] act as a dynamical coupling agent between mesosphere and Thermosphere-Ionosphere System (TIS). The perturbations in atmosphere, generated thermal forcing, lightning, wind flow over a mountain, etc propagate upward and Earth's gravity acts as a restoring force in the propagation of these waves. These are commonly known as AGWs. The periods of these waves range from as low as 5 min to 3 hours. The horizontal wavelengths of the AGWs can be ~50-500 km whereas, the vertical wavelengths can range from 5 to 10 km in mesosphere. AGWs, generated at lower altitude regions, generally propagate upward as atmospheric density decreases with altitude. In order to conserve energy, its amplitude grows exponentially with the altitude. These waves eventually break [*Hecht et al.,* 1997; *Fritts et al.,* 1997] and dump their energy into mesosphere. AGWs play very crucial role in the mesospheric heat budget [*Killeen and Johnson,* 1995] as they transport energy and momentum to mesosphere, generate turbulence, and interact with the background mean flow [*Fritts,* 1984; *Fritts and Alexander,* 2003].

4.1.2 Characterization of AGWs

In order to understand upper atmospheric energetics and dynamics, characterization of AGWs becomes extremely important. The parameters of AGWs can be derived using ground based remote-sensing techniques like lidar, VHF, MF and meteor radars. These are very useful techniques in deriving atmospheric parameters such as temperature and neutral wind. Some of the important results obtained by these techniques over Indian longitude sectors are already discussed in Chapter 1. Observations using lidar and radar can be carried out with extremely good temporal and height resolution and the backscattered signals can be used to derive the parameters of AGWs.

As discussed in the Chapter 1, the AGWs can be characterized using Na resonance lidar. The downward phase propagation of AGWs can be clearly observed in neutral Na atom layer [e.g. *Rowlett et al.,* 1978; *Taylor et al.,* 1995a; *Bhavani Kumar et al.,* 2007a]. In the present thesis work, one such event consisting of the passage of AGWs through neutral Na atom layer is identified from the observations made by the author. Figure 4.1 depicts the temporal development of the altitude profiles of Na concentration on 18-19 March, 2007 over Gadanki. Around 200 profiles of Na atom concentration with 2 minutes temporal resolution are stacked together in Figure 4.1. Wave-like signature can clearly be seen in the stacked plot. The peaks in the Na concentration at a given altitude are descending down with time indicating clearly the downward phase propagation (inclined arrows) characteristic of gravity waves. The wave activities are observed throughout the altitude range of 82-95 km with largest downward phase propagation within 86-89 km during ∼00:00-01:40 IST. The downward phase progressions at different altitudes during the same time (22:30-00:00 IST) indicate the presence of multiple modes of gravity waves. The downward phase velocity on that night is observed to be less than 1 m/s. The uncertainty of measurements of the phase velocity is less than 0.1 m/s.

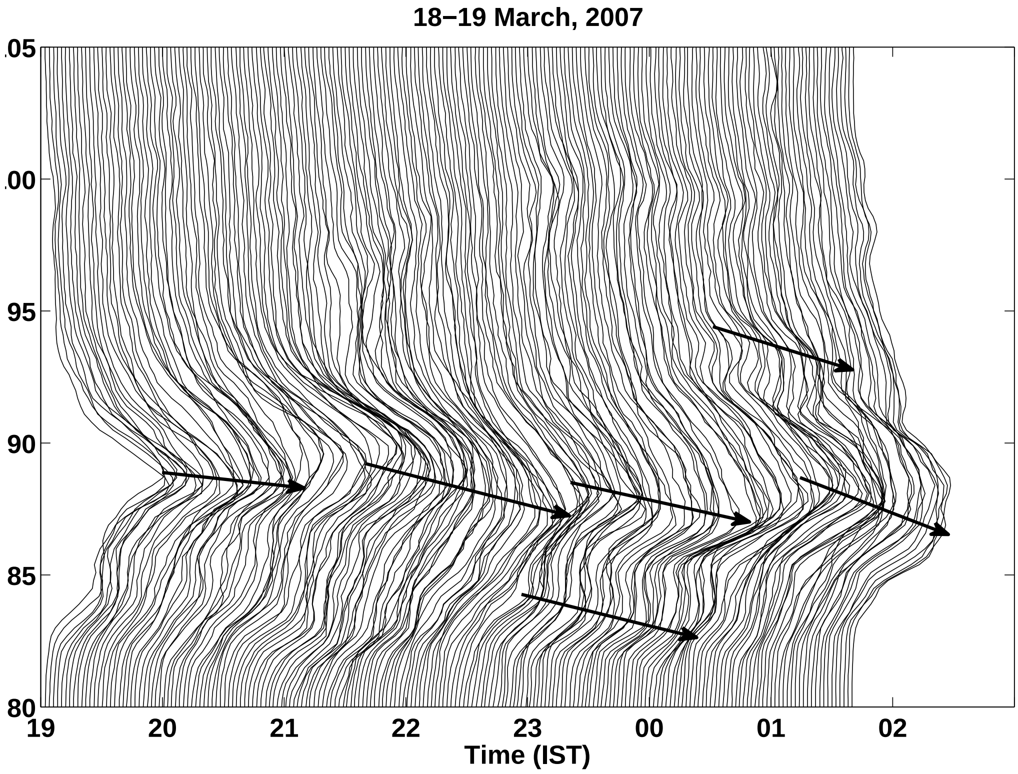

Figure 4.1: Time series of Na concentration profiles on 18-19 March, 2007. Inclined arrows represent phase propagation of gravity waves.

Airglow emissions can also be used as tracers to understand the dynamical processes of upper atmosphere. Different airglow emissions originate due to various chemical reactions and these reactions are favored at certain altitudes. Therefore, to understand the physical phenomena at different altitudes, different airglow emissions can be studied. In order to probe mesosphere and lower thermosphere regions, OH band emission (720-910 nm), NaD (589.0/589.6 nm) and OI (557.7 nm) emission lines are generally used. 557.7 nm emission comes from around 97±2 km and it occurs due to three body recombination of atomic oxygen (O). OH band emission occurs due to transition between rotational energy levels in a vibrational band of hydroxyl radical (OH) and this emission comes from around 85±5 km. Na airglow emission produced at ∼90±5 km altitude also serves as tracer for AGWs. Thus, using airglow photometer and imager, this modulation in the airglow intensity can be recorded and the periodicities as well as horizontal wavelengths of gravity waves can be determined.

Investigations of mesospheric gravity waves have been carried out over different latitudes using airglow photometry and imaging techniques. A considerable number of observations were carried out over high-latitude stations using mesospheric airglow emission lines along with radio techniques [e.g. *Suzuki et al.,* 2009a; *Nielsen et al.,* 2009]. These measurements reveal the occurrence of short period (5-15 and 6-12 minutes) and long period (30-80 minutes) gravity waves. In addition, *Bageston et al.* [2009] observed, based on OH airglow images, that the periods were mainly distributed between 5 and 20 minutes over Comandante Ferraz, an Antarctica Station (62.1° S, 58.4° W). Similar to high latitude stations, airglow observations were also carried out at mid-latitudes. The dominant modes were found to be less than 30 minutes [e.g. *Swenson et al.,* 1999; *Higashikawa et al.,* 1999; *Reid and Woithe,* 2005; *Wrasse et al.,* 2006a]. However, *Won et al.* [2003] observed longer periods (>2 hours) in OH airglow images from another mid-latitude station like Chungirvon (36.6° N, 127.3° E), Korea.

Substantial measurements were also carried out from equatorial and low latitude stations. *Taylor et al.* [1995b, 1997] observed the occurrence of short periods (< 20 min) from Alcantara, Brazil (2.3° S, 44.5° W) and Haleakala Crater, Maui (20.8° N, 156.2° W in images of near-infrared OH and O_2 airglow as well as in visible OI (557.7 nm) and NaD (589.2 nm) airglow. *Mukherjee* [2003] investigated the short period of gravity waves of around 8 min over Panhala (17.0°N, 74.2°E), a Indian low latitude station. Recently, *Suzuki et al.* [2009b] estimated the periods of gravity waves that lie between 5 and 25 min using OH airglow imaging and meteor radar over Kototabang (0.2° S ,100.3° E).

Fagundes et al. [1995] carried out measurements of O_2 (0,1) and OH (9,4) band as well as OI (557.7 nm) and NaD line emissions obtained from Cachoeira Paulista (23° S, 45° W), Brazil. The investigation revealed the presence of gravity waves with periodicities more than 60 minutes. However, short period gravity waves (less than 16 min) were also observed from several low-latitude stations [e.g. *Nakamura et al.,* 2003; *Medeiros et al.,* 2003; *Pautet et al.,* 2005; *Wrasse et al.,* 2006b]. Recently, *Taylor et al.* [2009] derived periods of gravity waves over Brasilia (14.8° S, 47.6° W) and Cariri (7.4° S, 36.5° W) using airglow imaging technique. The observations brought out the occurrence gravity waves with short scale (5-8 min) and medium scale (20-40 and 40-60 min) periods over both Cariri and Brasilia.

4.1.3 Breaking of Gravity Waves in Mesosphere

Breaking of gravity waves plays an important role in mesospheric energetics. Instability processes are believed to be responsible for the breaking of gravity waves near mesopause region. *Hodges* [1967] and *Lindzen* [1981] suggested that the breaking of gravity waves arises from convective instability. This can be quantified using the square of Brunt-Vaisala frequency (N^2). This is the frequency at which a displaced air parcel oscillates when displaced vertically within a stable environment under the influence of buoyancy as a restoring force. The expression for N^2 is as follows

$$N^2(z) = \frac{g}{T(z)}\Big[\frac{g}{C_p} + \frac{dT(z)}{dz}\Big] \tag{4.1}$$

Where, $T(z)$ = Temperature at height z (in meter).
g = Acceleration due to gravity (in m/s^2)
C_p = Molecular specific heat at constant pressure (29.1 J.mol^{-1}.K^{-1} for diatomic molecules like N_2 and O_2)

Convective instability occurs in the region of atmosphere where negative temperature gradient exists and $N^2(z)$ becomes negative. Therefore, equation 4.1 suggests that the atmosphere will be convectively unstable and favorable for the generation of turbulence whenever $dT/dz + g/C_p$ is negative.

In addition to convective instability, dynamical instability is also responsible for breaking of AGWs. The dynamical instability can be gauged by the Richardson number (R_i) [*Richardson,* 1920].

$$R_i(z) = \frac{N^2(z)}{(du/dz)^2 + (dv/dz)^2} \tag{4.2}$$

where, $u(z)$ and $v(z)$ are the zonal and meridional winds (in m/s) at an altitude z.

The numerator in the expression of R_i is the square of Brunt-Vaisala frequency (N). This is a measure of the stability of atmosphere. The denominator of equation (4.2) represents the destabilizing effects due to wind shear in the atmosphere. The dynamical instability may be excited to cause turbulence, if the wind shear effect overwhelms the buoyancy effect so that the Richardson number is less than 0.25 [*Chu et al.,* 2007].

As discussed in *Hecht et al.* [2004], convective and dynamical instabilities occur in mesosphere depending on critical values of $N^2(z)$ and R_i. Whenever R_i is less than 0.25, dynamical instability occurs which leads to the formation of Kelvin-Helmholtz billows [*Gossard and Hooke,* 1975]. On the other hand, convective instability occurs if N^2 is negative when the atmospheric lapse rate exceeds the adiabatic lapse rate.

Gravity wave breaking has been extensively investigated with theoretical analyses and numerical simulations [e.g., *Lindzen,* 1981; *Fritts et al.,* 1994; *Liu et al.,* 1999]. Several critical factors control the process of the wave breaking. This includes the growth of the wave amplitude with height, the thermal structure and wind velocity profile of the background environment. The wave breaking process can be roughly described when the temperature and wind velocity perturbations of the upward propagating gravity wave grow with height. If the overturning in the temperature field occurs at the height where the wave-induced temperature gradient exceeds the background temperature gradient, the convective instability is likely to occur and the turbulence is generated to cause wave breaking. The dynamical instability may also occur due to large velocity shears in the ambient wind. As discussed in *Chu et al.* [2007], the dynamic instability will occur subsequently on the upper and lower sides of the accelerated mean flow when the wind shears become sufficiently large. The later stage of wave breaking will therefore have a complicated distribution of turbulence because of the combination of Kelvin-Helmholtz turbulence [*Hecht et al.,* 2005; *Li et al.,* 2005] and convective instability-generated turbulence in the wave breaking zone.

4.1.4 Breaking of Gravity Waves Observed in Airglow

Apart from the characterization of gravity waves, the signature of breaking of gravity waves in mesospheric airglow have been observed by several researchers. *Swenson and Mende* [1994] observed the evidence of breaking of gravity waves at upper mesosphere in OH airglow images over Utah State University Observatory at Bear Lake, Utah. Based on airglow and lidar observations in Urbana, Illinois (40°N), *Hecht et al.* [1997, 2000b] observed a few small-scale wave-like structures in OH and O_2 airglow images that could be associated with the breaking of gravity waves due to convective instability. In addition, using an OH airglow imager and a meteor radar over Japan, *Yamada et al.* [2001] observed a few cases where breaking of small-scale gravity waves occurred in the mesopause region that propagated against background wind. One such example provided by *Yamada et al.* [2001] is illustrated in Chapter 1.

In the present thesis, indirect indication for the breaking of gravity waves in Na airglow layer was obtained using observations from a ground-based Na airglow photometer along with the different instruments onboard TIMED (Thermosphere Ionosphere Mesosphere Energetics and Dynamics) satellite.

4.2 Data Set

In order to measure the temporal variation of Na airglow intensity, portable narrow-band photometers were designed and fabricated. The detailed specifications of these photometers are already discussed in Chapter 2. Na airglow intensity with temporal resolution of 10 s was obtained using those photometers from Mt. Abu and Gadanki during moonless nights in cloudless season.

In order to assess the effect of mesopause height on the observed Na airglow variation, the altitude profiles of mesospheric kinetic temperature are obtained from SABER instrument onboard TIMED satellite nearly over both Mt. Abu and Gadanki on observational nights.

Mesospheric zonal and meridional wind profiles nearly over Mt. Abu and Gadanki were obtained from the TIMED Doppler Interferometer (TIDI) measurements in the mesosphere and lower thermosphere region. The brief specifications pertaining to the SABER and TIDI instruments are discussed in Chapter 2.

4.3 Data Analyses

In order to identify the modes of mesospheric gravity waves, Na airglow measurements, carried out in campaign modes during November, 2006 - February, 2009 from Mt. Abu (24.6° N, 72.7° E) and Gadanki, were used. A total of 80 nights over Mt. Abu and 30 nights of data over Gadanki were collected during the course of the thesis work. Moonless and cloudless conditions required for the airglow measurements limit the number of observations. Spectral components are obtained for all these cases. In addition, based on a few distinct cases, investigation is also carried out to understand the relation between the propagation of gravity waves and mesopause altitudes.

Na airglow photometer measures time series of terrestrial Na airglow emission intensity in terms of photon counts/s. A few sharp peaks, observed in the temporal variation, are identified as extra-terrestrial origin as each peak systematically shifts around 4 minutes on a given night as compared to the previous night. These are removed from the original data set in each night to avoid extra-terrestrial contribution in Na airglow intensity. Data points during passage of thin clouds, haze are also rejected. As a consequence, the time series of Na airglow intensity becomes unevenly-spaced in time domain.

The gravity wave-induced small scale intensity fluctuations (less than 3 hrs) are embedded in the large scale variation of the unevenly-spaced time series data. In order to extract the small scale fluctuations, filtering technique is used by detrending the large scale variation in Na airglow intensity. The mean of the residuals is then subtracted from each datum point of residual time series to minimize the probable bias [*Koopmans*, 1974]. Spectral analysis is thus performed on the unevenly-spaced normalized residual time series using Lomb-Scargle method which is capable of handling unevenly-spaced time series data. The spectral peaks above the critical level (g_f) determined by Fisher's test [*Schulz and Stattegger,* 1997] are considered to be "significant". In addition, the frequency components satisfying "Nyquist Criteria" are only considered. Further, the periods, below the "Brunt-Vaisala" period, which is around 5 minutes at Na airglow emission altitude, are not considered. The periods obtained from the spectral analysis satisfying all the above conditions, for all the nights of observations in each month, are binned for every 15 minutes time interval. Thus, the percentage of occurrence and occurrence of maximum power of gravity wave modes are evaluated.

Figure 4.2 depicts a typical nocturnal Na airglow intensity variation and the power spectrum analysis technique applied for a given Na airglow intensity time series. As mentioned earlier, the time series data of Na airglow is unevenly-spaced due to extra-terrestrial contribution and/or passage of thin clouds and contains small and large scale fluctuations. The black curve in Figure 4.2a represents the temporal variation of Na airglow intensity in terms of counts/s. The gray curve in Figure 4.2a represents the time series after suitable low pass filtering. It must be noted that the appropriate low pass filtering is carried out using running average in time domain so that gravity wave fluctuations with periods ranging from 5 min to 3 hours are smoothed out. Now, this smoothed time series is used to extract the fluctuations due to gravity waves. The residual time series, thus obtained, is normalized with respect to the maximum count for that night. The normalized residual time series is shown in Figure 4.2b. Figure 4.2c shows the Lomb-Scargle periodogram of the unevenly-spaced normalized residual (black curve). The gray curve in the same subplot represents the Fisher (g_f) level above which the spectral peaks are considered 'significant'. As the average ambient wind speed within the Na airglow layer is less, the Doppler shift of the observed frequency is extremely small. Therefore, the significant spectral peaks calculated from Lomb-Scargle periodogram analysis can be considered to be the representative frequency due to passage the gravity waves through Na airglow layer.

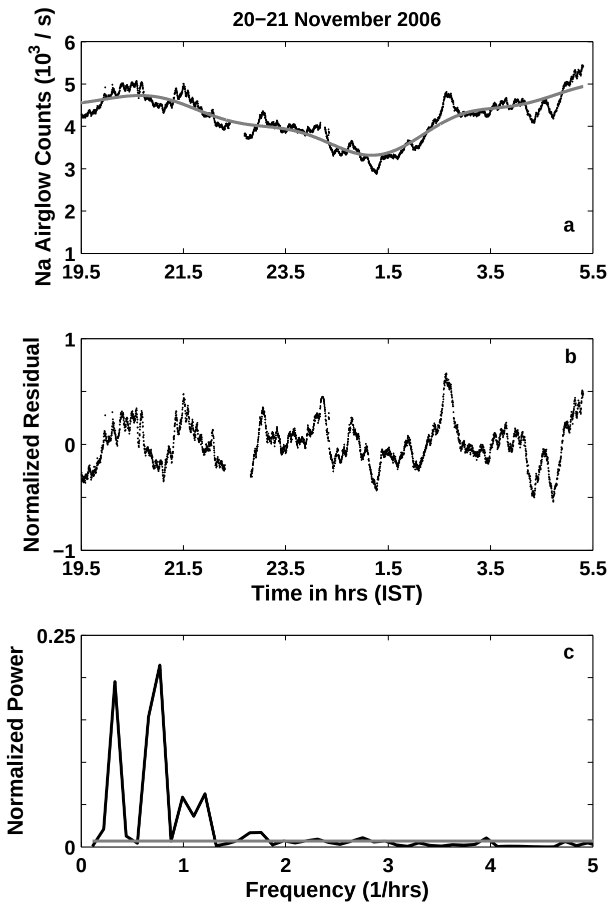

Figure 4.2: (a) Na airglow intensity variation in terms of Counts/s (black curve) overlaid on the smoothed time series (gray curve). (b) Normalized residual time series after detrending the Na airglow intensity variation. (c) Normalized power spectrum using Lomb-Scargle periodogram of the unevenly-spaced normalized residual (black curve) overlaid on the fisher fisher (g_f) level above which the spectral peaks are considered.

In order to investigate the occurrence of convective and dynamical instabilities within Na airglow layer, the square of the Brunt-Vaisala frequency (N^2) and the Richardson number (R_i) profiles on those nights were calculated using SABER derived mesospheric temperature profile and TIDI derived zonal (u) and meridional (v) wind profiles nearly over the observational sites during nighttime.

4.4 Results

Figures 4.3 and 4.4 depict the normalized nocturnal variations during 19.5-05.5 IST of Na airglow intensity over Mt. Abu and Gadanki respectively. The normalization procedure were carried out by dividing each datum point of Na airglow intensity by the maximum value of Na airglow intensity on a given night. Significant difference is observed in the Na airglow intensity levels from one night to another.

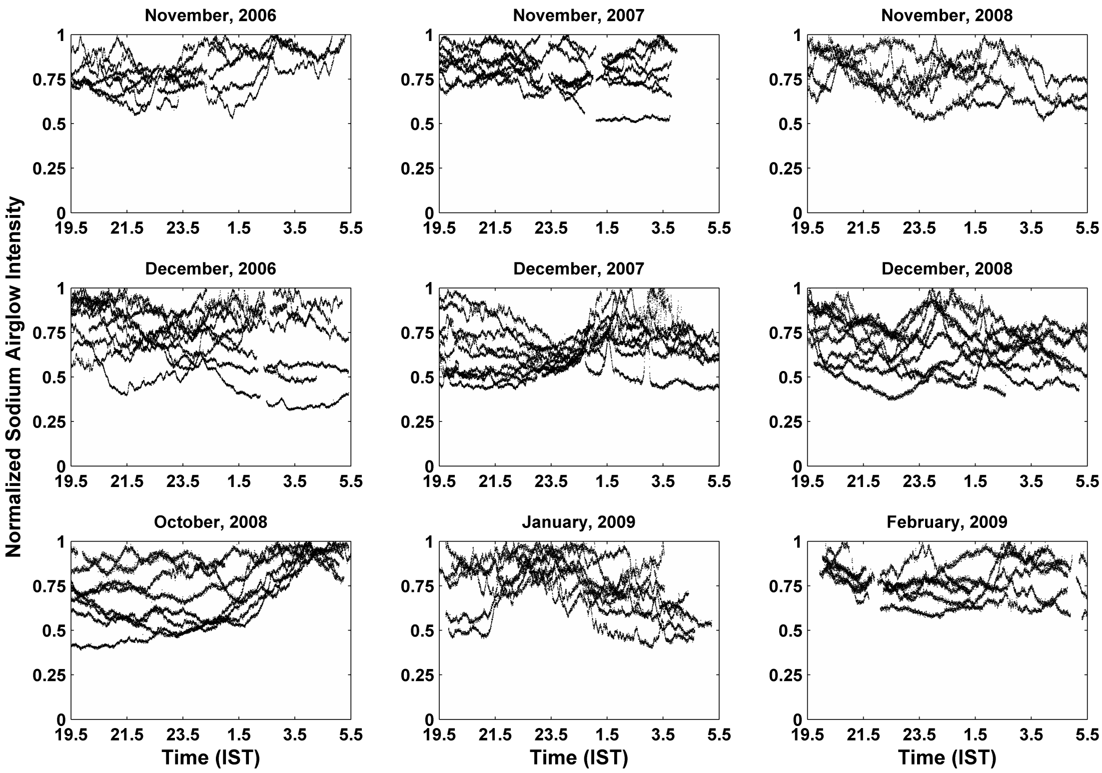

Figure 4.3: Normalized Na airglow intensity variation measured from Mt. Abu during different months.

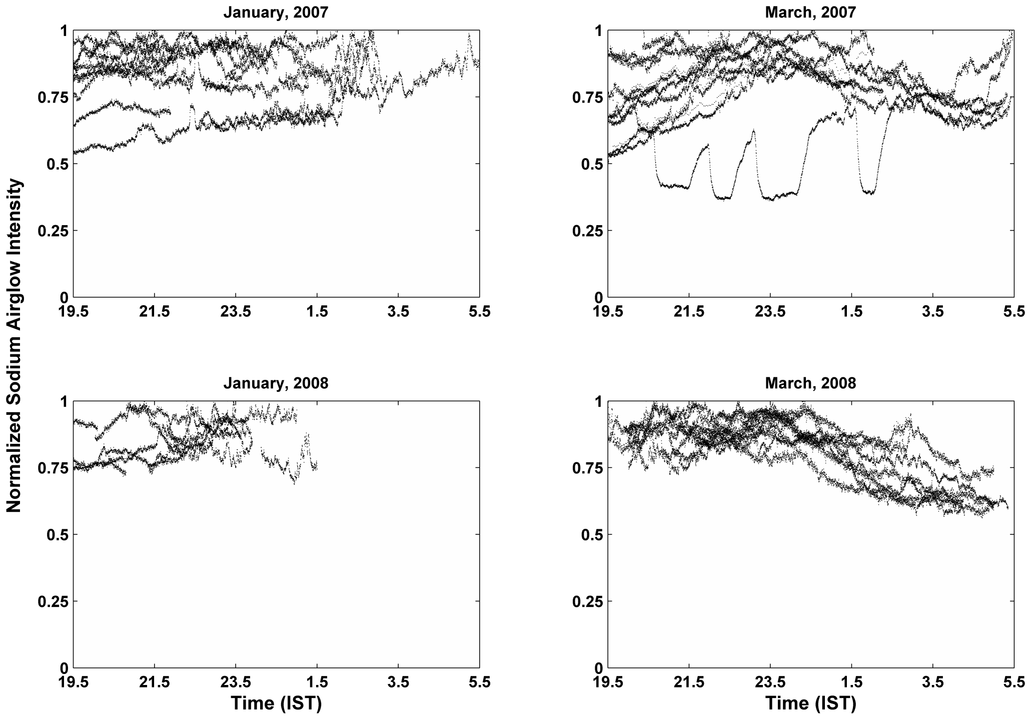

Figure 4.4: Normalized Na airglow intensity variation measured from Gadanki during January and March of 2007 & 2008.

Significant night-to-night variabilities on a given month are observed over both Mt. Abu and Gadanki. In addition, the nocturnal Na airglow intensity variations differ from year to year. The salient observational features are listed below.

- The nocturnal Na airglow intensity variations over Mt. Abu during December, 2006 and 2008 are significantly different as compared to the variations during December, 2007. The peaks in the airglow intensity occurred during midnight during 2006 and 2008. However, the airglow intensities maximize well after midnight during December, 2007. On the contrary, the nocturnal variations during November for the years 2006, 2007 and 2008 do not reveal any systematic occurrence of intensity peaks.

- The airglow intensity variations over Mt. Abu on each night during October, 2008 reveal the occurrence of peak intensity during pre-dawn hours (around 4:30 IST). On the other hand, the intensity variations do not show any systematic intensity peak during February, 2009.

- Nocturnal airglow intensity variations over Mt. Abu show a hump like structure between 21:30 to 01:30 IST during January, 2009.

- The variation on a particular night during March, 2007, where intensity shows quasi-periodic oscillation, is noticed. The Na airglow intensity variation on this night is entirely different from other nights during this month and is addressed in detail in Chapter 3.

- The intensity during March, 2008 decreases consistently during post-midnight hours.

  The wave induced fluctuations can be observed in the temporal variation during all nights. In order to derive the periodicities associated with the gravity waves embedded in the Na airglow intensity variations, spectral analyses were carried out as discussed in the data analyses section.

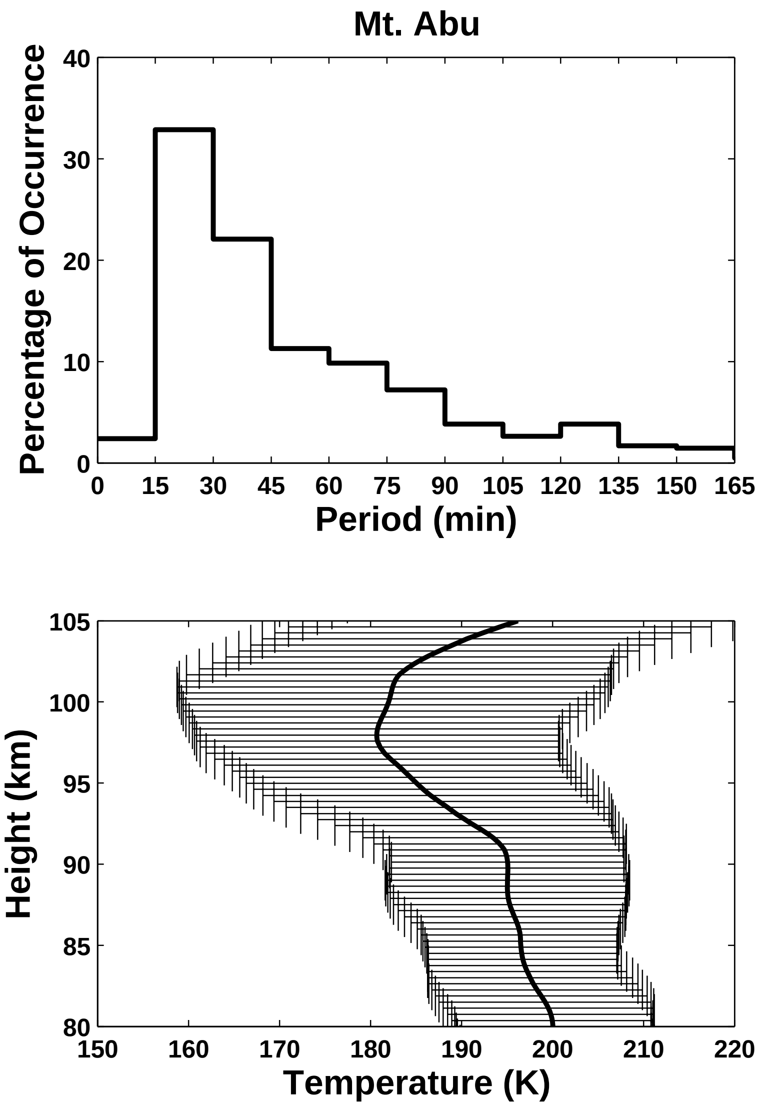

Figure 4.5: The upper subplot depicts the occurrence of maximum power derived from Na airglow intensity variation over Mt. Abu. The variations in temperature profile obtained from SABER during all the observational nights over Mt. Abu are shown in the lower subplot along with the average temperature profile (bold black curve).

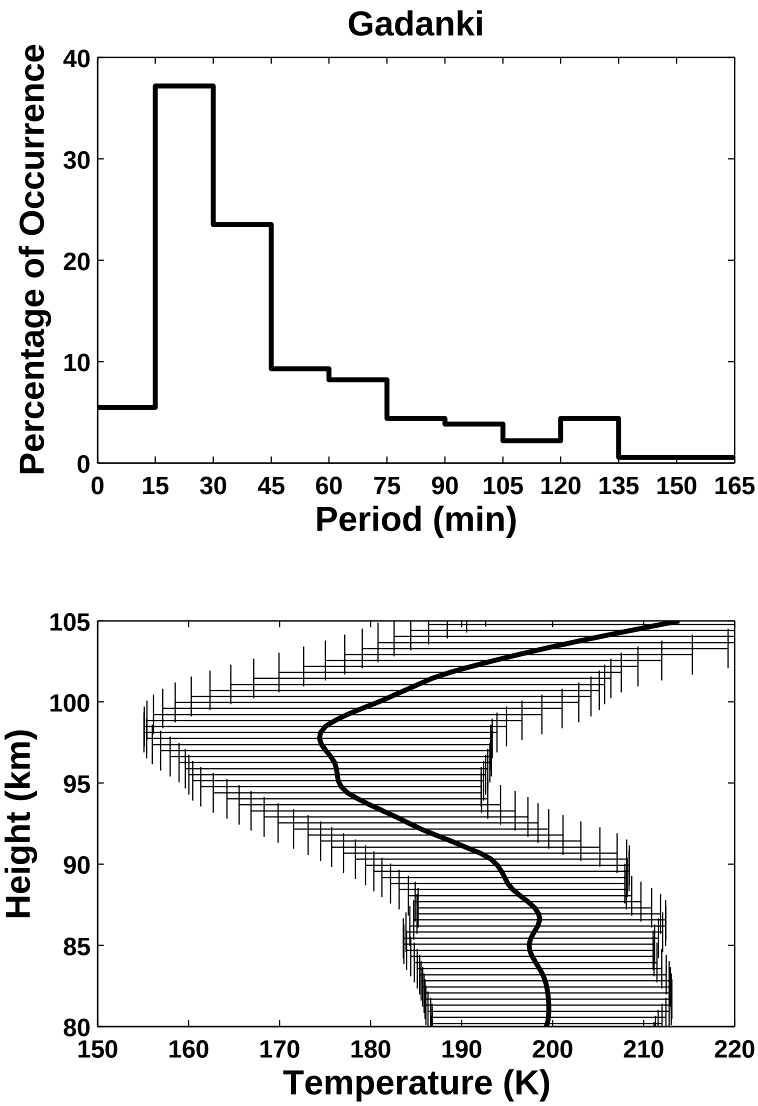

Figure 4.6: The upper subplot depicts the occurrence of maximum power derived from Na airglow intensity variation over Gadanki. The variations in temperature profile obtained from SABER during all the observational nights over Gadanki are shown in the lower subplot along with the average temperature profile (bold black curve).

Figures 4.5 depicts the histogram obtained with the percentage of occurrence associated with the gravity wave modes over Mt. Abu along with the altitude profiles of temperatures during the observational period. Similar analyses over Gadanki are plotted in Figure 4.6. It is interesting to note that the percentages of occurrence of periods of atmospheric gravity waves in the nocturnal Na airglow variation both over Mt. Abu and Gadanki maximize for the period between 15 to 30 minutes. In addition, the average altitude profile of mesospheric temperature during the observational period obtained from SABER over both Mt. Abu and Gadanki, reveals that the mesopause altitude is around 98 km. It is interesting to note that the deviations of temperature for those nights both over Mt. Abu and Gadanki are observed to increase beyond 90 km.

In addition to the occurrence of gravity wave periods described above, percentage of occurrence of periodicities with maximum spectral power of gravity waves is also calculated to investigate the impact of a particular gravity wave mode in the energetics of mesosphere. Figure 4.7 represents the percentage of occurrences of maximum power over Mt. Abu and Gadanki. There are three spectral components containing large powers (marked by arrows) having the periodicities that lie within 45-60, 75-90 & 90-105 minutes over Mt. Abu and 30-45, 75-90 & 105-120 minutes over Gadanki.

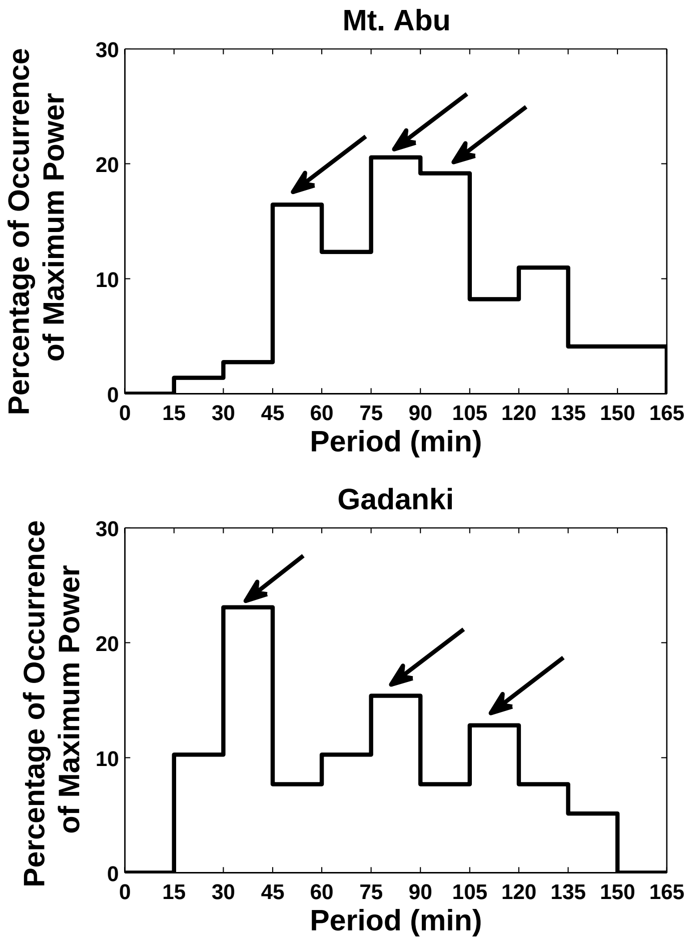

Figure 4.7: The upper and lower subplots depict the occurrence of maximum power derived from Na airglow intensity variations over Mt. Abu and Gadanki respectively.

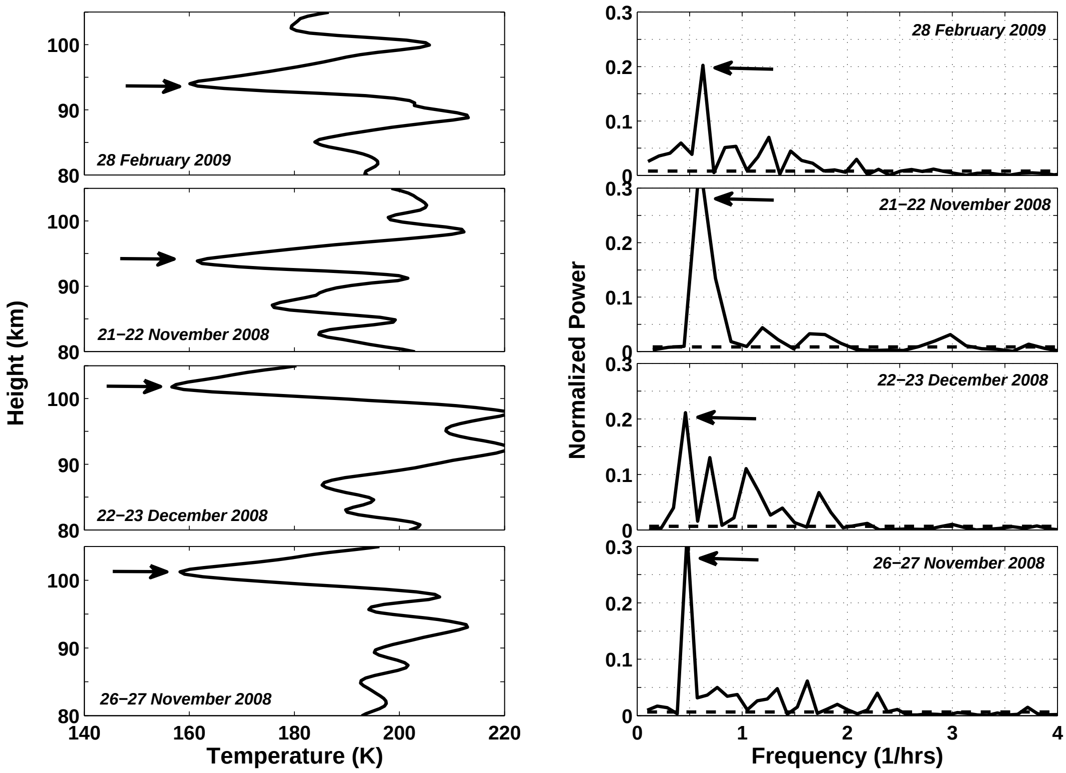

Figure 4.8: The left panel shows the mesospheric temperature profile obtained from SABER over Mt. Abu on a few distinct nights. The subplots in the right panel depict the power spectra derived from the temporal variations of Na airglow intensity on those respective nights.

The left panel of Figure 4.8 depicts mesospheric temperature profiles obtained from SABER on a few distinct nights over Mt. Abu. The right panel shows the power spectra derived from Na airglow intensity variation recorded from Mt. Abu on those nights. It is to be noted from the first two subplots (28 February, 2009 and 21-22 November, 2008) that the mesopause altitude is below 93 km and the corresponding dominant period is around 90 min. Interestingly, steep negative gradients in temperature (< -10 K/km) within the altitude range of 85-97 km are observed on those two nights. In contrast, the dominant period of gravity waves observed on 22-23 December, 2008 and 26-27 November, 2008 is more than 120 min. The mesopause heights on those cases lie well above 100 km. It is also observed that negative temperature gradients are relatively less steep (> -5 K/km) within 85-97 km during those nights. It is to noted that the altitude region between 85 to 97 km is the Na airglow emission region and the importance of this aspect will be discussed later.

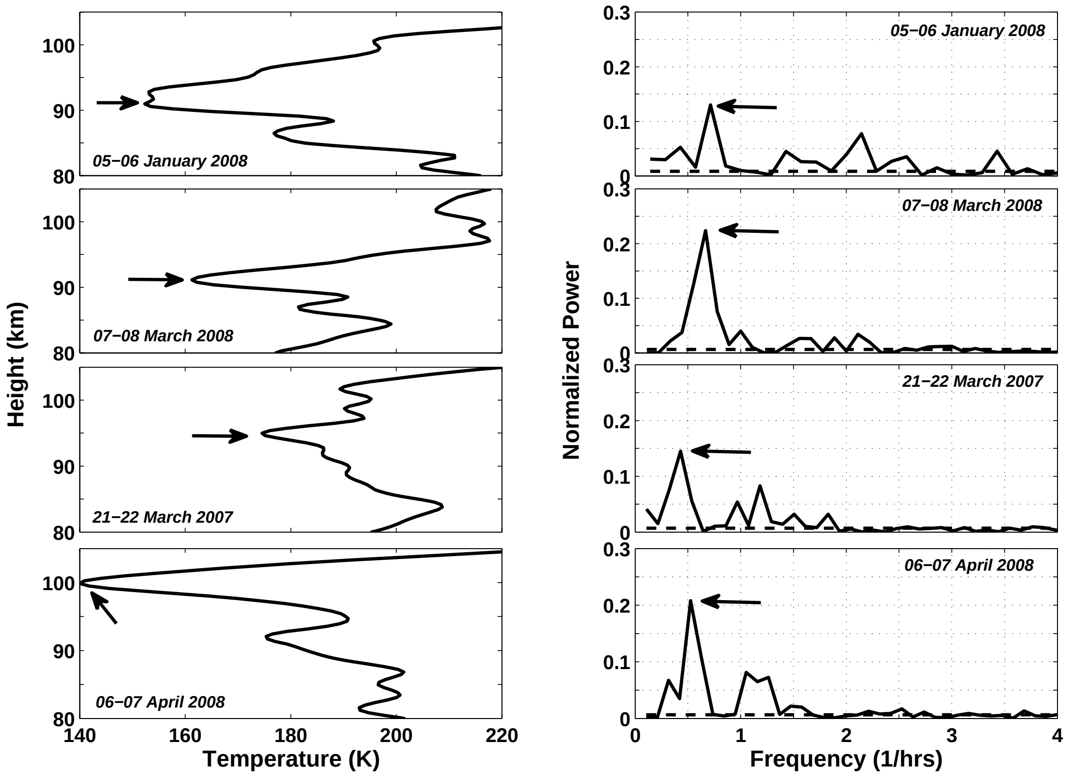

Figure 4.9: The left panel shows the mesospheric temperature profile obtained from SABER over Gadanki on a few distinct nights. The subplots in the right panel depict the power spectra derived from the temporal variations of Na airglow intensity on those respective nights.

Similar features are also be observed over Gadanki (Figure 4.9) wherein the periods of gravity waves on a few distinct occasions are found to be different depending on the levels of mesopause height and gradient in temperature. The dominant periodicities derived from Na airglow intensity variation on 05-06 January, 2008 and 07-08 March, 2008 are less than 90 min and in these cases, the mesopause altitude lies around 90 km and the steep negative gradient in temperature (< -10 K/km) exists within 85-97 km. In addition to that, periodicities of around 120 min are observed to be dominant on 21-22 March, 2007 and 06-07 April, 2008 when the mesopause altitude lies beyond 97 km with relatively less negative temperature gradient (> -6 K/km).

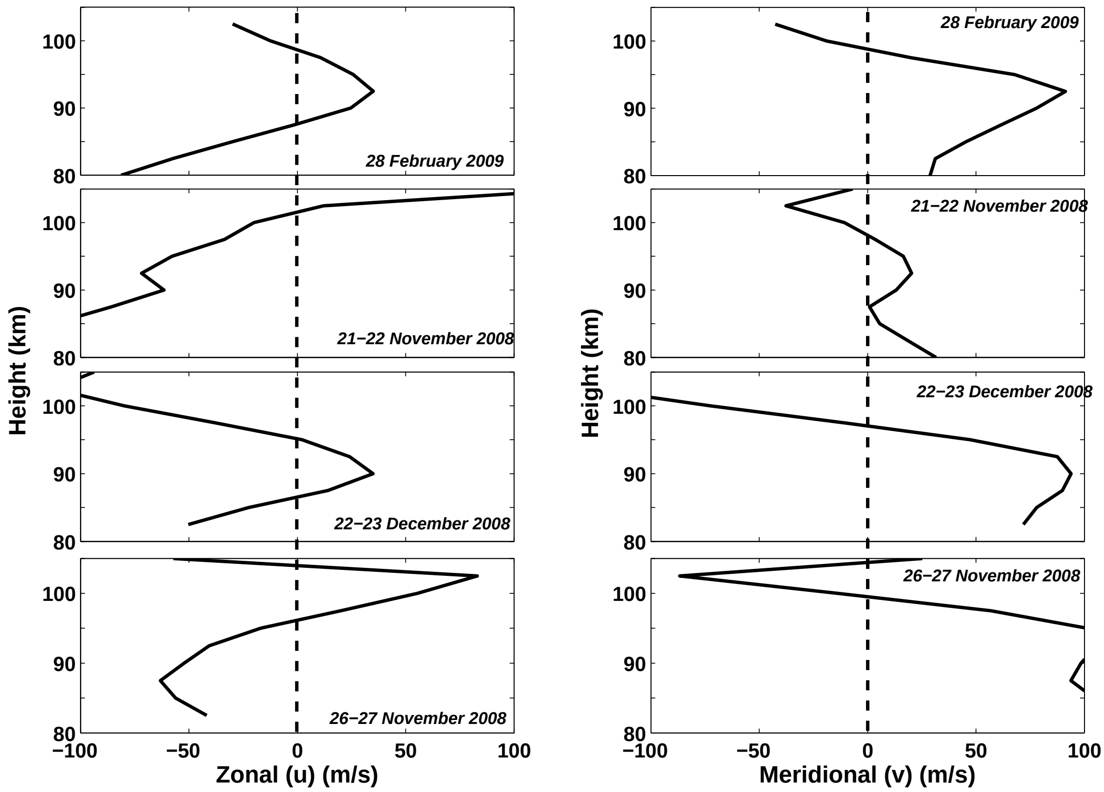

Figure 4.10: The left panel shows zonal wind profiles over Mt. Abu on those nights considered in Figure 4.8. Positive and negative signs in zonal wind respectively indicate the direction to be eastward and westward. The subplots in the right panel depict meridional wind profiles on those respective nights. Positive and negative signs in meridional wind respectively indicate the direction to be northward and southward.

Figures 4.10 and 4.11 depict the profiles of zonal and meridional winds obtained from TIDI in the altitude range of 80-105 km nearly over Mt. Abu and Gadanki respectively. A large night-to-night variations in the magnitude of both zonal and meridional winds are noted. In addition to that, significant velocity shears are present in both zonal and meridional winds in the altitude region of 85-97 km. TIDI derived wind profiles during nighttime are used to derive the altitude profiles of Richardson number on those nights.

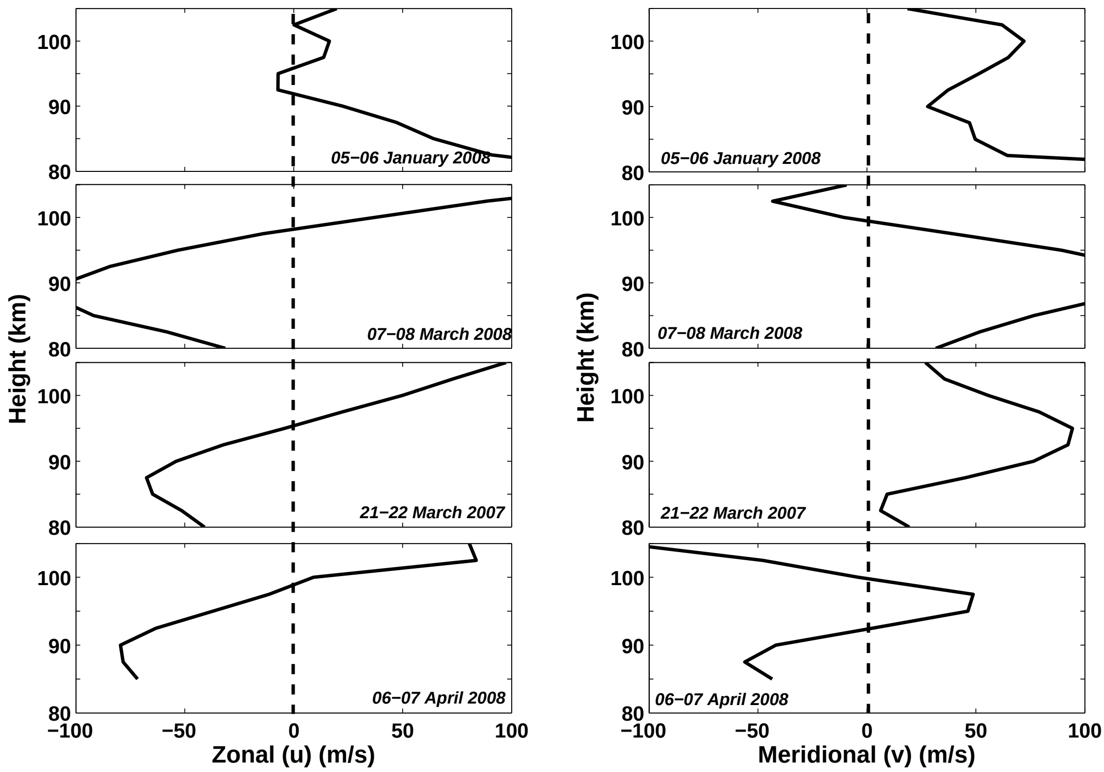

Figure 4.11: The left panel shows zonal wind profiles over Gadanki on those nights considered in Figure 4.9. Positive and negative signs in zonal wind respectively indicate the direction to be eastward and westward. The subplots in the right panel depict meridional wind profiles on those respective nights. Positive and negative signs in meridional wind respectively indicate the direction to be northward and southward.

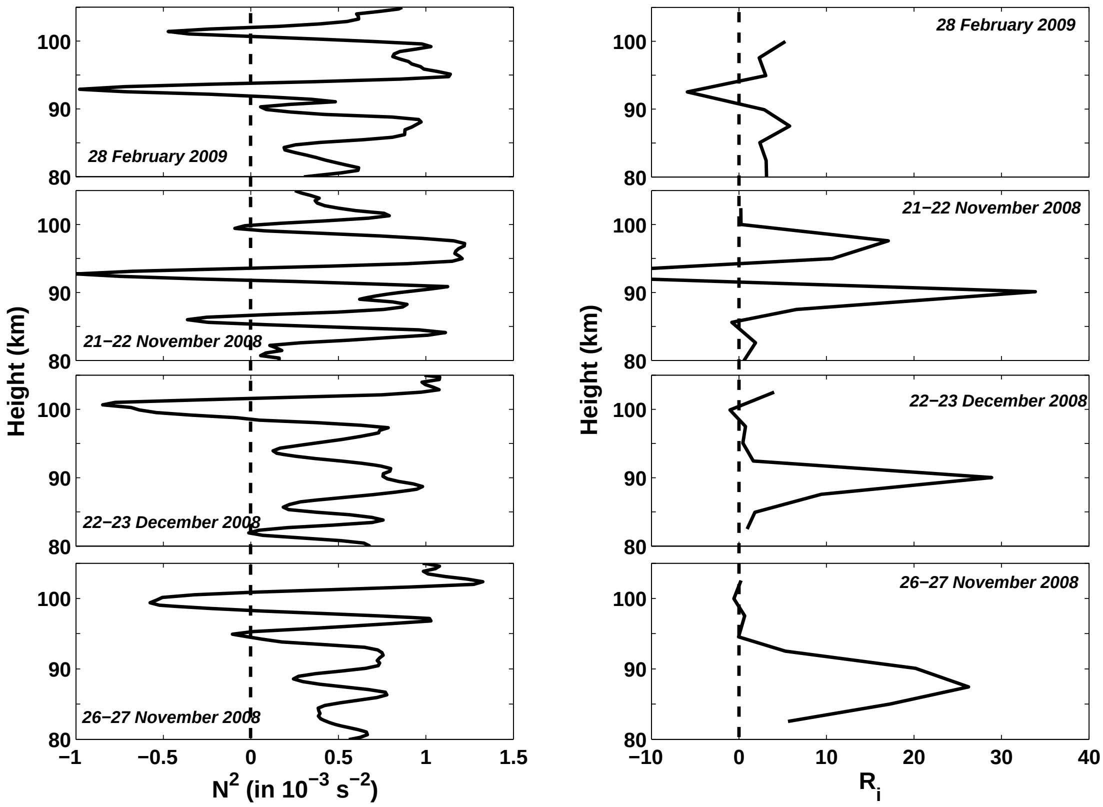

Figure 4.12: The left panel shows N^2 (N = Brunt-Vaisala frequency) profiles over Mt. Abu on those nights considered in Figure 4.8. The subplots in the right panel depict R_i (Richardson Number) profiles on those respective nights.

The left panel of figure 4.12 depicts altitude profiles of N^2 over Mt. Abu in the altitude range of 80-105 km obtained using the SABER derived temperature profiles in equation 4.1. The altitude profile of Richardson number (R_i), calculated from N^2 using equation 4.2 on those nights, are plotted in the right panel of this figure. Several interesting aspects can be noted based on the N^2 and R_i values. Figure 4.12 reveals that N^2 becomes negative and R_i is less than 0.25 within the altitude range of 85-97 km on 28 February, 2009 and 21-22 November, 2008. Interestingly, the dominant period of gravity waves, present over Mt. Abu for these two nights, is around 90 min (Figure 4.8). However, N^2 becomes negative and R_i is less than 0.25 beyond 95 km on 22-23 December, 2008 and 26-27 November, 2008 and the dominant period derived from Na airglow intensity variation is more than 120 min on those two nights over Mt. Abu. (Figure 4.8).

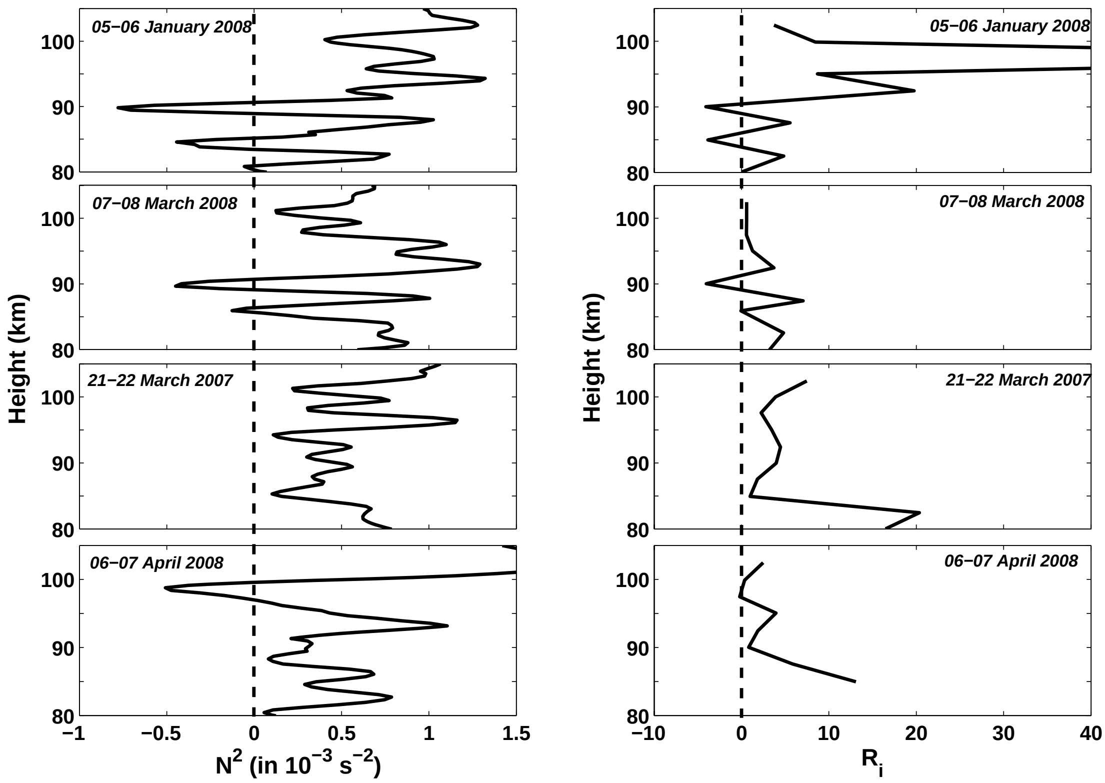

Figure 4.13: The left panel shows N^2 (N = Brunt-Vaisala frequency) profile over Gadanki on those nights considered in Figure 4.9. The subplots in the right panel depict R_i (Richardson Number) profiles on those respective nights.

Similarly, observations obtained on 05-06 January, 2008 and 07-08 March, 2008 from Gadanki suggest that the dominant period present in Na airglow intensity is less than 90 min (Figure 4.9) whenever N^2 becomes negative and R_i is less than 0.25 within the altitude of 85-97 km (Figure 4.13). However, N^2 and R_i were respectively not observed to be negative and below 0.25 within 85-97 km (21-22 March, 2007 and 06-07 April, 2008). The dominant period is found to be more than 120 min (Figure 4.9). Comparison of Figures 4.8, 4.9, 4.12 and 4.13 clearly reveal that the dominant periods, associated with the gravity wave activities, are less (~90 min) whenever the value of N^2 is negative and R_i is less than 0.25 within altitude region of 85-97 km. In other cases, the dominant period is significantly greater (~120 min) whenever N^2 and R_i were respectively not observed to be negative and below 0.25 within 85-97 km.

4.5 Discussion

It is well known that neutral Na layer will be modulated by the passage of gravity waves as, the lifetime of neutral Na atoms during nighttime is long compared to the typical gravity wave periods [*Xu and Smith,* 2003]. These waves, propagate upward and carries energy and momentum from lower to upper atmosphere. The downward phase propagation of these waves (Figure 4.1) suggest that these are gravity waves. Therefore, the modulations in the Na concentration reported here are due to the propagation of gravity waves through Na atom layer.

It is to be noted that the identification of the Na airglow layer height region was reported earlier based on several in-situ and ground based measurements [*Clemesha et al.,* 1993, 1995; *Hecht et al.,* 2000; *Sarkhel et al.,* 2010] and it was found to lie in between 88 to 97 km. Moreover, the reaction time constant of Na airglow emission in the Chapman mechanism [*Chapman,* 1939] is around a few seconds [*Plane et al.,* 1993], the gravity waves having periods greater than the reaction time constant can, in principle, be recorded.

The modulation in Na airglow intensity due to the passage of gravity waves through Na airglow layer are indicated by the percentage of occurrence. It is interesting to note that the night-to-night variation in temperature near mesopause region is substantially large over Mt. Abu and Gadanki. The variations in temperature can be interpreted due to the passage of gravity waves as it modulate temperature. This large amount of variation in temperature near mesopause region is owing to the fact that the gravity waves play a crucial role in the energetics near mesopause region. The energetics in upper mesosphere are described by the occurrence of gravity waves with maximum power in which the larger power indicates the gravity wave periods that are mainly responsible for altering mesospheric temperature. These waves transport energy and momentum from lower atmosphere and dump at the altitude region where they break. As a consequence, energy and momentum are transferred to the ambient medium.

The convective and dynamical instability processes are responsible for the breaking of gravity waves near the mesopause region. The steep negative temperature gradient makes the ambient atmosphere convectively unstable whereas, the shear in the horizontal velocity can trigger dynamical instability. The square of Brunt-Vaisala frequency (N^2) and the Richardson number (R_i) respectively are the measures of convective and dynamical instabilities. These processes occur at the altitude regions where N^2 is negative and R_i goes below 0.25. In the present investigation, both convective and dynamical instabilities are observed to occur within the Na airglow layer on a few nights. The power spectra on those nights reveal that the dominant periods are 90 min. On other occasions, the dominant periodicites are observed to be larger (>120 min) when the instabilities occurred above the Na airglow altitude region. From Figure 4.7, it is clear that in case of more than 10% of the total nights of observation, both the periodicities of gravity waves are found to be dominant. As discussed in *Hines* [1960, 1964], if the periodicity is much greater than the Brunt-Vaisala period (∼5 min in mesosphere), the horizontal wavelength associated with gravity waves are proportional to the periodicity assuming the vertical wavelength to be nearly constant. Thus, in the present investigation, smaller horizontal scale sizes appeared whenever instabilities occurred within Na airglow layer. On the other hand, larger horizontal scale scales are observed whenever instabilities occurred beyond Na airglow layer. As reported by other researchers [*Hodges,* 1967; *Orlanski and Bryan,* 1969; *Geller et al.,* 1975; *Hecht et al.,* 1997; *Nakamura et al.,* 2005], the breaking of gravity waves, triggered by those instabilities near mesopause region, lead to the production of turbulence and as a consequences, smaller scale gravity waves possibly got generated. In the present investigation, the smaller horizontal scale sizes waves are observed that might have generated from the breaking of gravity waves due to occurrence of convective and dynamical instabilities within Na airglow layer identified on a few nights using SABER and TIDI instruments onboard TIMED satellite. The ground based observations by the Na airglow photometer, on those occasions, possibly indicate the breaking of gravity waves due to those instabilities. The three independent measurements bring out the occurrence of convective and dynamical instabilities within Na airglow layer that leads to the breaking of gravity waves into smaller scale sizes.

The breaking of these gravity waves near mesopause can induce the generation of secondary waves [*Vadas et al.,* 2003]. These waves propagate upward and reach thermosphere-ionosphere system. Under appropriate background ionospheric conditions, these may act as seed perturbation to generate ionospheric irregularities.

Chapter 5

Identification of Active Fossil Bubbles based on Coordinated VHF Radar and Airglow Measurements

5.1 Background

As discussed in Chapter 4, the gravity waves that are created in the lower atmosphere, break near mesopause region due to instability processes that generate secondary waves. These waves eventually penetrate through mesopause region and reach into reach Thermosphere-Ionosphere System (TIS). These are suggested to act as seed perturbations to generate plasma irregularities in the F region of ionosphere [*Rottger,* 1982; *Kelley et al.,* 1981]. These seed perturbations become the sources for the development of plasma bubbles associated with Equatorial Spread F (ESF) events. In order to understand different aspects of ESF, several coordinated measurements were carried out [e.g. *Kelley et al.,* 1986; *Raghavarao et al.,* 1984, 1987; *Sridharan et al.,* 1997]. The generation of plasma bubbles and its evolution were investigated by several techniques [*Kelley,* 1985] and simulated theoretically by nonlinear numerical models [*Ossakow,* 1981; *Raghavarao et al.,* 1992; *Sekar et al.,* 1994]. For example, *Sekar et al.* [1995] investigated the evolution of such plasma bubbles in the equatorial F region with different seeding conditions using nonlinear numerical simulation model. Seed perturbations in the ambient electron density with appropriate background ionospheric conditions evolve nonlinearly under the action of generalized Rayleigh-Taylor instability mechanism to form plasma bubbles. The background ionospheric conditions such as the F-region peak height, eastward electric field and steep plasma density gradients are, in general, suitable during post sunset time for the generation of such plasma bubbles.

The ESF structures and dynamics have been investigated using VHF radars at different parts of the globe [*Woodman and LaHoz* 1976; *Tsunoda* 1980; *Patra et al.,* 1995; *Fukao et al.,* 2004]. VHF backscatter radar is a powerful technique to probe the plasma irregularities in the entire region of ionosphere. Plasma irregularities associated with ESF show various interesting features in radar maps. The evolution of plasma plumes from the bottom side of ionosphere to the topside of the ionosphere can be unambiguously observed in the radar maps using backscatter signals. Irregularities of few meter-scale sizes are in general responsible for the VHF backscattered echo. Despite the vast usage of VHF radar to probe ionospheric irregularities, the differentiation between plasma bubbles and blobs could not be done unambiguously as the backscattered echo strength is proportional to the square of electron density fluctuations.

The plasma bubbles and blobs can be distinguished with the help of OI 630.0 nm airglow emission. This redline emission comes from around 250 km in the thermosphere during nighttime and the intensity variation is directly proportional to electron density fluctuations. In addition, the intensity variation is also controlled by ionospheric layer height variation. Thus, the simultaneous measurements of plasma irregularities using VHF radar and OI 630.0 nm airglow emission have the potential to identify plasma bubbles and blobs. Several coordinated measurements have been carried out over Indian low latitude station, Gadanki (13.5°N, 79.2°E, dip 12.5°N) using Indian VHF radar and OI 630.0 nm airglow photometer to address several aspects of ESF [*Sekar et al.,* 2004; 2008] and space weather effects [*Chakrabarty et al.,* 2005; 2006].

These plasma bubbles drift due to background eastward plasma flow and remain active till midnight in general. However, the background ionospheric conditions near midnight are not conducive for further growth. *Krall et al.* [2010] suggested that bubbles stop rising when either the local electron density inside the bubble is equal to that of the ambient plasma medium or the fluxtube-integrated electron density inside the bubble is equal to that of the nearby background. As a result, these plasma bubbles drift zonally into the field of view of measuring instruments causing spread F like signatures. These kind of non-evolving remnant plasma bubbles are generally termed as "fossil bubbles". On most of the occasions, the meter-scale size structures detectable by VHF radars disappear during this non-evolving phase leaving larger scale structures in place [*Basu et al.,* 1978].

These fossil type bubbles also drift towards east with ambient plasma motion. Though, the electron density is depleted inside such bubbles, they tend to move downward similar to the ambient plasma during non-evolutionary phase. In general, they detach from the original plasma structure and may appear as detached patches after midnight. Several indications of the presence of fossil bubbles were obtained using earlier studies. In addition to *Basu et al.* [1978], *Argo and Kelley* [1986], using digital ionosonde with the capability to identify echo location, tentatively identified a "fossil plume" which was observed as isolated scattering patches moving with ambient plasma. The implications of the "fossil bubble" in the development of post-midnight onset of ESF during June solstice of the solar minimum period where the ionosphere background condition was not conducive for plasma instability mechanism, were discussed in detail by *Sastri* [1999]. Recently, *Fukao et al.* [2005] discussed the implication of moving structures from the west of Equatorial Atmosphere Radar (EAR) (a VHF radar) site using beam steering technique. None of these techniques were capable of identifying whether the structures were depleted plasma region or enhanced region which normally moves downward. This is essentially due to the fact that the return echo strength of a VHF radar is proportional to square of the electron density fluctuations while it is well known that the bubbles cannot be detected by ground based ionosondes. In this chapter, examples are provided for "fossil bubbles" which have 3 m scale size irregularities and a plasma blob event. A possible physical scenario is also suggested wherein the "fossil bubbles" can still be "active" enough to allow generation of meter-scale irregularities.

5.2 Data Set

In order to address various aspects of ESF, coordinated radar backscatter and thermospheric airglow intensity measurements had been carried out from 2001 to 2007 over the VHF radar site at Gadanki (13.5° N, 79.2° E; dip lat 6.3° N) [*Sekar et al.,* 2004, 2008]. The author had participated in the later part of the campaign during 2006 and 2007. Coordinated observations from Gadanki were carried out in a campaign mode using VHF radar and OI 630.0 nm airglow photmeter in conjunction with the ionosonde observation at Thumba (8.5° N; 77.0° E; dip lat 0.5° N). The details of the photometer and the VHF radar are described in Chapter 2. The radar was operated in ionospheric mode wherein the beam was oriented (14.8° N from zenith) orthogonal to the geomagnetic field lines.

5.3 Results

Figure 5.1 depicts coordinated measurements of ESF events using Indian VHF radar and OI 630.0 nm airglow photometer over Gadanki on 21-22 March, 2007 during geomagnetically quiet period (A_p=1). Figures 5.1a, 5.1b and 5.1c respectively show the Range-Time-Intensity (RTI), Range-Time-Velocity (RTV), Range-Time-Width (RTW) maps of ionospheric irregularities over Gadanki measured using VHF radar. The horizontal axis corresponds to time in IST (Indian standard time = Universal time, UT+5.5 h) which is common to all subplots. The color codes in RTI represents the strength (in dB) of the backscatter radar echo from plasma irregularities and the line of sight Doppler velocity (in m/s) for RTV map. The RTW map is a measure of spectral width of the irregularities expressed in m/s.

The measurement of OI 630.0 nm airglow intensity variation using the collocated multi-wavelength photometer during same time interval is represented in Figure 5.1d. The measurement OI 630.0 nm airglow after the local F region moon set (∼21:00 IST) is shown in Figure 5.1d. The base of F layer height observed over dip equator, Thumba, is shown in Figure 5.1e that varies from 285 km at 20:00 IST to 200 km at mid-night. It is of interest to note that the bottom envelope of ESF plumes descends from 280 km at 20:00 IST to around 200 km at around 23:30

IST. Multiple plume structures are observed in RTI maps. The spectral widths of plumes observed during 20:00-21:00 IST are predominantly large (>90 m/s) indicating the plumes are in evolutionary phase. During 22:30 IST, plumes at higher altitude region are found to move predominantly upward (see Figure 5.1b) while the bottom side structures observed around 200 km move downward. The optical signatures corresponding to the bottom side structures observed at 22:35-22:45 IST (marked by blue window) reveal clearly that the structure is plasma blob. This is unambiguous as the layer height remains steady during this time and Doppler velocities inside the structure are predominantly downward. Similarly, the structure in the region around 250 km during 23:25-23:35 IST (marked by red window) is identified as plasma bubble. Since the downward movement of F layer cannot account for depleted OI 630.0 nm airglow intensity, the region is identified as plasma depletion. The spectral width corresponding to this structure is large (>90 m/s) indicating evolutionary phase of this structure. This could probably be due to a structure that got generated west of Gadanki at an earlier time and moved into the radar field-of-view.

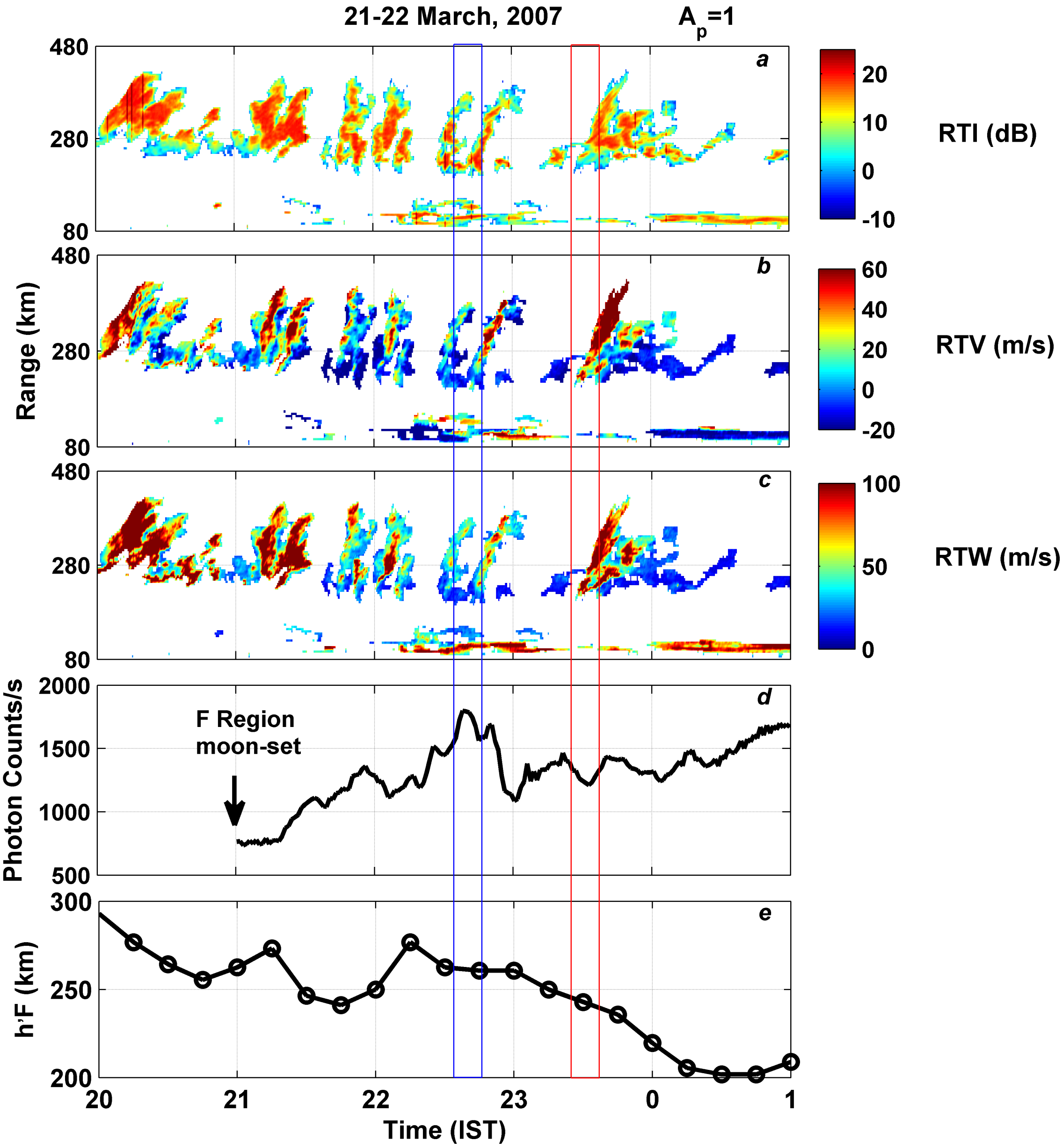

Figure 5.1: (a), (b) & (c) Range-Time-Intensity (RTI), Range-Time-Velocity (RTV) and Range-Time-Width (RTW) maps of ESF obtained using Indian VHF radar at Gadanki on 21-22 March, 2007. (d) The intensity variation of OI 630.0 nm airglow (in Photon Counts/s) measured using the multi-wavelength airglow photometer. (e) The base of the F layer height (h'F) variation over dip equator, Thumba. The blue and red rectangular boxes respectively represent the temporal window when plasma blob and bubble can be observed.

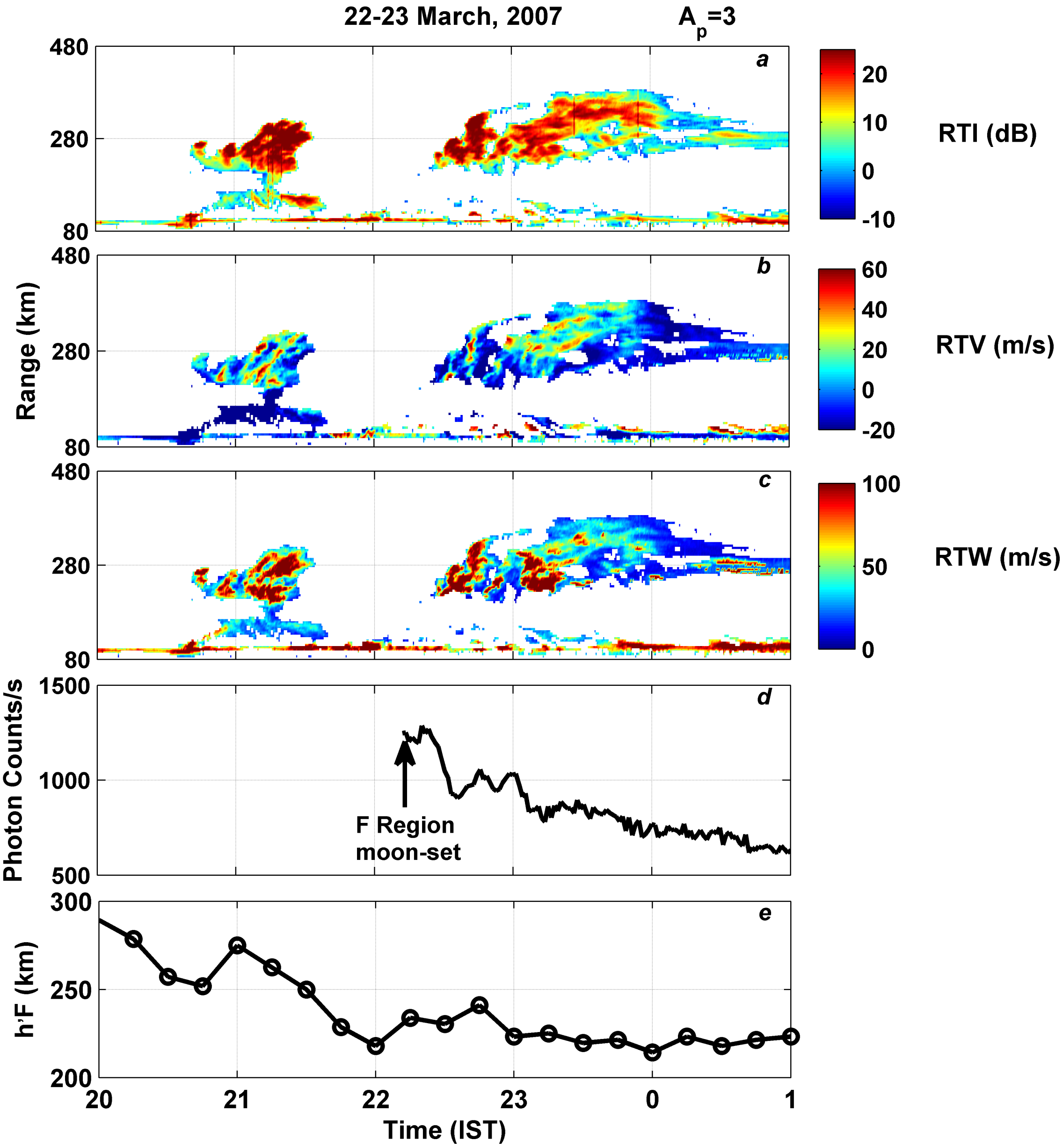

Figure 5.2: (a), (b) & (c) Range-Time-Intensity (RTI), Range-Time-Velocity (RTV) and Range-Time-Width (RTW) maps of ESF obtained using Indian VHF radar at Gadanki on 22-23 March, 2007. (d) The intensity variation of OI 630.0 nm airglow (in Photon Counts/s) measured using the multi-wavelength airglow photometer. (e) The base of the F layer height (h'F) variation over dip equator, Thumba.

Figure 5.2 depicts another simultaneous measurements of ESF events using VHF radar and OI 630.0 nm airglow photometer over Gadanki on 22-23 March, 2007 during geomagnetically quiet period (A_p=3). Figures 5.2a, 5.2b and 5.2c depict the RTI, RTV and RTW maps of plasma irregularities constructed from

VHF radar backscatter echo. The measurement OI 630.0 nm airglow emission intensities after the local F region moon set (∼22:10 IST) is shown in Figure 5.2d. The base height variation of ionospheric F layer over dip equator, Thumba, is plotted in Figure 5.2e. It is of interest to note that the radar structures are seen at ∼100, 140-150 and 220-300 km altitude regions between 20:30 to 22:00 IST. The structures at ∼100 km correspond to the usual E-region irregularities predominantly moving downward on most of the occasions except from 21:40 to 22:30 IST. The structures at 140-150 km are found only between 20:50 to 21:40 IST. Plasma irregularity channels which connect this region with E and F region irregularities are seen at around 21:15 IST (shown in Figure 5.2). The F region (220-300 km) irregular structures are found at unusually (even below the base height) lower altitude. The reasons for the generation of these unusual structures remain to be investigated further. ESF structures are not observed between 21:30 to around 22:30 IST. The depletion recorded at around 22:30 IST in OI 630.0 nm airglow cannot be conclusively associated with plasma depletion. This is also augmented by the fact that the base of the F layer moved upward during that time interval. Moreover, the Doppler velocities inside the structures reveal downward movement. Thus that depletion in OI 630.0 nm intensity is not associated with plasma bubble.

Figure 5.3 depicts the combined results of ESF events obtained on 26-27 April, 2006 by the three independent techniques during geomagnetically quiet period (A_p=3). The RTI, RTV and RTW maps obtained from VHF radar echoes are given in panels (a), (b) and (c). The color codes in them correspond to strength of return echoes in Figure 5.3a, line of sight Doppler velocities in Figure 5.3b and the spectral width in the unit of velocity in Figure 5.3c. A number of isolated plumes without having bottom side structures are observed on this night. The spectral width on this night is around 25 m/s which is significantly low as compared to those ESF observations on 21-22 March and 22-23 March, 2007 (shown in Figures 5.1 and 5.2). The vertical columnar intensity variations of OI 630.0 nm airglow emission corresponding to the same time interval are depicted in Figure 5.3d. Corresponding to isolated plume structures in Figure 5.3a, reductions or depletions in the OI 630.0 nm airglow intensities are noted. Depletions in airglow intensities are observed at ∼23:30, ∼24:00, ∼00:30, ∼01:00 and ∼01:30 IST. In addition to these, some other variations in OI 630.0 nm airglow emission are also observed before 23:30 IST and after 02:00 IST in Figure 5.3c which are not directly associated with ESF structures and will not be discussed further. The layer height variations over the dip equator (Thumba) which correspond to zonal electric field during nighttime are depicted in Figure 5.3e. The importance of these isolated structures obtained ∼23:30, ∼21:00, ∼01:00 and ∼01:30 IST will be discussed in the following section.

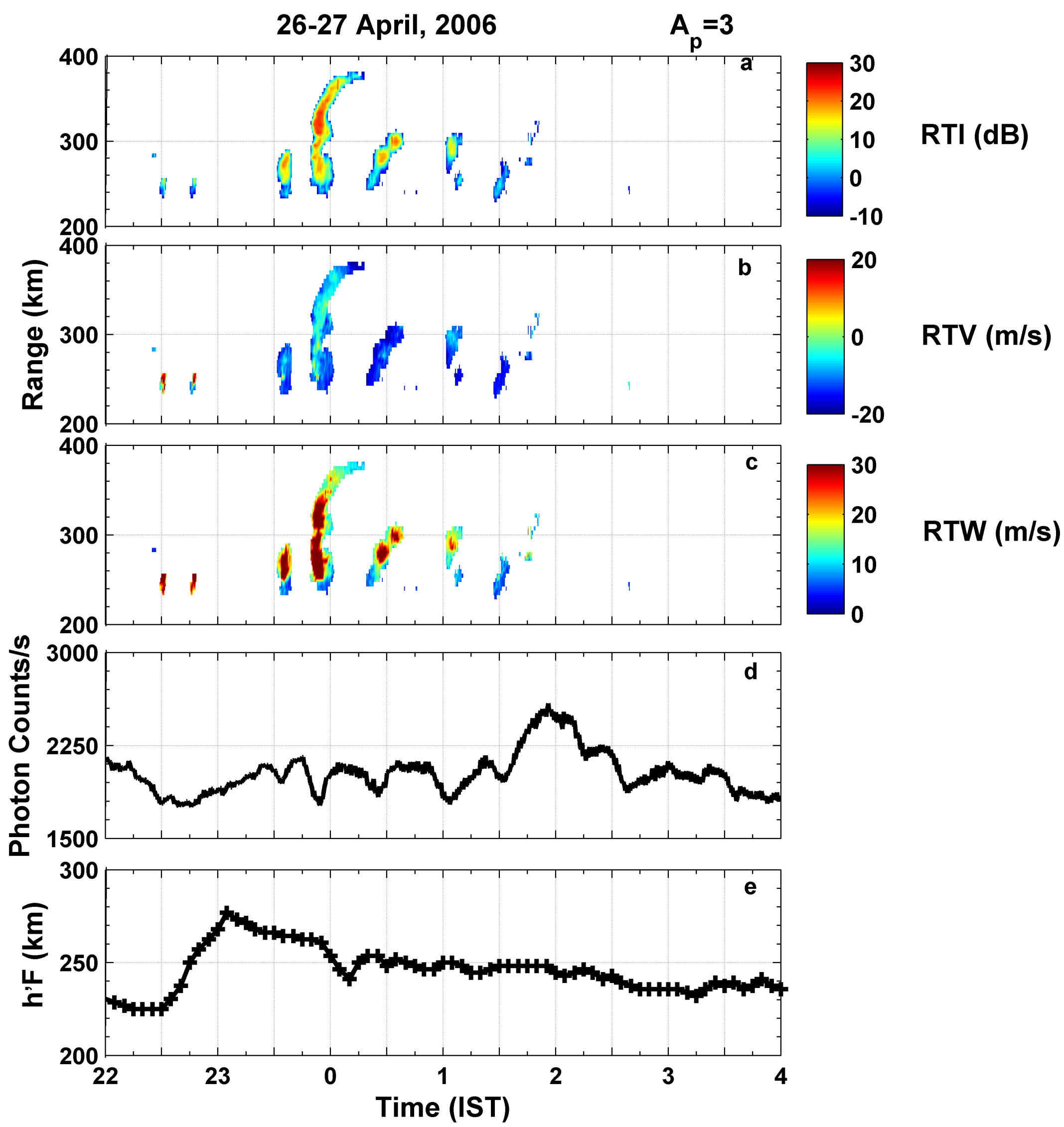

Figure 5.3: Equatorial Spread F (ESF) structures observed over Gadanki on 26-27 April 2006 as revealed by (a) Range-Time-Intensity (RTI) plot, (b) Range-Time- Velocity (RTV) plot, (c) Range-Time-Width (RTW) along with corresponding temporal variations in OI 630.0 nm airglow measurements and the base of the F layer over dip equator are shown in (d) and (e).

5.4 Discussion

It is well known that the production mechanism of OI 630.0 nm airglow during nighttime is due to dissociative recombination of O_2^+ ions with ambient electron (e^-). The O_2^+ ion react with e^- and produce $O(^1D)$ atom, an excited state of atomic oxygen. The excited $O(^1D)$ atom comes to ground state (O^3P) by radiating 630.0 nm airglow line. This reaction is favored at an altitude where sufficient O_2^+ ions and e^- are present. The peak altitude of this emission is around 250 km during nighttime. Therefore, the OI 630.0 nm intensity depends on the concentrations of both O_2^+ and e^- and the variation in the intensity is proportional to the fluctuation in the e^- density. As the both O_2^+ and e^- concentration are driven by the ionospheric conditions, the intensity of this redline emission is dependent on the ionospheric parameters.

Barbier [1959] established an empirical relation between the instantaneous intensity of OI 630.0 nightglow intensity to the ionospheric parameters h_pF_2 and f_oF_2 as

$$Q_{630.0nm} = A + B(f_oF_2)^2 e^{-\frac{h_pF_2-200}{40}} \tag{5.1}$$

Where, A and B are constants, h_pF_2 and f_oF_2 are peak height of the ionospheric F layer and critical frequency of the F_2 layer respectively. The above expression reveal that the airglow intensity and h_pF_2 are anti-correlated. The empirical relation given in equation 5.1 suggests that OI 630.0 airglow intensity increases or decreases depending on movement of the F layer downward or upward respectively. The movement of F layer can be determined by the temporal variation of either h_pF_2 or the base height of the F layer (h'F) as the altitude variation of the velocity is not significant during nighttime. As the variations of airglow intensity are investigated during ESF events in the present work, the height variations of h'F are used.

The effects of ESF plasma plumes and h'F variation on OI 630.0 nm airglow intensity have been investigated over Indian low latitude stations, Gadanki [*Sekar et al.,* 2004, 2008; *Chakrabarty,* 2007] extensively. These investigations report that the large scale temporal variations in OI 630.0 nm airglow intensity are governed by the F layer base height variation whereas, the smaller scale temporal variations in the intensity during magnetically quiet periods are due to ESF structures present within the airglow emission layer. The coordinated optical and radar measurement brought out the clear evidences of plasma blobs and bubbles where the airglow intensity shows enhancements and depletions respectively.

Similar to the earlier work, the OI 630.0 nm airglow intensity in present case shows smaller and larger scale variation (Figures 5.1). A hump like structure in OI 630.0 airglow intensity can be observed on 21-22 March, 2007 in between 21:15–22:15 IST when the base of the layer height (h'F) shows a valley type variation. In addition to that there is a steady decrease in base layer height after 23:00 IST and as a consequence the average level of airglow intensity increases monotonically. However, on many occasions, smaller scale variations are observed in airglow intensity whenever the plumes of irregularities enter in the airglow emission region. These depletions and enhancements in airglow intensity are due to plasma bubbles or blobs. The identification of plasma bubbles (marked by red window) and blobs (marked by blue window) are only substantiated by the optical measurements wherein the clear depletions and enhancements in OI 630.0 nm intensity are recorded whenever the ESF structures enter in the airglow region.

The numerical simulations by earlier workers [*Ossakow,* 1981; *Sekar,* 2003] suggest that depletion in seed perturbation in electron densities can grow into plasma bubble due to Rayleigh-Taylor instability mechanism whereas, the enhancement in the seed perturbation can form a plasma blob at lower altitude region [*Sekar et al.,* 1994]. Since these blobs are moving downward, plasma blobs at higher altitude cannot be easily formed. However, it was shown [*Sekar et al.,* 2001] by employing more than one mode as seed perturbation, the plasma blobs could be generated even beyond 350 km altitude region. Such blobs were also experimentally identified by the earlier research workers [*Sekar et al.,* 2004, 2008]. The generation of F region irregular structure below the base height observed on 22-23 March is somewhat intriguing. The echoes at 140-150 km altitude could not be classified as the well-known 150 km echoes [*Kudeki and Fawcett,* 1993; *Patra et al.,* 2008] as the characteristics (like necklace shape) are not observed in the present case. The fringe field associated with ESF [*Zalesak and Ossakow,* 1980; *Sekar et al.,* 1997;

Kherani et al., 2002] for the development of very large scale irregularities (a few hundred kms) in the F region can, in principle, connect the irregularities in F to E region. This process could probably explain the initial phase of the observation on 22-23 March, 2007.

The coordinated observations of the ESF events reveal that the plasma bubbles are highly turbulent in nature that indicates the evolutionary phase of these irregularities. These are generated during post-sunset hours and evolve in spatio-temporal domain depending on the ionospheric background conditions. As mentioned earlier, during mid-night hours, the plasma bubbles do not generally evolve. This non-evolutionary phase of plasma bubbles is known as "fossil bubble". These are the dead plumes and move with the background plasma drift. These can be mostly observed during post-midnight hours with larger scale sizes. The motion of these bubbles are predominantly downward and are less turbulent. The identification of these plasma bubbles is not easy with VHF radar as the radar can only probe 3 meter-scale sizes irregularities. However, on a few occasions, theses can be identified using coordinated radio and optical techniques. The simultaneous observations of VHF radar and optical airglow photmeter from Gadanki along with the ionosonde observation from dip equator, Thumba on 26-27 April, 2006 bring out the identification and characterization of fossil type plasma bubbles.

The strength of the radar backscattered echoes corresponding to the ESF structures till 00:30 IST on 27 April, 2006 can be observed to be relatively intense (shown in Figure 5.3a) and they remained either stationary or moved downward (shown in Figure 5.3b). The ESF structures began to weaken after 00:30 IST although the movements continued to be downward. The downward movement of these structures are evidenced both by Doppler velocities and from the location of the lower boundary of the structure compared to other structures. The variation of the base height of F region in the lowest panel also confirms the slow downward motion. The spectral widths corresponding to all the five structures are less than 25 m/s. These spectral widths are less compared to the corresponding width (>60 m/s) for well developed ESF structure (shown in Figures 5.1 and 5.2) indicating that the structures were less turbulent. This supports that these structures are mostly in the non–evolutionary stages.

The airglow intensity decreased corresponding to all these five structures. As mentioned earlier, this airglow intensity is directly proportional to electron density. Further, as these structures are isolated patches, depleted airglow intensities can be taken to be due to the presence of plasma depletion structures with respect to background. As mentioned earlier, that the variations in 630.0 nm airglow intensity not only depends on the electron density variations but also depends inversely on the F layer height variation. In order to ensure that the airglow intensity variations recorded corresponding to these ESF structures are essentially due to plasma depletions, the F-layer layer height variations (Figure 5.3e) are examined. The F-region height remained nearly stationary or was moving downward during these intervals. Downward motion of the F layer generally increases the 630.0 nm airglow intensity. Therefore, based on the airglow intensity variations, radar plots corresponding to these ESF structures and ionosonde observations, it can be inferred that these structures are "fossil bubbles" which were not moving upward as that of the conventional plasma bubble in developing phase.

It is important to understand how such fossil bubbles can maintain 3 meter-scale irregularities and remain "active". A close scrutiny of Figure 5.3 reveals that the irregularities are located mostly on the rising edge of the airglow depletions. As pointed out by *Woodman and La Hoz* [1976], a narrow field of view detector acts like a slit camera and and for a frozen-in structure moving east, the viewpoint is that of looking south along the earth's magnetic field lines. Thus, the active region is on the western edge of the fossil bubble. Such a region has a density gradient pointing westward. Therefore, the growth of 3 meter irregularities are favored only on the western edge of plasma bubbles. Under this condition, the plasma is susceptible to the neutral wind driven instability [*Kelley,* 1989] if the eastward wind exceeds the plasma drift, as it must be the case to sustain the F region dynamo. Thus the neutral wind driven instability is suggested to destabilize the fossil bubbles and make them active [*Sekar et al.,* 2007].

Chapter 6

Summary and Future Plan

- The variation in the average Na D_2 emission airglow intensity level from one night to another could not be explained based on measured Na atom and ozone concentrations. It is suggested that the quenching process due to the ambient gas affects the variations in branching ratio (α) and D_2/D_1 intensity ratio (R_D) leading to the observed differences in the Na airglow intensity level.

- Another simultaneous observation by Na lidar and Na airglow photometer brings out the critical role of ambient collisions in the Na airglow intensity. Correlation analysis between Na atom concentration and Na airglow intensity corresponding to D_2 emission line reveals that the correlation coefficient is maximum at an altitude that is about one scale height higher than the altitude of maximum Na concentration. Further, volume emission rate (V_{NaD_2}) calculations were carried out to account for the contribution from mesospheric ozone and temperature to the Na airglow emission process. This estimation of V_{NaD_2} reveals that the peak emission altitude does not match with altitude of maximum correlation coefficient. It is suggested that the altitude variation of the collisional quenching needs to be considered, on this occasion, to account for the observed Na airglow intensity variation. The measured mesospheric pressure supports this view.

  Systematic simultaneous measurements of neutral Na atoms and Na airglow intensity using Na resonance lidar and Na airglow photometer along with the satellite borne measurements of mesospheric ozone, temperature and pressure are planned in order to establish an empirical relationship between the Na airglow intensity and ambient mesospheric pressure.

The profiles of Na D_2/D_1 intensity ratio need to be measured by the photometers onboard sounding rockets to address the need for the altitude variation of collisional quenching.

- In order to identify the dominant modes of mesospheric gravity waves, Na airglow measurements were carried out in campaign modes during 2006-2009 over Mt. Abu and Gadanki using a narrow-band and narrow field-of-view Na airglow photometer. The power spectra indicate that 15-30 min periods, associated with the mesospheric gravity wave activities, are present in the Na airglow intensity variation over both Mt. Abu and Gadanki. The mesospheric temperatures and horizontal winds nearly over both the places reveal the occurrence of convective and dynamical instabilities within the Na airglow layer on a few occasions. The dominant periods, on those observational nights, associated with the gravity waves derived from Na airglow intensity variation, are found to be significantly small in comparison with the cases where those instabilities occurred much beyond Na airglow layer suggesting the breaking of gravity waves into smaller-scale sizes waves.

  The multi-wavelength airglow imager is being modified and will be used to derive the horizontal parameters (in two dimension) of atmospheric gravity waves. The vertical parameter of gravity waves can be estimated from profiles of neutral Na atoms measured using Na resonance lidar. Thus, the coordinated observations of Na lidar and airglow imager is useful to parameterize gravity waves in three dimensions.

- The secondary waves generated from the breaking of primary waves near mesopause region can reach thermosphere ionosphere system (TIS) and may act as seed perturbations to trigger equatorial spread F (ESF) irregularities. The coordinated observations of ESF events using thermospheric airglow photmeter and VHF radar can reveal several aspects of ESF. The differentiation between the plasma bubbles and blobs are carried out using OI

630.0 nm airglow intensity variations. The depletions and enhancements are recorded in the airglow intensity whenever the plasma bubbles and blobs are found within the airglow emitting layer. These post-sunset plasma irregularities are in evolutionary phase and are extremely turbulent. However, during mid-night hours these plasma irregularities no longer evolve and become less turbulent. An example of identifying "fossil bubbles" associated with ESF using coordinated measurements of VHF radar and airglow is obtained. Downward moving plume structures and corresponding depletions in OI 630.0 nm airglow intensity reveal that these structures are "fossil bubbles". The layer height variations support the conclusion that the recorded airglow intensity variations are only due to plasma density depletions. Analysis of the location of the 3 meter irregularity structures strongly suggests that these are due to neutral wind driven instability.

Attempts will be made to find out the favorable conditions under which gravity waves penetrate mesospause and reach TIS. Thus, systematic coordinated measurements are planned using mesospheric-thermospheric airglow imager and Na resonance lidar will lead to the understanding of vertical coupling between mesosphere and thermosphere-ionosphere.

Bibliography

1. Antonita, T. M., G. Ramkumar, K. K. Kumar, and V. Deepa; Meteor wind radar observations of gravity wave momentum fluxes and their forcing toward the Mesospheric Semiannual Oscillation, J. *Geophys. Res., 113,* D10115, doi: 10.1029/2007JD009089, 2008.

2. Argo, P. E. and Kelley, M. C.; Digital Ionosonde Observations During Equatorial Spread F, *J. Geophys. Res., 91,* 5539–5555, 1986.

3. Bageston, J. V., Wrasse, C. M., Gobbi, D., Takahashi, H., and Souza, P. B.; Observation of mesospheric gravity waves at Comandante Ferraz Antarctica Station (62∘ S), *Ann. Geophys., 27,* 2593–2598, 2009.

4. Barbier, D.; Recherches sur la raie 6300 de la luminescence atmospherique nocturne, *Ann. Geophys., 15,* 179–217, 1959.

5. Basu, S., Basu, Su., Aarons, J., McClure, J. P., and Cousins, M. D.; On the coexistence of kilometer- and meter-scale irregularities in the nighttime equatorial F region. *J. Geophys. Res., 83,* 4219–4226, 1978.

6. Bates, D. R., P. C. Ojha; Excitation of Na D-doublet of the nightglow, *Nature, 286,* 1980.

7. Bernard, R.; Das vorhansdensein von Natrium in der Atmosphaere auf Grund von interferometrischen Untersuchungen der D line in Abend und Nachthimmelslicht, *Z. Phys., 110,* 291–302, 1938a.

8. Bernard, R.; Etude interferentielle de la radiation janune 5893 Ao du ciel crepusculaire et preuve de la presence du sodium dans la haute atmosphere, *C. R. Acad. Sci. Paris, 206,* 928–930, 1938b.

9. Beer, T.; Atmospheric Waves, *ADAM HIGER LTD, Great Britain,* 1974.

10. Bhavani Kumar, Y., D. Narayana Rao, M. Sundara Murthy, M. Krishnaiah; Lidar system for mesospheric sodium measurements, *J. Opt. Engg*, *46*, 8, doi:10.1117/1.2767271, 2007a.

11. Bhavani Kumar, Y., P. V. Prasanth, D. Narayana Rao, M. Sundara Murthy, M. Krishnaiah; The first lidar observations of the nighttime sodium layer at low latitudes Gadanki (13.5°N, 79.2°E), India, *Earth, Planets and Space*, *59*, 601–611, 2007b.

12. Blamont, J. E., T. M. Donahue, and V. R. Stull; Sodium twilight airglow, 1955–1957. I, A*nn. Geophys., 14,* 253, 1958.

13. Blamont, J. E., M. L. Chanin, and G. Megie; Vertical distribution and temperature of the nighttime atmospheric sodium layer obtained by laser backscatter, *Ann. Geophys. 28,* 83–838, 1972.

14. Bowman, M. R., A. J. Gibson, and M. C. W. Sandford; Atmospheric sodium measurements by a tuned Laser Radar, *Nature, 221,* 456–457, 1969.

15. Bullock, W. R., and D. M. Hunten; Vertical distribution of sodium in the upper atmosphere, *Can. J. Phys., 39,* 976-982, 1961.

16. Cabannes, J., J. Dufay, and J. Gauzit; Sur la presence du sodium dans le haute atmosphere, *C. R. Acad. Sci. Paris, 206,* 870–872, 1938.

17. Chakrabarty, D., R. Sekar, R. Narayanan, T. K. Pant, and K. Niranjan; Thermospheric gravity wave modes over low and equatorial latitudes during daytime, *J. Geophys. Res., 109,* A12309, doi: 10.1029/2003JA010169, 2004.

18. Chakrabarty, D., Sekar, R., Narayanan, R., Devasia, C. V., Pathan, B. M.; Evidence for the interplanetary electric field effect on the OI 630.0 nm airglow over low latitude, *J. Geophys. Res., 110,* A11301, doi:10.1029/2005JA011221, 2005.

19. Chakrabarty, D., Sekar, R., Narayanan, R., Patra, A. K., Devasia, C. V.; Effect of interplanetary electric field on the development of an spread F event, *J. Geophys. Res., 111,* A12316, doi:10.1029/2006JA011884, 2006.

20. Chakrabarty, D.; Investigations on the F region of the ionosphere over low latitude using optical, radio and simulation techniques, *Ph. D. Thesis, Mohanlal Sukhadia University, Udaipur, India,* 2007.

21. Chamberlain, J. W., D. M. Hunten, and J. E. Mack; Resonance scattering by atmospheric sodium, 4. Abundance of sodium in twilight, *J. Atmos. Terr. Phys., 12,* 153-165, 1958.

22. Chamberlain, J. W.; Physics of the Aurora and Airglow, *AGU, Washington D. C.,* 1995.

23. Chapman, S.; Notes on atmospheric sodium, *J. Astrophys.*, *90*, 309–316, 1939.

24. Chu, Y. H., C. L. Su, M. F. Larsen, and C. K. Chao; First measurements of neutral wind and turbulence in the mesosphere and lower thermosphere over Taiwan with a chemical release experiment, *J. Geophys. Res., 112,* A02301, 10.1029/2005JA011560, 2007.

25. Clemesha, B. R., V. W. J. H. Kisrchhof, D. M. Simonich; Simultaneous Observations of the Na 5893-*Å* Nightglow and the Distribution of Sodium Atoms in the Mesosphere, *J. Geophys. Res.*, *83*, 2499–2503, 1978.

26. Clemesha, B. R., V. W. J. H., Kirchhoff, D. M., Kirchhoff, H. Takahashi, and P.P. Batista; Simultaneous observations of sodium density and the NaD, OH(8,3), and OI 5577 *Å* nightglow emissions, *J. Geophys. Res, 84,* 6477–6482, 1979.

27. Clemesha, B. R., D. M. Simonich, H. Takahashi, S. M. L. Melo; A simultaneous measurement of the vertical profiles of sodium nightglow and atomic sodium density in the upper atmosphere, *Geophys. Res. Lett.*, *20*, 1347–1350, 1993.

28. Clemesha, B. R., D. M. Simonich, H. Takahashi, S. M. L. Melo, and J. M. C. Plane; Experimental evidence for photochemical control of the atmospheric sodium layer, *J. Geophys. Res.*, *100*(D9), 18,909–18,916, 1995.

29. Clemesha, B. R., P. P. Batista, and D. M. Simonich; Formation of sporadic sodium layers, *J. Geophys. Res., 101*(A9), 19701–19706, 1996.

30. Clemesha B. R., D. M. Simonich, P. P. Batista, T. Vondrak, J. M. C. Plane; Negligible long-term temperature trend in the upper atmosphere at 23° S, *J. Geophys. Res., 109,* D05302, doi:10.1029/2003JD004243, 2004.

31. Daire, S. E., John M. C. Plane, Stuart D. Gamblin, Pavel Soldn, Edmond P. F. Lee, Timothy G. Wright; A theoretical study of the ligand-exchange reactions of Na^+X complexes ($X=O,O_2,N_2,CO_2$ and H_2O): implications for the upper atmosphere, *J. Atmos. Sol. Terr. Phys., 64,* 863–870, 2002.

32. Dejardin, G.; Presence possible de certaines raies de latome neuter de sodium dans le spectre du ciel nocturne, *C. R. Acad. Sci. Paris, 206,* 930–933, 1938.

33. Fagundes, P. R., Takahashi, H., Sahai, Y., Gobbi, D.; Observations of gravity waves from multispectral mesospheric nightglow emissions observed at 23∘ S, *J. Atmos. Terr. Phys., 57,* 395-405, 1995.

34. Fritts, D. C.; Gravity wave saturation in the middle atmosphere - A review of theory and observations, *Rev. Geophys., 22,* 275-308, 1984.

35. Fritts, D. C., J. R. Isler, and O. Andreassen; Gravity wave breaking in two and three dimensions: 1. Three-dimensional evolution and instability structure, *J. Geophys. Res., 99,* 8109–8123, 1994.

36. Fritts, D. C., J. R. Isler, J. H. Hecht, R. L. Walterscheid, Andreassen; Wave breaking signatures in sodium densities and OH nightglow 2. Simulation of wave and instability structures, *J. Geophys. Res.*, *102*(D6), 6669-6684, 10.1029/96JD01902, 1997.

37. Fritts D. C., and Alexander, M. J.; Gravity wave dynamics and effects in the middle atmosphere, *Rev. Geophys., 41* (1), 1003, doi: 10.1029/2001RG000106, 2003.

38. Fukao, S., Y. Ozawa, T. Yokoyama, M. Yamamoto, and R. T. Tsunoda; First observations of the spatial structure of F region 3-m-scale field-aligned irregularities with the Equatorial Atmosphere Radar in Indonesia, *J. Geophys. Res., 109,* A02304, 10.1029/2003JA010096, 2004.

39. Fukao, S., Yokoyama, T., Yamamoto, M., Maruyama, T., and Saito, S.; Onset of F-region plasma plumes observed with Equatorial Atmosphere Radar in Indonesia, *Proceedings of XXVIII URSI General Assembly, New Delhi,* 2005.

40. Fuller-Rowell, T. J.; The Dynamics of the Lower Thermosphere, *Geophysical Monograph, 87,* 23–36, American Geophysical Union, 1995.

41. Gardner, C. S., D.C. Senft, and K.H. Kwon; Lidar observations of a substantial sodium depletion in the summertime Arctic mesosphere, *Nature, 332,* 142–144, 1988.

42. Gardner C. S.; Sodium resonance fluorescence lidar applications in atmospheric science and astronomy, *Proc. IEEE 77*(3), 408-418, 1989.

43. Geller, M. A., H. Tanaka, and D.C. Fritts; Production of turbulence in the vicinity of critical levels for internal gravity waves, *J. Atmos. Sci., 32,* 2125, 1975.

44. Gibson, A. J., and M. C. W. Sandford; The seasonal variation of the night time sodium layer, *J. Atmos. Terr. Phys., 33,* 1675–1684, 1971.

45. Gibson, A. J., and M. C. W. Sandford; Daytime laser radar measurements of the atmospheric sodium layer, *Nature, 239,* 509–511, 1972.

46. Gibson, A. J., L. Thomas and S. K. Bhattachacharyya; Laser observations of the ground-state hyperfine structure of sodium and of temperatures in the upper atmosphere, *Nature 281,* 131–132, doi: 10.1038/281131a0, 1979.

47. Griffin, J., D. R. Worsnop, R. C. Brown, C. E. Kolb, and D. R. Herschbach, Chemical kinetics of the NaO(A $^2\Sigma^+$) + O(^{3}P) reaction, *J. Phys. Chem. A, 105*(9), 1643–1648, 2001.

48. Goldberg, R. A., A. C. Aikin, and B. V. Krishna Murthy; Ion Composition and Drift Observations in the Nighttime Equatorial Ionosphere, *J. Geophys. Res., 79*(16), 2473–2477, 1974.

49. Gossard, E. E., and W. H. Hooke; Waves in the Atmosphere, Atmospheric Infrasound and Gravity Waves-Their Generation and Propagation, *Elsevier Sci., New York,* 456, 1975.

50. Guharay, A.; Investigation of Mesospheric variability with the help of Airglow Emissions, *Ph. D. Thesis, Kumaun University, Nainital, India,* 2009.

51. Gurubaran, S., and R. Rajaram; Long-term variability in the mesospheric tidal winds observed by MF Radar over Tirunelveli (8.7N, 77.8E), *Geophys. Res. Lett., 26*(8), 1113–1116, 1999.

52. Gurubaran, S., and R. Rajaram; Mean winds, tides, and gravity waves during the westward phase of the mesopause semiannual oscillation (MSAO), *J. Geophys. Res., 106*(D23), 31817—31824, 2001.

53. Hargreaves, J. K.; The solar-terrestrial environment, *Cambridge University Press,* 1995.

54. Hecht, J. H., Walterscheid, R. L., Fritts, D. C., Isler, J. R., Senft, D. C., Gardner, C. S., Franke, S. J.; Wave breaking signatures in OH airglow and sodium densities and temperatures 1. Airglow imaging, Na lidar, and MF radar observations, *J. Geophys. Res.*, *102*(D6), 6655-6668, 10.1029/96JD02619, 1997.

55. Hecht, J. H., S. Collins, C. Kruschwitz, M. C. Kelley, R. G. Roble, and R. L. Walterscheid; The Excitation of the Na Airglow from Coqui Dos Rocket and Ground-Based Observations, *Geophys. Res. Lett.*, *27*(4), 453–456, 2000a.

56. Hecht, J. H., C. Fricke-Begemann, R. L. Walterscheid, and J. Hffner; Observations of the breakdown of an atmospheric gravity wave near the cold summer mesopause at 54N, *Geophys. Res. Lett., 27*(6), 879-882, 2000b.

57. Hecht, J. H.; Instability layers and airglow imaging, *Rev. Geophys., 42,* RG1001, doi:10.1029/2003RG000131, 2004.

58. Hecht, J. H., A. Z. Liu, R. L. Walterscheid, and R. J. Rudy; Maui Mesosphere and Lower Thermosphere (Maui MALT) observations of the evolution of

Kelvin-Helmholtz billows formed near 86 km altitude, *J. Geophys. Res., 110,* D09S10, doi:10.1029/2003JD003908, 2005.

59. Herschbach, D. R., C. E. Kolb, D. R. Worsnop, and X. Shi; Excitation mechanism of the mesospheric sodium nightglow, *Nature*, *56*, 414–416, 1992.

60. Hickey, M. P., and J. M. C. Plane; A chemical-dynamical model of wavedriven sodium fluctuations, *Geophys. Res. Lett., 22,* 2861–2864, 1995.

61. Higashikawa, A., Nakamura, T., Tsuda, T.; Seasonal variation of gravity waves observed with an OH CCD imager at Shigaraki (35° N,136° E), Japan, *Adv. Space Res., 24,* 561–564, 1999.

62. Hines, C. O.; Internal atmospheric gravity waves at ionospheric heights, *Can. J. Phys.*, *38*, 1441–1481, 1960.

63. Hines, C. O.; Internal atmospheric gravity waves at ionospheric heights, *Can. J. Phys.*, *42,* 1425–1427, 1964.

64. Hines, C. O.; The Upper Atmosphere in Motion, *Am. Geophys. Union, Washington, DC,* 1974.

65. Hines, C. O., and D. W. Tarasick; On the Nonlinear Response of Airglow to Atmospheric Gravity Waves, *J. Geophys. Res., 98*(A11), 19127–19131, 1993.

66. Hodges, R. R., Jr.; Eddy diffusion coefficients due to instabilities in internal gravity waves, *J. Geophys. Res., 74,* 4087, 1969.

67. Hunten, D. M.; The Airglow and the Aurora, *Pergamon Press, London,* 114–121, 1967.

68. Iyer, K. N., M. N. Jivani, B. M. Pathan, S. Sharma, H. Chandra and M. A. Abdu; Equatorial spread F: Statistical comparison between ionosonde and scintillation observations and longitude dependence, *Adv. Space Res., 31,* 735–740, 2003.

69. Joo, S., D. R. Worsnop, C. E. Kolb, S. K. Kim, and D. R. Herschbach; Observation of the A $^2\Sigma^+ \leftarrow$ X $^2\Pi$ electronic transition of NaO, *J. Phys. Chem. A*, *103*, 3193–3199, 1999.

70. Kane, T. J., and C. S. Gardner; Lidar observations of the meteoric deposition of mesospheric metals, *Science, 259,* 1297–1300, doi: 10.1126/science.259.5099.1297, 1993.

71. Kelley, M., M. Larsen, C. LaHoz, and J. McClure; Gravity Wave Initiation of Equatorial Spread F: A Case Study, *J. Geophys. Res., 86*(A11), 9087–9100, 1981.

72. Kelley, M. C.; Equatorial spread F: recent results and outstanding problem, *J. Atmos. Sol. Terr. Phys., 47,* 745–752, 1985.

73. Kelley, M., et al.; The Condor Equatorial Spread F Campaign: Overview and Results of the Large-Scale Measurements, *J. Geophys. Res., 91*(A5), 5487–5503, 1986.

74. Kelley, M. C.; The Earths Ionosphere: Plasma physics and electrodynamics, *International Geophysics Series, 96, Academic Press*, 2009.

75. Killeen, T. L., and Johnson, R. M.; Upper atmospheric waves, turbulence and winds: Importance for mesospheric and thermospheric studies, *Rev. Geophys.*, 33, 737–743, 1995.

76. Kirchhoff, V.W.J.H., B.R. Clemesha, and D.M. Simonich; Average Nocturnal and Seasonal Variations of Sodium Nightglow at 23° S, 46° W, *Planet. Space Sci., 29,* 765–766, 1981.

77. Kirchhoff, V.W.J.H., and B.R. Clemesha; Atmospheric sodium measurements at 23°S, *J. Atmos. Terr. Phys., 35,* 1493–1498, 1973.

78. Kirchhoff, V. W. J. H., B. R. Clemesha, and D. M. Simonich; Sodium Nightglow Measurements and Implications on the Sodium Photochemistry, *J. Geophys. Res., 84*(A4), 1323–1327, 1979.

79. Kirchhoff, V. W. J. H., and B. R. Clemesha; The atmospheric neutral sodium layer, 2. Diurnal variations, *J. Geophys. Res., 88,* 442–450, 1983.

80. Kherani E. A., R. Raghavarao, R. Sekar; Equatorial rising structure in nighttime upper E-region: a manifestation of electrodynamical coupling of

spread F, *J. Atmos. Sol. Terr. Phys., 64,* 1505–1510, 10.1016/S1364-6826(02)00087-1, 2002.

81. Kishore Kumar, G., M. Venkat Ratnam, A. K. Patra, S. Vijaya Bhaskara Rao, and J. Russell; Mean thermal structure of the low-latitude middle atmosphere studied using Gadanki Rayleigh lidar, Rocket, and SABER/TIMED observations, *J. Geophys. Res.*, *113*, D23106, doi:10.1029/2008JD010511, 2008.

82. Koopmans, L. H.; The Spectral Analysis of Time Series, *Prob. Math. Stat. Ser.*, vol. 22, Elsevier, New York, 1974.

83. Krall, J., J. D. Huba, S. L. Ossakow, and G. Joyce; Why do equatorial ionospheric bubbles stop rising?, *Geophys. Res. Lett., 37,* L09105, doi: 10.1029/2010GL043128, 2010.

84. Krishna Murthy, B.; Middle atmosphere-upper atmosphere coupling, *Proc. Ind. Natl. Sc. Acad., 64 A, 3,* 303–313, 1998.

85. Krishna Murthy, B. S. P. Perov and M. N. Sasi; Diurnal and semi-diurnal tides in the equatorial middle atmosphere, *J. Atmos. Terr. Phys., 54,* 881–891, 1992.

86. Kudeki, E., and C. D. Fawcett; High resolution observations of 150 km echoes at Jicamarca, *Geophys. Res. Lett., 20,* 1987, 1993.

87. Kumar, K. K., V. Deepa, T. M. Antonita, and G. Ramkumar; Meteor radar observations of short-term tidal variabilities in the low-latitude mesosphere-lower thermosphere: Evidence for nonlinear wave-wave interactions, *J. Geophys. Res., 113,* D16108, doi: 10.1029/2007JD009610, 2008.

88. Lindzen, R. S.; Turbulence and stress due to gravity wave and tidal breakdown, *J. Geophys. Res., 86,* 9707–9714, 1981.

89. Li , F., A. Z. Liu, G. R. Swenson, J. H. Hecht, and W. A. Robinson; Observations of gravity wave breakdown into ripples associated with dynami-

cal instabilities, *J. Geophys. Res., 110,* D09S11, doi:10.1029/2004JD004849, 2005.

90. Liu, H. L., P. B. Hays, and R. G. Roble; A numerical study of gravity wave breaking and impacts on turbulence and mean state, *J. Atmos. Sci., 56,* 2152–2177, 1999.

91. Mason, B.; Handbook of Elemental Abundances in Meteorites, *Gordon and Breach, New York,* 1971.

92. Medeiros A. F., Taylor, M. J., Takahashi, H., Batista, P. P., Gobbi, D.; An investigation of gravity wave activity in the low-latitude upper mesosphere: Propagation direction and wind filtering, *J. Geophys. Res., 108* (D14), 4411, doi: 10.1029/2002JD002593, 2003.

93. Meinel, A. B.; OH emission bands in the spectrum of the night sky. I, *Astrophysical Journal, 111,* 555–564, 1950.

94. Meriwether, J. W., J. L. Mirick, M. A. Biondi, F. A. Herrero, and C. O. Fesen; Evidence for orographic wave heating in the equatorial thermosphere at solar maximum, *Geophys. Res. Lett., 23*(16), 2177–2180, 1996.

95. Molina, A.; Sodium Nightglow and Gravity Waves, J. *Atmos. Sc., 40,* 2444–2450, 1983.

96. Mukherjee, G. K.; The signature of short period gravity waves imaged in OI 557.7 nm and near infrared OH nightglow emissions over Panhala, *J. Atmos. Sol. Terr. Phys., 65,* 1329–1335, 2003.

97. Nakamura T., Aono, T., Tsuda, T., Admiranto, A. G., E. Achmad, E., Suranto; Mesospheric gravity waves over a tropical convective region observed by OH airglow imaging in Indonesia, *Geophys. Res. Lett., 30* (17), 1882, doi: 10.1029/2003GL017619, 2003.

98. Nakamura, T., T. Fukushima, 1, T. Tsuda, C.-Y. She, B.P. Williams, D. Krueger and W. Lyons; Simultaneous observation of dual-site airglow imagers and a sodium temperature-wind lidar, and effect of atmospheric sta-

bility on the airglow structure, *Adv. Space Res.*, *35,* 11, 1957–1963, doi: 10.1016/j.asr.2005.05.102, 2005.

99. Narayanan, V. L., S. Gurubaran, and K. Emperumal; A case study of a mesospheric bore event observed with an all-sky airglow imager at Tirunelveli (8.7°N), *J. Geophys. Res., 114,* D08114, doi: 10.1029/2008JD010602, 2009.

100. Narayanan, V. L., S. Gurubaran, and K. Emperumal; Airglow imaging observations of small-scale structures driven by convective instability in the upper mesosphere over Tirunelveli (8.7°N), *J. Geophys. Res., 115,* D19119, doi: 10.1029/2009JD012937, 2010.

101. Narcisi, R. S., and A. D. Bailey; Mass Spectrometric Measurements of Positive Ions at Altitudes from 64 to 112 Kilometers, *J. Geophys. Res., 70*(15), 3687–3700, 1965.

102. Nicolls, M. J., and M. C. Kelley; Strong evidence for gravity wave seeding of an ionospheric plasma instability, *Geophys. Res. Lett., 32,* L05108, doi: 10.1029/2004GL020737, 2005.

     item Nielsen, K., Taylor, M. J., Hibbins, R. E., Jarvis, M. J.; Climatology of short-period mesospheric gravity waves over Halley, Antarctica (76° S, 27° W), *J. Atmos. Sol-Terr. Phys., 71,* 991–1000, doi:10.1016/j.jastp.2009.04.005, 2009.

103. Orlanski, I., and K. Bryan; Formation of the Thermocline Step Structure by Large-Amplitude Internal Gravity Waves, *J. Geophys. Res., 74*(28), 6975–6983, 1969.

104. Ossakow, S. L.; Spread F theories: A review, *J. Atmos. Terr. Phys., 43,* 437–452, 1981.

105. Pant, T. K., D. Tiwari, C. Vineeth, S. V. Thampi, S. Sridharan, C. V. Devasia, R. Sridharan, S. Gurubaran, and R. Sekar; Investigation on the mesopause energetics and its possible implications on the equatorial MLTI processes through coordinated daytime airglow and radar measurements, *Geophys. Res. Lett., 34,* L15102, doi: 10.1029/2007GL030193, 2007.

106. Pallamraju, D.; Studies of Daytime Upper Atmospheric Phenomena using Ground-based Optical Techniques, *Ph. D. Thesis, The Devi Ahilya Vishwa Vidyalaya of Indore, Indore, India,* 1996.

107. Pallamraju, D., U. Das, and S. Chakrabarti; Short and long-timescale thermospheric variability as observed from OI 630.0 nm dayglow emissions from low latitudes, *J. Geophys. Res., 115,* A06312, doi: 10.1029/2009JA015042, 2010.

108. Patra, A., V. Anandan, P. Rao, and A. Jain; First observations of equatorial spread F from Indian MST radar, *Radio Sci., 30*(4), 1159–1165, 1995.

109. Patra, A. K., T. Yokoyama, Y. Otsuka, and M. Yamamoto; Daytime 150-km echoes observed with the Equatorial Atmosphere Radar in Indonesia: First results, *Geophys. Res. Lett., 35,* L06101, doi:10.1029/2007GL033130, 2008.

110. Pautet P.-D., Taylor, M. J., Liu, A. Z., Swenson, G. R.; Climatology of short-period gravity waves observed over northern Australia during the Darwin Area Wave Experiment (DAWEX) and their dominant source regions, *J. Geophys. Res., 110,* D03S90, doi: 10.1029/2004JD004954, 2005.

111. Plane, John M. C. and David Husain; Determination of the absolute rate constant for the reaction O + NaO $\rightarrow$ Na + O_2 by time-resolved atomic chemiluminescence at λ= 589 nm [Na(3 ^2P_J) Na(3 $^2S_{1/2}$)+hν], *J. Chem. Soc., Faraday Trans. 2, 82*, 2047–2052, doi: 10.1039/F29868202047, 1986.

112. Plane, J. M. C., C. F. Nien, M. R. Allen, M. Helmer; A kinetic Investigation of the Reactions Na + O_3 and NaO + O_3 over the Temperature Range 207-377 K, *J. Phys. Chem.*, *97*, 4459–4467, 1993.

113. Plane, J. M. C., C. S. Gardner, J. Yu, C. Y. She, R. R. Garcia, and H. C. Pumphrey; Mesospheric Na Layer at 40^circ N : modeling and observations, *J. Geophys. Res., 104*(D3), 3773–3788, 1999a.

114. Plane, J. M. C., R. M. Cox, R. J., Rollason; Metallic Layers in the Mesopause and Lower Thermosphere Region, *Adv. Space Res., 24,* 1559–1570, 1999b.

115. Plane, J. M. C.; Meteors in the Earths Atmosphere: Murad, E., Williams, I. P., Eds., *Cambridge University Press: Cambridge,* 2002.

116. Plane, J. M. C.; MESOSPHERE/Metal Layers, *Encyclopedia of Atmospheric Sciences,* 1265–1271, 2003a.

117. Plane, J. M. C.; Atmospheric Chemistry of Meteoric Metals, *Chem. Rev.*, *103*, 4963–4984, 2003b.

118. Plane, J. M. C.; A time resolved model of the mesospheric Na layer: constraints on the meteor input function, *Atmos. Chem. Phys.*, *4*, 627–638, 2004.

119. Plane, J. M. C., A. Saiz-Lopez, B. J. Allan, S. H. Ashworth, P. Jenniskens; Variability of the mesospheric nightglow during the 2002 Leonid storms, *Adv. Space Res.*, *39*, 562–566, 2007.

120. Pfrommer, T., P. Hickson, and C.-Y. She; A large-aperture sodium fluorescence lidar with very high resolution for mesopause dynamics and adaptive optics studies, *Geophys. Res. Lett., 36,* L15831, doi: 10.1029/2009GL038802, 2009.

121. Prakash, S., S. Pal, H. Chandra; In-situ studies of equatorial spread-F over SHARsteep gradients in the bottomside F-region and transitional wavelength results, *J. Atmos. Terr. Phys, 53,* 977–986, 1991.

122. Raghavarao, R. J.N Desai, B.G Anandarao, R Narayanan, R Sekar, Ranjan Gupta, V. V. Babu and V Sudhakar; Evidence for a large scale electric field gradient at the onset of equatorial spread-F, *J. Atmos. Terr. Phys, 46,* 355–357, 359–362, 1984.

123. Raghavarao, R., S. P. Gupta, R. Sekar, R. Narayanan, J. N. Desai, R. Sridharan, V. V. Babu and, V. Sudhakar; In situ measurements of winds, electric fields and electron densities at the onset of equatorial spread-F, *J. Atmos. Terr. Phys, 49,* 485–492, 1987.

124. Raghavarao, R., R. Sekar and R. Suhasini; Nonlinear numerical simulation of equatorial spread-F Effects of winds and electric fields, Adv. Space Res., 12, 227–230, 1992.

125. Rajaram, R. and Gurubaran, S.; Seasonal variabilities of low-latitude mesospheric winds, *Ann. Geophys., 16,* 197-204, doi: 10.1007/s00585-998-0197-4, 1998.

126. Ramkumar, G., et al.; Seasonal variation of gravity waves in the equatorial middle atmosphere: Results from ISROs Middle Atmospheric Dynamics (MIDAS) program, *Ann. Geophys., 24,* 2471–2480, 2006.

127. Rao, P. B., Jain, A. R., Kishore, P., Balmuralidhar, P., Damle, S. H., and Vishwanathan, G.; Indian MST radar, System description and sample vector wind measurements in ST mode, *Radio Sci., 30,* 1125, 1995.

128. Reid, I. M., and Woithe, J. M.; Three-field photometer observations of short-period gravity wave intrinsic parameters in the 80 to 100 km height region, *J. Geophys. Res., 110,* D21108, doi: 10.1029/2004JD005427, 2005.

129. Richardson, L. F.; The supply of energy from and to atmospheric eddies, *Proc. R. Soc. London A, 97,* 354–373, 1920.

130. Rowlett, J. R., C. S. Gardner, E. S. Richter, and C. F. Sechrist, Jr.; Lidar observations of wavelike structure in the atmospheric sodium layer, *Geophys. Res. Lett., 5,* 683–686, 1978.

131. Rottger, J.; Gravity waves seeding ionospheric irregularities, *Nature, 296,* 111–112, 1982.

132. Sandford, M.C.W., and A. J. Gibson; Laser radar measurements of the atmospheric sodium layer, *J. Atmos. Terr. Phys., 32,* 1423–1430, 1970.

133. Sastri, J. H.; Post-midnight onset of spread F at Kodaikanal during the June solstice of solar minimum, *Ann. Geophys., 17,* 1111–1115, 1999.

134. Sarkhel, S., R. Sekar, D. Chakrabarty, R. Narayanan, and S. Sridharan; Simultaneous Na airglow and lidar measurements over India: a case study, *J. Geophys. Res.*, *114*, A10317, doi:10.1029/2009JA014379, 2009.

135. Sarkhel S., R. Sekar, D. Chakrabarty, and S. Sridharan; A Case Study on the Possible Altitude-Dependent Effects of Collisions on Sodium Airglow Emission, *J. Geophys. Res., 115,* A10306, doi: 10.1029/2010JA015251, 2010.

136. Schulz, M. and Stattegger, K.; Spectrum: Spectral Analysis of unevenly spaced paleoclimatic time series, *Computers & Geosciences*, 23, 929–945, 1997.

137. Sekar, R.; Plasma Instabilities and the Dynamics of the Equatorial F-region, *Ph. D. Thesis, Gujarat University, Ahmedabad, India,* 1990.

138. Sekar, R., S. Gurubaran, and R. Sridharan; All sky imaging Fabry-Perot spectrometer for optical investigation of the upper atmosphere, *Indian J. Radio Space Phys., 22,* 197–204, 1993.

139. Sekar, R., R. Suhasini, and R. Raghavarao, Effects of vertical winds and electric fields in the nonlinear evolution of equatorial spread F, *J. Geophys. Res., 99,* 2205–2213, 1994.

140. Sekar, R., R. Suhasini, and R. Raghavarao; Evolution of plasma bubbles in the equatorial F region with different seeding conditions, *Geophys. Res. Lett., 22(8),* 885–888, 1995.

141. Sekar, R., R. Sridharan, and R. Raghavarao; Equatorial plasma bubble evolution and its role in the generation of irregularities in the lower F region, *J. Geophys. Res., 102(A9)*, 20063–20067, 1997.

142. Sekar, R., Kelley, M. C.; On the combined effects of vertical shear and zonal electric field patterns on nonlinear equatorial spread F evolution, *J. Geophys. Res.*, *103,* 20735, 1998.

143. Sekar, R., E. A. Kherani, P. B. Rao, and A. K. Patra; Interaction of two long-wavelength modes in the nonlinear numerical simulation model of equatorial

spread F, *J. Geophys. Res., 106,* 24,76524,775, doi:10.1029/2000JA000361, 2001.

144. Sekar, R.; Plasma instabilities and their simulations in the equatorial F region - Recent results, *Space Sci. Rev. 107,* 251, 2003.

145. Sekar, R., D. Chakrabarty, R. Narayanan, S. Sripathi, A. K. Patra and K. S. V. Subbarao; Characterization of VHF radar observations associated with equatorial Spread F by narrow-band optical measurements, *Ann. Geophys.*, *22*, 3129–3136, 2004.

146. Sekar, R., D. Chakrabarty, S. Sarkhel, A. K. Patra, C. V. Devasia, and M. C. Kelley; Identification of active fossil bubbles based on coordinated VHF radar and airglow measurements, *Ann. Geophys., 25,* 2099–2102, 2007.

147. Sekar, R., Chakrabarty, D.; Impact of space weather events on the coupling of ionosphere and thermosphere over low latitudes, *Asian J. of Phys.*, *16,* 247, 2007.

148. Sekar, R., D. Chakrabarty, R. Narayanan, and A. K. Patra; Equatorial Spread F structures and associated airglow intensity variations observed over Gadanki, *Ann. Geophys.*, *26*, 3863–3873, 2008.

149. Sekar, R., S. Sarkhel, and D. Chakrabarty; A Review on the Na Airglow Mechanism using Simultaneous Na Airglow and Na Lidar Measurements over India, *Asian J. Phys.,* in press, 2010.

150. Slipher, V. M.; Emission in the spectrum of the light of the night sky, *Publ. Astron. Soc. Pac., 41,* 262–263, 1929.

151. Sipler, D. P., and M. A. Biondi; Interferometric studies of the twilight and nightglow sodium D-line profiles, *Planet. Space Sci., 26,* 65–73, 1978.

152. She, C. Y., S. Chen, Z. Hu, J. Sherman, J. D. Vance, V. Vasoli, M. A. White, J. Yu and D. A. Kreger; Eight-year climatology of nocturnal temperature and sodium density in the mesopause region (80-105 km) over Fort Collins, CO (41° N, 105° W), *Geophys. Res. Lett., 27,* 3289–3292, 2000.

153. Shi, X., D. R. Herschbach, D. R. Worsnop, and C. E. Kolb; Molecular beam chemistry; Magnetic deflection analysis of monoxide electronic states from alkali-metal atom plus ozone reactions, *J. Phys. Chem., 97*(10), 2113–2122, 1993.

154. Slanger, T. G., P. C. Cosby, D. L. Huestis, A. Saiz-Lopez, B. J. Murray, D. A. O'Sullivan, J. M. C. Plane, C. Allende Prieto, F. J. Martin-Torres, and P. Jenniskens; Variability of the mesospheric nightglow sodium D2/D1 ratio, *J. Geophys. Res.*, *110*, D23302, doi: 10.1029/2005JD006078, 2005.

155. Slanger, T. G., P. C. Cosby, D. L. Huestis, and B. D. Sharpee; Review of tropical nightglow studies with astronomical instruments, *J. Atmos. sol. Terr. Phys.*, *68*, 1426–1440, doi: 10.1016/j.jastp.2005.04.012, 2006.

156. Sreeja, V., Vineeth, C., Pant, Tarun Kumar, Ravindran, Sudha, and Sridharan, R.; Role of gravity wavelike seed perturbations on the triggering of ESF a case study from unique dayglow observations, *Ann. Geophys., 27,* 313–318, doi: 10.5194/angeo-27-313-2009, 2009.

157. Sridharan, R.; Study in the Composition of the Upper Atmosphere, *Ph. D. Thesis, Gujarat University, Ahmedabad, India,* 1983.

158. Sridharan et al.; Ionization hole campaigna coordinated rocket and ground-based study at the onset of equatorial spread-F: first results, *J. Atmos. Sol. Terr. Phys., 59,* 2051–2067, 1997.

159. Sridharan, S., S. Gurubaran, and R. Rajaram; Radar observations of the 3.5-day ultra-fast Kelvin wave in the low-latitude mesopause region, *J. Atmos. Sol. Terr. Phys., 64,* 1241-1250, 2002.

160. Sullivan, H. M.; Seasonal variation of the twilight sodium layer, *J. Atmos. Terr. Phys., 33,* 573-579, 1971.

161. Suzuki, S., Shiokawa, K., Hosokawa, K., Nakamura, K., and Hocking, W. K.; Statistical characteristics of polar cap mesospheric gravity waves observed by an all-sky airglow imager at Resolute Bay, Canada, *J. Geophys. Res., 114,* A01311, doi: 10.1029/2008JA013652, 2009a.

162. Suzuki, S., Shiokawa, K., Liu, A. Z., Otsuka, Y., Ogawa, T., and Nakamura, T.; Characteristics of equatorial gravity waves derived from mesospheric airglow imaging observations, *Ann. Geophys., 27,* 1625–1629, doi: 10.5194/angeo-27-1625-2009, 2009b.

163. Swenson, G. R., and S. B. Mende; OH emission and gravity waves (including a breaking wave) in all-sky imagery from Bear Lake, UT, *Geophys. Res. Lett., 21*(20), 2239–2242, 1994.

164. Swenson, G., Haque, R., Yang, W., and Gardner, C.; Momentum and energy fluxes of monochromatic gravity waves observed by an OH imager at Starfire Optical Range, New Mexico, *J. Geophys. Res., 104*(D6), 6067–6080, 1999.

165. Takahashi, H., Batista, P. P., Sahai, Y., Clemesha, B. R.; Atmospheric wave propagations in the mesopause region observed by the OH(8,3) band, NaD, O_2A(8645Å) band and OI 5577 Å nightglow emissions, *Planet. Space Sci., 33,* 381–384, 1985.

166. Takahashi, H., B. R. Clemesha, D. M. Simonich, S. M. L. Melo, N. R. Teixeira, A. Eras, J. Stegman, G. Witt; Rocket measurements of the equatorial airglow: MULTIFOT 92 database, *J. Atmos. Terr. Phys., 58,* 1943–1961, 1996a.

167. Takahashi, H., S. Melo, B. Clemesha, D. Simonich, J. Stegman, and G. Witt; Atomic hydrogen and ozone concentrations derived from simultaneous lidar and rocket airglow measurements in the equatorial region, *J. Geophys. Res., 101*(D2), 4033–4040, 1996b.

168. Takahashi, H., Taylor, M. J., Pautet, P.-D., Medeiros, A. F., Gobbi, D., Wrasse, C. M., Fechine, J., Abdu, M. A., Batista, I. S., Paula, E., Sobral, J. H. A., Arruda, D., Vadas, S. L., Sabbas, F. S., and Fritts, D. C.; Simultaneous observation of ionospheric plasma bubbles and mesospheric gravity waves during the SpreadFEx Campaign, *Ann. Geophys., 27,* 1477–1487, doi: 10.5194/angeo-27-1477-2009, 2009.

169. Taylor, M. J., Y. Y. Gu, X. Tao, C. S. Gardner, and M. B. Bishop; An investigation of intrinsic gravity wave signatures using coordinated lidar and nightglow image measurements, *Geophys. Res. Lett., 22*(20), 2853–2856, 1995a.

170. Taylor, M. J., M. Bishop, and V. Taylor; All-Sky Measurements of Short Period Waves Imaged in the OI(557.7 nm), Na(589.2 nm) and Near Infrared OH and O_2(0,1) Nightglow Emissions During the ALOHA-93 Campaign, *Geophys. Res. Lett.*, 22(20), 2833–2836, 1995b.

171. Taylor, M., W. Pendleton Jr., S. Clark, H. Takahashi, D. Gobbi, and R. Goldberg; Image measurements of short-period gravity waves at equatorial latitudes, *J. Geophys. Res., 102*(D22), 26283–26299, 1997.

172. Taylor, M. J., Pautet, P.-D., Medeiros, A. F., Buriti, R., Fechine, J., Fritts, D. C., Vadas, S. L., Takahashi, H., and So Sabbas, F. T.; Characteristics of mesospheric gravity waves near the magnetic equator, Brazil, during the SpreadFEx campaign, *Ann. Geophys., 27,* 461–472, doi: 10.5194/angeo-27-461-2009, 2009.

173. Torr, M. R., and D. G. Torr; The role of metastable species in the thermosphere, *Rev. Geophys., 20*(1), 91–144, 1982.

174. Thorne, A., U. Litzen, S. Johansson; Spectrophysics: Principles and Applications, *Springer-Verlag Berlin Heidelberg,* 1999.

175. Tsunoda, R. T.; Magnetic-field-aligned characteristics of plasma bubbles in the nighttime equatorial ionosphere, *J. Atmos. Terr. Phys., 42,* 743–752, 1980.

176. Vadas, Sharon L., Fritts, D. C., and Alexander M. J.; Mechanism for the Generation of Secondary Waves in Wave Breaking Regions, *J. Atmos. Sci., 60,* 194–214, 2003.

177. Venkateswara Rao N.; A Study on the Quasi-Periodic Radar Echoes from Low-Latitude E-Region, *Ph. D. Thesis, Sri Venkateswara University, Tirupati, India* 2008.

178. Venkat Ratnam, M., A. K. Patra, and B. V. Krishna Murthy; Tropical mesopause: Is it always close to 100 km?, *J. Geophys. Res., 115,* D06106, doi: 10.1029/2009JD012531, 2010.

179. Vineeth, C., T. K. Pant, M. Antonita, G. Ramkumar, C. V. Devasia, and R. Sridharan; A comparative study of daytime mesopause temperatures obtained using unique ground based optical and meteor wind radar techniques over the magnetic equator, *Geophys. Res. Lett., 32,* L19101, doi:10.1029/2005GL023728, 2005.

180. Vishnu Prashanth, P.; Broadband Resonance Lidar Studies of Mesospheric Sodium at a Tropical Station, *Ph. D. Thesis, Sri Venkateswara University, Tirupati, India* 2007.

181. Vishnu Prasanth, P., Sridharan, S., Bhavani Kumar, Y., and Narayana Rao, D.; Lidar observations of sporadic Na layers over Gadanki (13.5° N, 79.2° E), *Ann. Geophys., 25,* 1759-1766, doi: 10.5194/angeo-25-1759-2007, 2007.

182. Voelz, D.G.; Theoretical and Lidar studies of the seasonal and nocturnal variations of the mesospheric sodium layer at Urbana, Illinois, *Ph.D. thesis, University of Illinois, Urbana, Illinois,* 1987.

183. von Zahn, U., M. Gerding, J. Hoeffner, W.-J. McNeil, and E. Murad; Iron, calcium, and potassium atom densities in the trails of Leonids and other meteors: Strong evidence for differential ablation, *Meteorit. Planet. Sci., 34,* 1017–1027, 1999.

184. Walterscheid R. L., G. Schubert, and J. M. Straus; A Dynamical-Chemical Model of Wave-Driven Fluctuations in the OH Nightglow, *J. Geophys. Res.*, *92*, 1241–1254, 1987.

185. Walterscheid, R. L., and M. P. Hickey; Acoustic waves generated by gusty flow over hilly terrain, *J. Geophys. Res., 110,* A10307, doi: 10.1029/2005JA011166, 2005.

186. Williams, I. P.; In Meteors in the Earths Atmosphere; Murad, E., Williams, I. P., Eds., *Cambridge University Press: Cambridge,* 2002.

187. Won Y.-I., Kim, J., Niciejewski, R. J., Lee, B. Y., Chung, J. -K., Kim, Y. H.; Measurements of atmospheric waves in the upper mesosphere at Chungwon, Korea, *Adv. Space Res., 32,* 849–853, 2003.

188. Woodman, R. F. and La Hoz, C.; Radar observations of F region equatorial irregularities, *J. Geophys. Res., 81,* 5447–5466, 1976.

189. Wrasse, C. M., Nakamura, T., Takahashi, H., Medeiros, A. F., Taylor, M. J., Gobbi, D., Denardini, C. M., Fechine, J., Buriti, R. A., Salatun, A., Suratno, Achmad, E., and Admiranto, A. G.; Mesospheric gravity waves observed near equatorial and low–middle latitude stations: wave characteristics and reverse ray tracing results, *Ann. Geophys., 24,* 3229–3240, 2006a.

190. Wrasse, C. M., Nakamura, T., Tsuda, T., Takahashi, H., Medeiros, A. F., Taylor, M. J., Gobbi, D., Salatun, A., Suratno, Achmad, E., and Admiranto, A. G.; Reverse ray tracing of the mesospheric gravity waves observed at 23° S (Brazil) and 7° S (Indonesia) in airglow imagers, J. *Atmos. Sol. Terr. Phys., 68*(2), 163-181, 2006b.

191. Wright, T. G., A. M. Ellis, and J. M. Dyke; A study of the products of the gas-phase reaction M + N2O and M + O3, with ultraviolet photoelectron spectroscopy, *J. Chem. Phys., 98,* 2891–2907, 1993.

192. Xu, J., and A. K. Smith; Perturbations of the sodium layer: controlled by chemistry or dynamics?, *Geophys. Res. Lett.*, *30*(20), 2056, 10.1029/2003GL018040, 2003.

193. Yamada, Y., H. Fukunishi, T. Nakamura, and T. Tsuda; Breaking of small-scale gravity wave and transition to turbulence observed in OH airglow, *Geophys. Res. Lett., 28*(11), 2153–2156, 2001.

194. Zalesak, S., and S. Ossakow; Nonlinear Equatorial Spread F: Spatially Large Bubbles Resulting From Large Horizontal Scale Initial Perturbations, *J. Geophys. Res., 85(A5),* 2131–2142, 1980.